Investigations of an On-body Reflectometer Probe

Von der Fakultät für Ingenieurwissenschaften,

Abteilung Elektrotechnik und Informationstechnik

der Universität Duisburg-Essen

zur Erlangung des akademischen Grades

Doktor der Ingenieurwissenschaften

genehmigte Dissertation

von

Adam Buck

aus

Hindenburg

Gutachter: **Prof. Dr.-Ing. Klaus Solbach**

Gutachter: **Prof. Dr.-Ing. Andreas Czylwik**

Tag der mündlichen Prüfung: 18. Dezember 2015

Abstract

Radar can be utilized to detect the mechanical heart activity and is a potential alternative to today's heartbeat monitoring techniques in medicine. It can detect details of the heart activity, such as filling and ejection of heart chambers and opening and closing of heart valves. This is due to the radars ability to detect movements and direction of motion. Compared to electrocardiogram and ultrasound it has the advantage that it is a contactless measurement.

The objective of this thesis is the development of a proof-of-concept prototype of a novel microwave on-body sensor for heartbeat detection, which can be used inside an MRI system and which could provide prospective triggering information. The main idea is to use a microwave sensor (reflectometer) with an on-body antenna illuminating the heart and detecting the reflected signal.
The measurement is based on the evaluation of the heart-related time-dependent reflection coefficient of the antenna, by minimizing the static and respiration-related components of the reflection coefficient. In a first step, this is done by minimizing the antenna mismatch with an automatic impedance matching circuit after the placement of the antenna on the chest of an individual; the antenna mismatch is dependent on the position and the individual body properties. In a second step the residual static and slow variation signal from respiration is suppressed by a canceller circuit (well-known from CW radar technology as reflected power canceller).

With the reflectometer sensor system consisting of a CW signal generator (transmitter, Tx), on-body antenna, adaptive impedance matching circuit and demodulator circuit as part of the reflected signal canceller, the performance of each component influences the performance of the sensor system. Thus, the thesis concentrates on the design of the circuits and the antenna but also investigates the wave propagation scenario of the sensor applied to a human chest.

The signals measured with the microwave sensor are compared with a standard measurement method for heart activity, a heart sound measurement. This is used in order to assess the obtained signal and relate the signal states to certain heart states.

The measured radar signals are found to be sensitive to position of the sensor, the individual and the posture of the individual, making the interpretation of the signals challenging.

Acknowledgment

I want to express my deeply-felt thanks to my thesis advisor Prof. Dr.-Ing. Klaus Solbach for the continuous support, expertise, understanding and patience. His guidance helped me in all the time of research and writing of this thesis.

Besides my advisor, I would like to thank the rest of my committee members: Prof. Dr.-Ing. Andreas Czylwik, Prof. Dr. Roland Schmechel, Prof. Dr.-Ing. Rainer Kokozinski and Prof. Dr.-Ing. Holger Hirsch.

My sincere thanks goes to my colleagues at the Institute of Microwave and RF Technology, for the stimulating discussions, for all the fun we have had and for their support in tough times. I would also like to thank all other members of the department for their support and help.

I am deeply and forever indebted to my parents for their love and support throughout my entire life. I am also very grateful to my sister and her family who are a source of happiness.

Contents

List of Tables

List of Figures

1 Introduction

1.1 Motivation

Magnetic resonance imaging (MRI) systems are used among others in order to obtain images of the heart. A sequence of images is displayed as a movie showing the heart motion during the cardiac cycle (cardiovascular MRI). For image acquisition an electrocardiogram (ECG) signal can be used as a trigger to synchronize the MRI sequence with the cardiac cycle. The image acquisition can be guided in two different ways by the ECG. One technique is the prospective triggering where the preceding R-wave acts as a trigger for the information acquisition during the full cardiac cycle. The other technique, called retrospective gating, acquires MR data continuously and matched images and recorded ECG tracing.
In low-field strength MRI systems (1.5 Tesla and 3 Tesla) this triggering method works reliable. Due to the fact that the image quality is improved by higher field strengths, there is a trend towards ultra-high field MRI systems (e.g. 7 Tesla). Higher field strengths lead to artefacts in the ECG signal which result in a lack of synchronization. The artefacts can be caused by the static and dynamic magnetic fields, namely by the magnetohydrodynamic effect, gradient switching and RF pulses (for more details see appendix B.2 and B.3). Consequently, alternative methods are needed which work reliable inside (ultra-) high field MRI systems.

1.2 State of the Art

A large variety of sensors (capacitive, inductive, microwave, acceleration, optical and phono) and methods can be used to obtain an electrical signal which is related to the heart phase. Here, we put emphasis on those methods used in MRI systems. The best known method is the ECG gating, where the heart phase is determined by means of electrodes which are attached to the patient's chest. A multitude of techniques can be used in order to minimize interferences between the MRI system and ECG. In [1] several means are recommended including: ECG electrodes with minimal metal, electrodes and cables with no ferrous metals, special placement of electrodes and lines, twisting and banding of cables. Additionally, methods based on digital filtering of the ECG signal have been presented in [2] and [3].
Another approach is described in [4] where an acoustic sensor (microphone) and waveguide are used to record the acoustic heart tone. Due to the fact that this approach

does not interfere with the electromagnetic fields, it is suitable for ultra-high-field imaging. Additionally well-known methods like finger blood pressure sensors can be utilized.
Furthermore, a UWB pulse radar system is presented in [5] which is a non-contact approach. Decomposition of respiratory and cardiac motion is achieved by data analysis by applying blind-source separation based on several time-delay second order correlation matrices. The proposed method determines trigger events reliably and can also reject false trigger events caused by non-uniform respiration and partial breath holding. In contrast to ECG the UWB signal is related to the mechanical heart activity rather than to the electric activity.
Moreover remote Doppler radar systems are used in order to detect respiration and heartbeat (e.g. [6], [7] and [8]). The utilized Doppler radar systems are based on direct-conversion architectures with single or quadrature channel output signals. The approach relies on the evaluation of the signal reflected form the periodically moving chest. The moving air-body interface produces a Doppler modulated signal, which can be evaluated in order to obtain information about respiration and heartbeat. Due to the fact that respiration causes a greater displacement of the chest than the heart movement, the signal modulation related to heart activity is harder to detect.
Some of the mentioned methods detect the heartbeat information based on secondary phenomena like blood pressure or surface motion which occur with some time delay which could complicate the proper synchronization.

1.3 Goals of this Work

The goal of this work is the development of a proof-of-concept prototype of a novel microwave on-body sensor for heartbeat detection, which can be used inside an MRI system and which could provide prospective triggering information. The main idea is to use a microwave sensor (reflectometer) with an on-body antenna illuminating the heart and detecting the reflected signal. In the following, the sensor system is shortly explained and the related problem areas are indicated which require further investigation.
The measurement is based on the evaluation of the heart-related time-dependent reflection coefficient of the antenna, by minimizing the static and respiration-related components of the reflection coefficient. In a first step this is done by minimizing the antenna mismatch with an automatic impedance matching circuit after the placement of the antenna on the chest of an individual. The antenna mismatch is dependent on the position and the individual body properties. In a second step the residual static and slow variation signal (respiration) is suppressed by a canceller circuit (well-known from CW radar technology as reflected power canceller).
The total reflected signal at the antenna is a superposition of several reflections, resulting from antenna mismatch, skin reflection and reflections at inner body layers and organs. The first-mentioned reflections are static, whereas the signal reflected by the beating heart is time-dependent and can be separated. The skin reflection can be

high enough to saturate the receiver, thus masking the reflection of inner objects. To avoid the demodulator to be driven into saturation by the amplified received signal, a feedback canceller circuit is applied as a solution. Another dominant interfering signal results from respiration induced modulation of the antenna reflection coefficient. In comparison to Doppler radar systems this interference is caused by the change in volume and dielectric properties of the lung during respiration and not by displacement of the chest surface. By appropriate filtering of the total reflected signal by means of the feedback canceller, a signal related to the instantaneous heart phase can be obtained from the demodulator in real-time. With the reflectometer sensor system consisting of a CW signal generator (transmitter, Tx), on-body antenna, adaptive impedance matching circuit and demodulator circuit as part of the reflected signal canceller, the performance of each component influences the performance of the sensor system. Thus, the thesis concentrates on the design of the circuits and the antenna but also investigates the wave propagation scenario of the sensor applied to a human chest.
Finally, the signals measured with the microwave sensor are compared with a standard measurement method for heart activity like electrocardiography or heart sound measurement. This is necessary in order to assess the obtained signal and relate the signal states to certain heart states.

1.4 Structure of this Work

In chapter 2, initial measurements conducted with a vector network analyser and an antenna are presented which already show the functionality of a heartbeat sensor. The measured signals are analysed in time and frequency domain. The measurement method is explained and a model describing the underlying phenomena is given. An overview of the state of the art in sensing of vital signs using continuous wave Doppler radar is also given in chapter 2.
The reflectometer sensor system model is presented in chapter 3. It describes the structure of the reflectometer sensor and the formation of the time-dependent reflection coefficient.
In chapter 4, an investigation of electromagnetic wave propagation inside the human body is conducted in order to gain some insight in the underlying phenomena leading to the sensor signals. The investigation is done by means of an electromagnetic-field simulator, where a rectangular waveguide, excited by a broadband pulse, is placed at different positions on a human body torso model.
Chapter 5 is about the design of an on-body antenna matched to the human body.
The design of an adaptive impedance matching system, that is used in order to mitigate the residual antenna mismatch is described in chapter 6.
In chapter 7, the sensor receiver using the feedback canceller circuit is investigated. Finally in chapter 8, measurements conducted with the microwave sensor are presented and compared to heart sounds for several persons.
Appendix A and B give a brief introduction into the basics of magnetic resonance imaging and the problems with triggering cardiovascular imaging.

2 Initial Measurements and Concept of CW Doppler Radar

This chapter describes initial measurements of heartbeat related signals, conducted by means of a vector network analyzer and an on-body antenna, which can be termed reflectometer measurement. The measured signals are analysed in time and frequency domain and the frequency components are assigned to physical phenomena.
Due to the fact that, the reflectometer and continuous wave (CW) radar have many things in common, the basic concepts of CW Doppler radar and the sensing of vital signs by means of CW Doppler radar are presented. Some problems encountered in CW-radar systems and existing solutions are presented. In addition, an explanation for modulation of phase and magnitude of the received signal is given.

2.1 Initial Measurements with Vector Network Analyzer

Initial measurements were performed with a vector network analyzer (VNA) and an antenna (see Figure 2.1). The measurements of the reflection coefficient were conducted in time domain and continuous wave mode. The antenna was placed on the chest of an individual in upright position and a frequency around 850 MHz was chosen for minimum return loss of the antenna, such that the reflection resulting from mismatch was reduced. The incident wave $\underline{a}$ is constant and the reflected wave $\underline{b}$ is dependent on the antenna reflection coefficient $\underline{\Gamma}$. Evaluation of the magnitude and phase of the complex reflection coefficient of the antenna shows that those quantities contain modulation related to the heart activity (see Figure 2.2). The Figure shows the measured magnitude and phase of the reflection coefficient versus time for four different antenna positions on the chest. The periodic trend in either the magnitude or the phase of the reflection coefficient is clearly seen and corresponds to the heartbeat. Signal variations caused by respiration are observable as a slowly changing overlayed signal.
As can be seen, the cardiac information is induced on either the magnitude (Figure 2.2c) or the phase (Figure 2.2b) of the reflection coefficient or both (Figure 2.2a). The position of the antenna affects which quantity is stimulated. The variation of the phase is approximately 10° and the magnitude is altered by 0.6 - 1.5 dB around a low average level of about -20 dB. However the amount of variation depends on the chosen

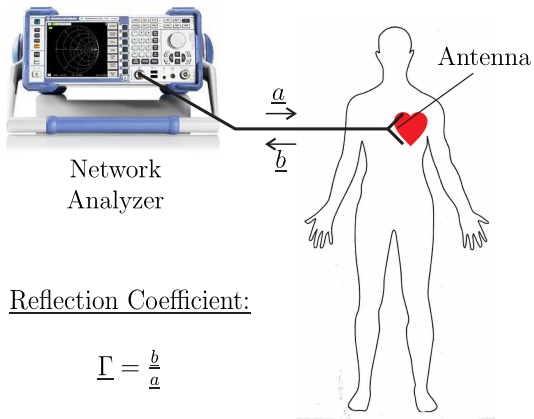

Figure 2.1: Measurements conducted with vector network analyzer

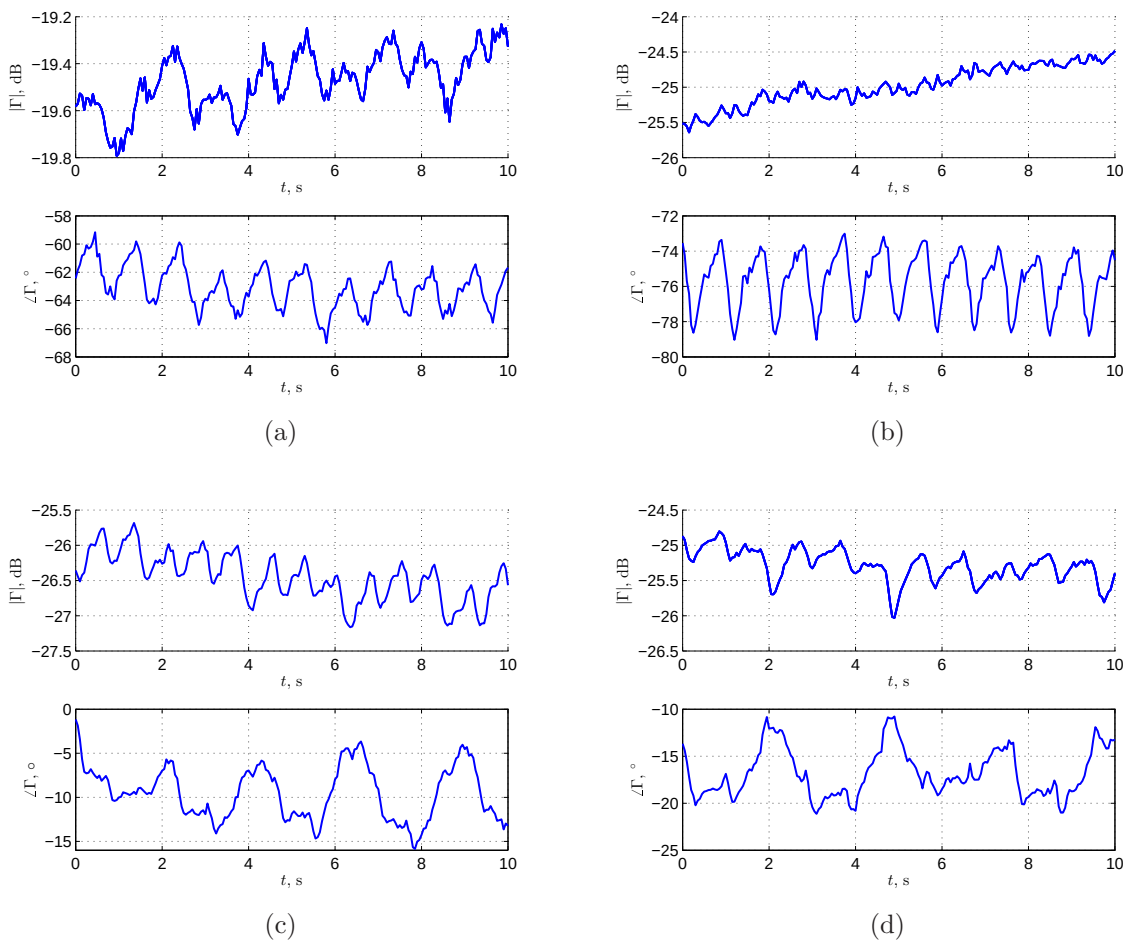

Figure 2.2: Variation of magnitude and phase of antenna reflection coefficient for four different positions on the chest.

position.
The constant component of the antenna impedance and consequently the reflection coefficient, is affected by the chosen position, due to the fact that the chest occupies the antenna near field and is not a homogeneous structure.
In order to analyse the frequency spectrum of the magnitude and phase of the reflection coefficient, the mean value is subtracted to obtain only the signal variation. Figure 2.3a and 2.3b show the variation of the measured quantities in time domain and their corresponding normalized spectra. Both spectra differ from each other and contain

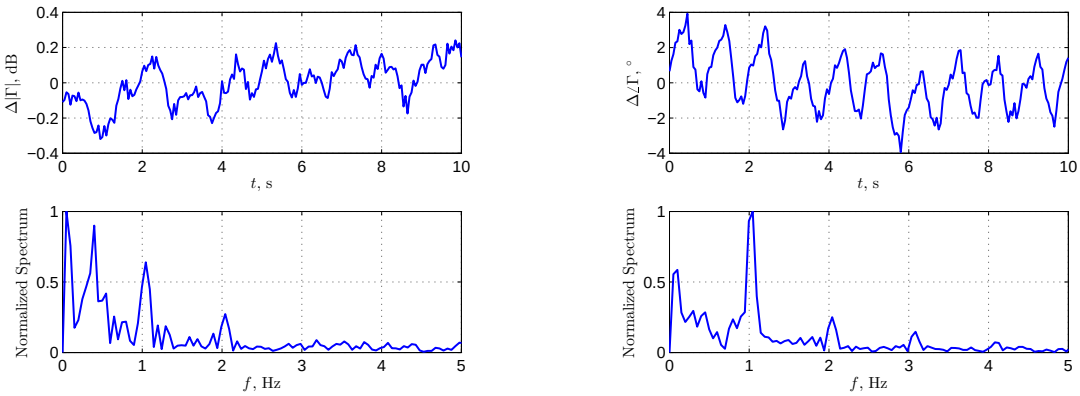

(a) (b)

Figure 2.3: Signal variation for antenna position of Figure 2.2a. Magnitude variation and normalized spectrum (a). Phase variation and normalized spectrum (b).

several frequency components. Components below 1 Hz belong to the respiration and around 1 Hz to the heartbeat. Due to the fact that the cardiac activity produces pulse-like signals, up to three frequency components (harmonics) corresponding to the heartbeat can be found. For antenna position of Figure 2.2 (a) the magnitude variation is dominated by the respiration and the phase variation by the heartbeat. These results need to be explained:
One reasonable assumption could be that the change of the ventricular volume and the measured heart signal are correlated. Due to the contraction and expansion of the

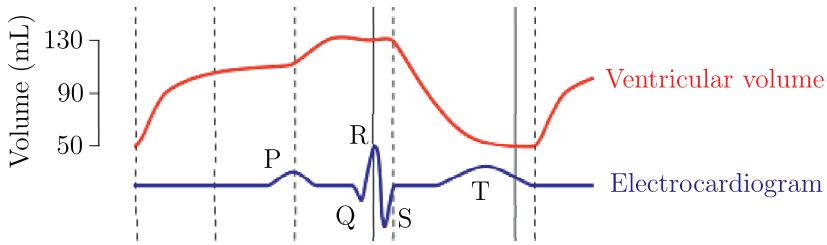

Figure 2.4: Ventricular volume and electrocardiogram

heart the spatial position and the size of reflecting body (the heart) changes, so that

the reflection of the incident wave depends on the instantaneous phase of the heart. As a result, both the magnitude and the phase of the reflected wave may be modulated. Figure 2.4 shows the ventricular volume and the electrocardiogram for one cardiac cycle. The waveform of the ventricular volume change resembles the measured heart signal (compare Figure 2.3b). Thus it can be concluded that the measured signal is related to the mechanical activity of the heart.

The described method for heartbeat measurement could be characterized as an on-body reflectometer and is based on the placement of an antenna on the body in the middle of the chest, where the reflected microwave signal is measured. A good penetration of the electromagnetic energy into the body is important because reflected signals from inside the body are used for determination of the heartbeat. Hence it is necessary to obtain a reasonable antenna matching which depends on the position of the antenna and the individual body structure. Apart from impedance mismatch of the antenna and the feed cable, the total reflection is composed of two parts, one static part which originates from the reflection at the antenna-skin interface, and a second dynamic part which is caused by respiration and heartbeat. One aim is to decrease the influence of the human body and the positioning of the antenna on the operation of the heartbeat sensor and as a consequence to decrease the static reflection. In order to use the measured signal as a trigger, a threshold would be used to detect a certain heart phase. In this scenario a superimposed respiration signal hampers a correct detection.
Figure 2.5 shows a simplified model of the measurement setup and the formation of the time-variant reflection coefficient as a superposition of several reflections. This

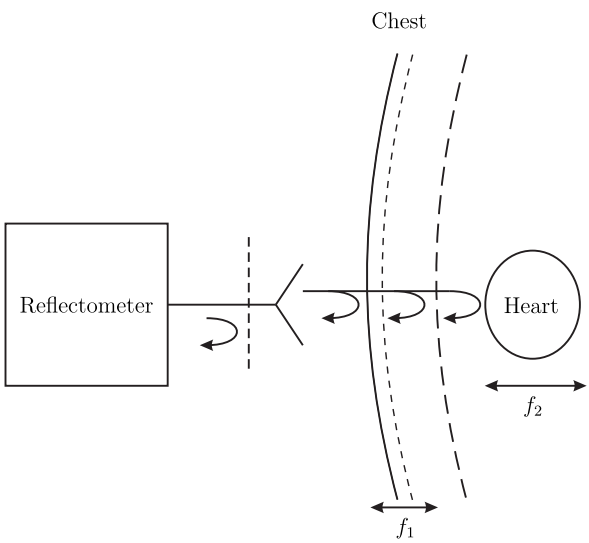

Figure 2.5: Formation of time-dependent reflection coefficient

model assumes wave propagation and is extremely simplified due to the fact that the on-body antenna near-field extends into the body where some modulation of the reflection coefficient may result from change in volume and dielectric properties of the inner organs during respiration and mechanical activity of the heart. Independent of

the underlying phenomena, the resulting modulation of the reflection coefficient can be evaluated to show heartbeat activity.

The measurement is based on the evaluation of the time-dependent reflection coefficient of the antenna $\underline{\Gamma}(t)$, which is a function of the time-dependent reflected wave $\underline{b}(t)$ (assuming constant incident wave $\underline{a}$) and can be termed vector reflectometer measurement.
This kind of measurement is closely related to the principle of CW-Doppler Radar systems. Both systems emit electromagnetic waves and detect waves reflected by objects. The received signal is mixed with the Tx-signal (down-conversion) and the baseband signal is evaluated.
However there are some differences. In the case of CW-Doppler radar, the sensor is separated form the object by a distance. The emitted wave propagates in free space and is reflected at the air-skin interface. For a moving object the frequency of the reflected wave is shifted due to the Doppler effect. In order to gain information about velocity and direction of movement of the object, the Doppler shift is evaluated. Furthermore, the reflection caused by antenna mismatch and the object are separated. Whereas in the case of the reflectometer, sensor and object are not separated by a distance and there is no wave propagation in free space. Baseband signal evaluation is based on the time-dependent magnitude and phase of the reflected signal.
On these grounds we discuss the function of the reflectometer and analyse the received signal from the point of view of radar theory.

2.2 Sensing of Vital Signs using CW Doppler Radar

2.2.1 Signal Model

2.2.1.1 Single-Target Model

The CW radar transmits the following signal:

$$T(t) = \cos(2\pi f t + \phi_{\mathrm{n}}(t)), \tag{2.2.1}$$

where f is the transmitter frequency, t is the elapsed time and $\phi_{\mathrm{n}}(t)$ the phase noise of the local oscillator. The signal $T(t)$ is reflected by a single target at distance d_0 with a time-varying displacement given by $x(t)$. The received signal $R(t)$ can by approximated as [9]:

$$R(t) \approx \cos\left[2\pi f t - \frac{4\pi d_0}{\lambda} - \frac{4\pi x(t)}{\lambda} + \phi_{\mathrm{n}}(t - \frac{2d_0}{c})\right], \tag{2.2.2}$$

where it is assumed that $x(t) << d_0$, λ is the wavelength and c propagation velocity of light. Due to the assumption that $x(t) << d_0$, the amplitude variation is negligible

and does not contain information about the displacement of the target. Therefore normalized amplitudes are used in the following section. $R(t)$ is similar to the transmitted signal with a time delay caused be the nominal distance d_0 and the phase modulated by the motion $x(t)$ of the target. Using the same oscillator for the LO and transmitter signal, keeps the phase noise of the two signals correlated as long as the distance to the target is kept small. Mixing the received signal $R(t)$ with the LO signal (homodyne receiver or direct conversion receiver) and filtering the output, the baseband signal $B(t)$ is obtained:

$$B(t) = \cos\left[\theta + \frac{4\pi x(t)}{\lambda} + \Delta\phi(t)\right], \tag{2.2.3}$$

where

$$\Delta\phi(t) = \phi_{\mathrm{n}}(t) - \phi_{\mathrm{n}}\left(t - \frac{2d_0}{c}\right) \tag{2.2.4}$$

is the residual phase noise and

$$\theta = \frac{4\pi d_0}{\lambda} + \theta_0, \tag{2.2.5}$$

is the constant phase shift which depends on the nominal distance to the target d_0 and the quantity θ_0 which depends on the phase shift at the reflection surface and distance between mixer and antenna [9]. Phase noise is critical when a high-phase noise oscillator is used and can be negligible at short range due to the range-correlation effect, which is descried in detail in [9] and [10]. Depending on the relation between the displacement $x(t)$ and the wavelength λ, two approximations can be considered.

1. $x(t) \approx \lambda$:
   For this case $B(t)$ is the same as given in equation 2.2.3. Defining $\Theta = \theta + \frac{4\pi x(t)}{\lambda} + \Delta\phi(t)$ it becomes obvious that the signal $B(\Theta)$ is non-linearly dependent on the phase Θ (see Figure 2.6, left). The constant phase shift θ determines the shape of $B(t)$, such that for the same $x(t)$ the output signal is different in shape for different θ (see Figure 2.6, right) [11]. It can be seen that the amplitude of $B(t)$ becomes smaller when θ is an integer multiple of π, such that the sensitivity is decreased.

2. $x(t) << \lambda$:
   In the case that the displacement $x(t)$ is much smaller than the wavelength λ, the small angle approximation is valid and the signal $B(t)$ becomes (phase noise is neglected):

$$B(t) = \cos(\theta) \cdot \left[1 - \left(\frac{4\pi x(t)}{\sqrt{2}\lambda}\right)^2\right] - \sin(\theta) \cdot \frac{4\pi x(t)}{\lambda}. \tag{2.2.6}$$

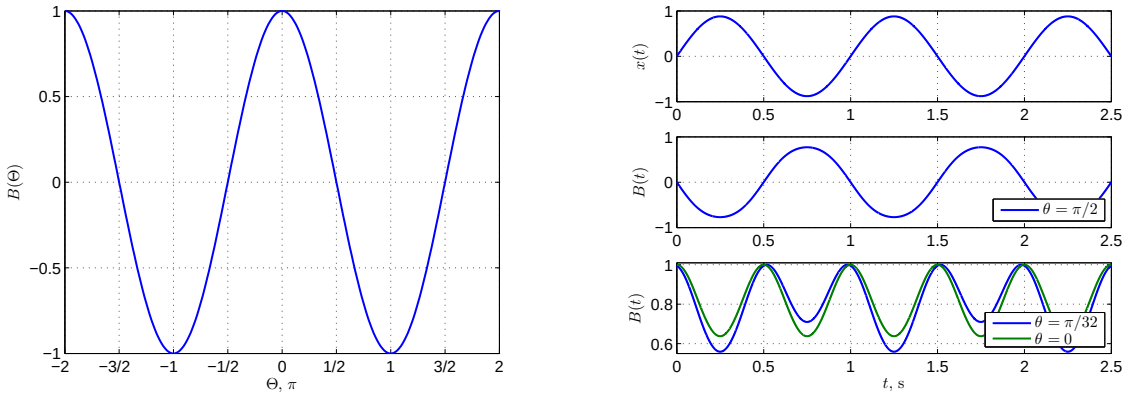

Figure 2.6: Phase dependence of baseband signal

If the phase θ is an odd multiple of $\pi/2$, the baseband signal is approximately:

$$B(t) \approx \frac{4\pi x(t)}{\lambda}. \tag{2.2.7}$$

In this particular case, the baseband signal is proportional to the displacement $x(t)$ and the phase-demodulation sensitivity is maximum (optimum point). Another particular case appears when the phase θ is an integer multiple of π, the approximated output signal becomes:

$$B(t) \approx 1 - \left[\frac{4\pi x(t)}{\sqrt{2}\lambda}\right]^2. \tag{2.2.8}$$

Again $B(t)$ is no linear function of the displacement $x(t)$ and the sensitivity is decreased. These points are known as null points and occur when the LO signal and the received signal $R(t)$ are either in-phase or 180° out of phase [9].

In order to avoid null detection points a quadrature receiver can be used, where the two output channels are [9]:

$$B_{\mathrm{I}}(t) = \cos\left[\theta + \pi/4 + \frac{4\pi x(t)}{\lambda} + \Delta\phi(t)\right], \tag{2.2.9}$$

and

$$B_{\mathrm{Q}}(t) = \cos\left[\theta - \pi/4 + \frac{4\pi x(t)}{\lambda} + \Delta\phi(t)\right]. \tag{2.2.10}$$

If one of the channels is in the null detection point then the other will be in the optimum phase-demodulation point. The worst case occurs when θ is an integer multiple of π,

then neither receiver chain is at the optimum phase-demodulation point and the signals become ($x(t) << \lambda$) [9]:

$$B_{\mathrm{I}}(t) = B_{\mathrm{Q}}(t) \approx \frac{1}{\sqrt{2}} - \frac{1}{\sqrt{2}} \cdot \left[\frac{4\pi x(t)}{\lambda} + \Delta\phi(t) \right]. \tag{2.2.11}$$

For this case the heart signal can still be detected.
In [12], further topologies are presented to overcome the null detection, three are based on phase diversity and one on frequency diversity. Two topologies based on phase diversity and two-channel receivers ensure that when one channel receives a minimum, then the other receiver receives a maximum. The combination of both output signals ensures the detection of the heart signal (the same is true for the quadrature receiver). The other two topologies, one based on a variable phase shifter, the second on frequency diversity (voltage controlled oscillator) have the advantage of using a single-channel receiver, but must be controlled by software.

2.2.1.2 Target-in-Clutter Model

A single reflector model of the heartbeat is presented in [6] for a radar system that is situated at a distance to the patient's chest. It is described that the physiological motion appears as phase and amplitude modulation in the radar signal. Additionally to the chest movement, the radar records all other objects within the antenna beam (clutter) by a superimposed signal without modulation.
It is assumed that the heartbeat and respiration cause a periodic movement of the chest surface and therefore the chest is modelled as a reflector with an initial distance d_0 from the radar superimposed by a sinusoidal small range variation $x_{\mathrm{h}}(t)$. As a result, the time dependent distance $x_{\mathrm{m}}(t)$ between the antenna and the target can be written as:

$$x_{\mathrm{m}}(t) = x_{\mathrm{h}}(t) + d_0. \tag{2.2.12}$$

Furthermore the assumption is made, that the electromagnetic wave does not penetrate into the body and consequently reflections at inner interfaces are not taken into account.
Based on the physiological motion model a characterization of the modulation of the radar signal is derived. The amplitude of a spherical wave propagating in air undergoes attenuation inversely proportional to the distance from the source (inverse square law). Due to this, the change in amplitude resulting from the change in range is negligible. Thus it is concluded that the modulation in a single channel receiver manifests as phase

modulation in the carrier and is converted to an amplitude modulation. For a quadrature receiver, a complex base-band signal $\underline{b}(t)$ with phase modulation corresponding to the moving chest, can be given as:

$$\underline{b}(t) = A_{\mathrm{s}}e^{j\phi_{\mathrm{s}}} + A_{\mathrm{m}}e^{j\phi_{\mathrm{m}}(t)} + n(t), \tag{2.2.13}$$

$$A_{\mathrm{s}}e^{j\phi_s} = \sum_n A_{\mathrm{n}}e^{j\frac{2\omega_c x_{\mathrm{n}}}{c}}, \tag{2.2.14}$$

$$\phi_{\mathrm{m}}(t) = \frac{2\omega_{\mathrm{c}}x_{\mathrm{m}}(t)}{c} = \phi_{\mathrm{h}}(t) + \phi_0. \tag{2.2.15}$$

Where $A_{\mathrm{s}}e^{j\phi_{\mathrm{s}}}$ represents the stationary reflectors within the antenna beam (clutter), $A_{\mathrm{m}}e^{j\phi_{\mathrm{m}}(t)}$ represents the reflection from the moving chest and $n(t)$ represents the receiver noise. $\phi_{\mathrm{h}}(t)$ is a time varying phase proportional to $x_{\mathrm{h}}(t)$ and ϕ_0 is a fixed phase resulting from the fixed distance d_0. Equation 2.2.13 is rewritten to:

$$\underline{b}(t) = A_{\mathrm{s}}e^{j\phi_{\mathrm{s}}} + A_{\mathrm{m}}e^{j\phi_{\mathrm{h}}(t)}e^{j\phi_0} + n(t), \tag{2.2.16}$$

and illustrated in Figure 2.7. As can be seen, the total signal is the superposition of

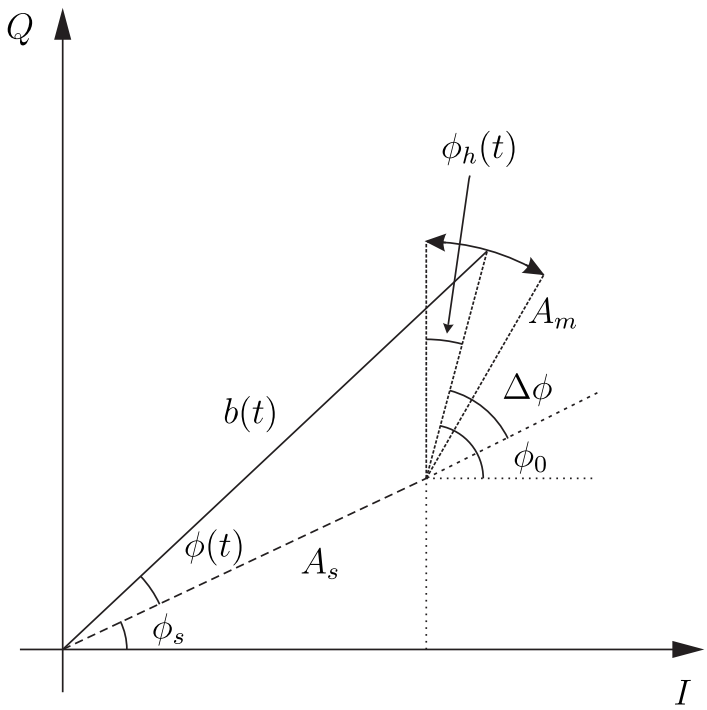

Figure 2.7: Signal in the complex plane with stationary and moving scatterers [6]

the stationary and time-varying signal. Furthermore the total signal is modulated in phase and amplitude albeit the moving target only creates a phase modulation in the

model. For further investigation of these modulations, Equation 2.2.16 is rewritten to:

$$\Delta\phi = \phi_0 - \phi_\mathrm{s}, \tag{2.2.17}$$
$$\underline{b}(t) = e^{j\phi_\mathrm{s}}\left[A_\mathrm{s} + A_\mathrm{m}e^{j\Delta\phi}e^{j\phi_\mathrm{h}(t)}\right] + n(t), \tag{2.2.18}$$
$$= e^{j\phi_\mathrm{s}}A(t)e^{j\phi(t)} + n(t), \tag{2.2.19}$$

with:

$$A(t) = \sqrt{A_\mathrm{m}^2 + A_\mathrm{s}^2 + 2A_\mathrm{s}A_\mathrm{m}\cos\left(\Delta\phi + \phi_\mathrm{h}(t)\right)}, \tag{2.2.20}$$
$$\phi(t) = \tan^{-1}\left(\frac{A_\mathrm{s}\sin(\phi_\mathrm{s}) + A_\mathrm{m}\sin\left(\phi_0 + \phi_\mathrm{h}(t)\right)}{A_\mathrm{s}\cos(\phi_\mathrm{s}) + A_\mathrm{m}\cos(\phi_0 + \phi_\mathrm{h}(t))}\right) - \phi_\mathrm{s}. \tag{2.2.21}$$

Additionally the real and imaginary part of the complex base-band signal $\underline{b}(t)$ is obtained:

$$\mathrm{Re}\{\underline{b}(t)\} = A_\mathrm{s}\cos(\phi_\mathrm{s}) + A_\mathrm{m}\cos\left(\Delta\phi + \phi_\mathrm{h}(t)\right) + \mathrm{Re}\{n(t)\}, \tag{2.2.22}$$
$$\mathrm{Im}\{\underline{b}(t)\} = A_\mathrm{s}\sin(\phi_\mathrm{s}) + A_\mathrm{m}\sin\left(\Delta\phi + \phi_\mathrm{h}(t)\right) + \mathrm{Im}\{n(t)\}. \tag{2.2.23}$$

It is concluded that based on this model it can be explained whether the modulation appears in the amplitude or phase, or in the real or imaginary part of the baseband signal, by considering the relative position and size of the stationary reflectors and the moving reflector. From equation 2.2.20 it can be seen that $A(t)$ is no linear function of the displacement $\phi_\mathrm{h}(t)$ and that by reducing the stationary reflection ($A_\mathrm{s} \to 0$) the total amplitude $A(t)$ becomes equal to the amplitude A_m and the amplitude is no longer modulated. For this case a signal is obtained that is solely phase modulated. In the case that:

$$\Delta\phi = n \cdot \pi \quad \text{with } n = 0, \pm1, \pm2, ... \tag{2.2.24}$$

the stationary and moving reflector vectors point either into the same or opposite direction. This results in a signal with nearly no amplitude but phase modulation, thus these points can be termed amplitude modulation null points. Another special case is that:

$$\Delta\phi = (2n-1) \cdot \frac{\pi}{2} \quad \text{with } n = \pm1, \pm2, ... \tag{2.2.25}$$

For this case the stationary and the moving reflector vectors are orthogonal. Consequently the total signal is modulated stronger in amplitude than in phase, thus these points can be termed phase modulation null points.
Equation 2.2.21 shows that the reflections from stationary objects cause a DC offset, which hampers correct detection of $\phi(t)$, as will be shown later.

2.2.2 Advanced CW Doppler Radar Concepts

Approaches for elimination of the null/optimum detection point problem found in literature are presented in the following two sub-chapters. The first approach eliminates the null/optimum detection point problem in single channel Doppler radar receiver systems, the second in quadrature Doppler radar receiver systems.

2.2.2.1 Elimination of null/optimum Detection Point Problem in Single Channel Doppler Radar Receiver Systems

A single channel receiver architecture is proposed in [13]. Based on a phase tuning method the optimum demodulation point is achieved and DC offset is removed simultaneously. By virtue of self-mixing, LO leakage and clutter reflections, one of the problems of homodyne receivers is the large DC offset of the down-conversion mixer. It is stated that a large DC value can saturate the baseband amplifier and also restricts the ADC input range to a higher value, consequently limiting the ADC resolution. Known solutions for this issue are either AC coupling of the mixer outputs or baseband DC cancellation techniques before amplification. As disadvantages of AC coupling, time delay and distortion of the physiological signals are mentioned. Further it is pointed out that DC cancellation techniques require a real time control unit. This unit subtracts the estimated DC voltage from the mixer output prior to sending the signal to a baseband amplifier. In contrast, the proposed architecture effectively performs analog linear signal demodulation and provides a single DC coupled output with no distortion.
Figure 2.8 illustrates the single channel receiver architecture, which transmits a signal TX and receives signals reflected from a subject and clutter. A phase shifted (Φ_1) and attenuated (A) version of the LO signal is fed back and added to the RX signal. Subsequently the resulting signal is phased shifted (Φ_2) and down-converted. The baseband

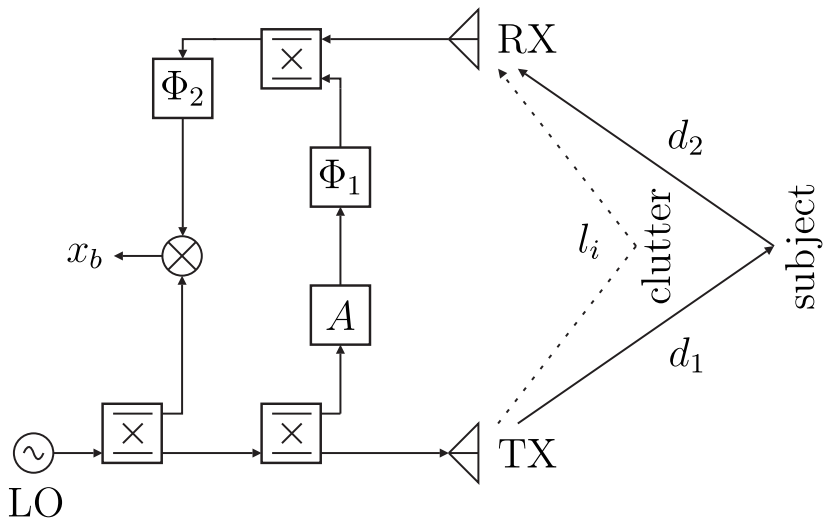

Figure 2.8: Single channel receiver architecture

signal results in (for a detailed derivation see [13]):

$$\begin{aligned} x_{\mathrm{b}}(t) &= \frac{a}{2}\cos\left(-\omega\frac{d_1+d_2}{c}+\psi(t)+\Phi_2\right) \\ &\quad +\frac{1}{2}\sum_i b_i\cos\left(-\omega\frac{l_i}{c}+\Phi_2\right)+\frac{A}{2}\cos(\Phi_1+\Phi_2), \end{aligned} \tag{2.2.26}$$

where a is the received signal amplitude, ω is the angular transmit frequency, ψ is the phase change caused by physiological motion, d_1 and d_2 are the distances between TX antenna and subject and RX antenna and subject, respectively. The term b_{i} represents the clutter signal amplitude and l_{i} is the distance a signal travels from transmitter to receiver with reflection at each clutter object.
Equation 2.2.26 consists of an AC component which is related to the physiological motion of the subject (first term) and a DC component (second and third term). The DC component can be minimized by a proper combination of Φ_1 and Φ_2, additionally the optimum demodulation point can be achieved by a proper choice of Φ_2, such that the output signal can be approximated as $\psi(t)$.
An experimental setup was used to verify the theory, where Φ_1 and Φ_2 were varied independently between 0° and 180°. It turned out that the phase Φ_1 has to be tuned first in order to remove the DC offset and to tune Φ_2 afterwards in order to maximize the AC signal amplitude. Otherwise the necessary amplifier gain for meaningful AC signal amplitudes results in saturation. The minimization of the DC offset required more than one tuning iteration and was achieved simultaneously with an optimization of AC signal amplitude.

2.2.2.2 Elimination of null/optimum Detection Point Problem in Quadrature Doppler Radar Receiver Systems

Arctangent Demodulation In [14], arctangent demodulation is presented to overcome position sensitivity issues in quadrature receivers. The I and Q signals detected by a quadrature Doppler radar can be expressed as follows:

$$B_{\mathrm{I}}(t) = \cos\left[\theta+\frac{4\pi x(t)}{\lambda}\right], \tag{2.2.27}$$

$$B_{\mathrm{Q}}(t) = \sin\left[\theta+\frac{4\pi x(t)}{\lambda}\right]. \tag{2.2.28}$$

By combining the two signals, accurate phase demodulation can be achieved whatever the target position is [14]:

$$\phi(t) = \arctan\left[\frac{B_{\mathrm{Q}}(t)}{B_{\mathrm{I}}(t)}\right] = \arctan\left[\frac{\sin\left(\theta+\frac{4\pi x(t)}{\lambda}\right)}{\cos\left(\theta+\frac{4\pi x(t)}{\lambda}\right)}\right] = \theta+\frac{4\pi x(t)}{\lambda}. \tag{2.2.29}$$

Receiver imperfection (circulator isolation, antenna mismatch and mixer isolation) and clutter reflection result in DC offset, which is a challenge in this technique. These DC components can be large in comparison to the AC signal resulting from motion, such that digitization of the signal cannot be performed without adversely affecting resolution. Therefore, a DC offset compensation method is required in order to capture the motion related signal with maximum resolution and for the proper functioning of the arctangent demodulation. Taking the DC offset into account, equation 2.2.29 can be rewritten as:

$$\phi(t) = \arctan\left[\frac{B_{\mathrm{Q}}(t)}{B_{\mathrm{I}}(t)}\right] = \arctan\left[\frac{V_{\mathrm{Q}} + \sin\left(\theta + \frac{4\pi x(t)}{\lambda}\right)}{V_{\mathrm{I}} + \cos\left(\theta + \frac{4\pi x(t)}{\lambda}\right)}\right]. \tag{2.2.30}$$

where V_{Q} and V_{I} are the DC offset of each signal. Another contribution to the DC offset is caused by the position of the target, see equation 2.2.27 and 2.2.28. This DC component contains information about the position and can be valuable for certain applications.

Complex Signal Demodulation In [15], a complex signal demodulation technique is presented to overcome the null detection point problem in non-contact vital sign detection. It is stated that the proposed method is easier to implement than the arctangent demodulation and is robust against DC offset. DC-offset can be removed by calculating the average signal for a time domain sliding signal window and subtraction from the initial signal. The complex signal is software-reconstructed by [15]:

$$S(t) = B_{\mathrm{I}}(t) + j \cdot B_{\mathrm{Q}}(t) = A \exp\left[j\left(\theta + \frac{4\pi x(t)}{\lambda} + \Delta\phi(t)\right)\right], \tag{2.2.31}$$

where the exponential term has always an amplitude of one and thus eliminates the effect of θ on signal amplitude. The further analysis is based on the Fourier transform and is conducted in the frequency domain.

2.2.2.3 Leakage and Flicker Noise in Direct Conversion Receivers

A homodyne or direct conversion receiver (DCR) translates the RF signal to baseband in a single frequency conversion. Beside some advantages, the direct conversion receiver major drawbacks are leakage and flicker ($1/f$) noise. LO-leakage is a consequence of finite isolation between the LO and RF port of a mixer which results in self-mixing and consequently in a DC-offset. Flicker noise can be a great issue if the down-converted signal is located closed to zero frequency. It is known that flicker noise is higher for active mixers because of DC-bias current flow through the switching transistors. Even in passive mixers where no DC-bias is required, a DC-offset due to self-mixing of the LO-signal is present. In any case, the DC-offset results in an increase in flicker noise.

Additionally passive mixers require a quite high LO power (7 dBm or higher) which leaks to the RF-port due to finite isolation. In [16] the DC-offset was reduced by using a LO-leakage cancellation method achieving improved noise figure.

2.2.2.4 Digitally Controlled DC Offset Compensation

In [17], a system with digitally controlled voltage feedback and real-time center find function is proposed that compensates DC offset and preserves important DC information for extraction of cardiopulmonary activity related phase. The adaptive DC offset compensation system is based on a feedback path which includes a 16-bit ADC, a DSP and a 16-bit DAC. A center find function is implemented on the DSP for DC information preservation. This system is able to overcome issues inherent in CW direct conversion Doppler radar, including a large DC offset in relation to the signal of interest. It was demonstrated in experimental results, that the proposed technique provides significant improvements of accuracy in heart rate extraction.
A fast clutter cancellation method for quadrature Doppler radar, which is used for non-contact vital sign detection is proposed in [18]. The DC offset caused by clutter is eliminated by means of a clutter cancellation generator employed in the radar receiver. The generator produces a signal based on the detected DC offset values in the quadrature channels, which is anti-phase to the received clutter signal, such that a superposition of the clutter signal and the generator signal leads to cancellation of the clutter signal and consequently to an elimination of the DC offset. The cancellation generator consists of a voltage-controlled variable phase shifter and voltage-controlled variable attenuator and is controlled by a baseband processor.

2.2.2.5 Digital Signal Processing Technique

A rate finding algorithm based on extended Kalman filter is presented in [19] for quadrature direct-conversion Doppler radar. The Kalman filter is an optimal estimator that estimates the state of a discrete time-controlled process by using a feedback control. The algorithm is based on two groups of equations, time update equations and measurement update equations. To put it simply, the time update equations function as predictor equations and the measurement update equations function as corrector equations. The extended Kalman filter is a nonlinear version of the conventional Kalman filter, which is used for systems having nonlinear dynamic models. For a review of the extended Kalman filter and a derivation of the system model, the interested reader is referred to [19].
In a first step of the signal processing, the I/Q signals are low-pass filtered in order to avoid aliasing effects and out of band noise. Then, the signals are A/D converted and fed into the extended Kalman filter module for state estimation. A principle component analysis for channel selection is performed in order to avoid null-point demodulation.
Experimental results obtained with the proposed system were compared with ECG

measurements for heart rate detection. It is stated that the results demonstrate the feasibility and accuracy of the algorithm to estimate the heart rate from I/Q signals.

2.2.3 Doppler Radar for Detection of Mechanical Heart Activity

This section focuses on the concept and the state of the art of Doppler radar as a diagnostic and monitoring tool for heartbeat measurements.

2.2.3.1 Overview

The radar monitors the mechanical movements of the heart and therefore offers additional details of the heart phases, compared to the ECG which only provides information about the electrical activity of the heart. Details provided by radar are the opening and closing of the heart valves and the filling and rejection of the heart chambers [7]. A further advantage compared with ECG is that radar does not require a number of electrodes attached to the human chest. The radar approach is comparable to echocardiography where ultrasound is used to monitor the mechanical activity of the heart. Due to the differences of sound wave and electromagnetic wave propagation, the two approaches may detect different phenomena. Again the advantage of radar over ultrasound is that radar can be used through clothing and that no gel is necessary between the probe and the skin.
Electromagnetic wave propagation inside the human body undergoes attenuation because tissues are lossy media. In [20], based on simulation the attenuation of the air-heart-air path was evaluated in the $0.1-3\,\mathrm{GHz}$ range for a layered thorax model exposed to an incident plane wave. The attenuation increases with frequency ($25-58\,\mathrm{dB}$) and is higher in the case of deflated lung compared to inflated lung. As a reason for that the higher conductivity of the deflated lung and a lower reflection coefficient at the heart-lung interface is stated. In [21] it was computed for non-contact radar, that approximately 70 % of the incident energy is reflected at the air to skin interface. Due to this it is concluded that the observed heartbeat modulations originate from small movements of the body surface.
In an early investigation [8] of a continuous-wave microwave system a coaxial applicator was located over the apex of the heart at a height of about 3 cm above the chest wall. It is found that the reflected signal is modulated in amplitude and in phase by the movement of the chest wall and that the amplitude and phase changes depend significantly on the applicator position. It was concluded that, in order to minimize the body surface reflections the antenna should be located on the body so that the heart movements can be measured directly.

2.2.3.2 On-Body Radar

In [7] an on-body radar was used to detect changes in the human heartbeat. As a radar a vector network analyzer connected to a pair of bow-tie antennas was used. The antennas were strapped on the chest with 8 cm spacing. It is not clear what the purpose of using two antennas is, the author presumes that the measurement is based on a bi-static radar approach. Continuous wave measurements ($f = 1$ GHz) in conjunction with ECG and blood pressure measurements were conducted before and after physical activity. The measurements were performed while the person was holding his breath. Changes observed in the radar measurement were in compliance with changes in the ECG and blood pressure measurements, showing that radar can reliably detect changes in the heartbeat. It was pointed out that while the heartbeats appear mainly as phase modulation, there is also some in the amplitude. Further, the phase modulation contains an offset due to static scatterers and system DC. Assuming that the heartbeats are mainly noticed as phase variations, the heartbeat information can be obtained by using phase estimation and DC offset cancellation techniques [7]. These methods were used to get the time varying phase which is directly related to heart movements. Additionally it is stated that the instantaneous frequency can contain information related to the heart movement hardly seen in the phase variation. The instantaneous frequency is defined as the derivative of the phase with respect to time:

$$\omega(t) = \frac{\mathrm{d}\phi(t)}{\mathrm{d}t}. \tag{2.2.32}$$

While the phase changes are related to the displacement of an object the instantaneous frequency is related to the velocities of the object movements. Consequently large movements are visible in the phase variation whereas fast but small movements may be hard to see in the phase but lead to large variations of the instantaneous frequency.

A detailed analysis of the CW radar heartbeat waveforms is given in [7]. In this analysis radar measurements were conducted simultaneously to ECG measurements and examined by means of the Wigger's diagram. The Wigger's diagram depicts the ventricular, atrial and aortic pressure, the ventricular volume and the heart sounds together with the ECG. It was figured out that the phase of the radar recording follows the ventricular volume, whereas the heart sounds connected to the opening and closing of the heart valves are correlated with peaks in the instantaneous frequency waveform. For a more detailed analysis of the waveform events the interested reader is referred to [7].

Furthermore it is pointed out that during the heartbeat, the heart rotates and stretches and that the opening and closing of the heart valves cause shock waves that spread over the heart surface and into surrounding tissues. In addition, the blood density is changed during the heartbeat, leading to small changes in the dielectric properties of the tissues. This may modulate the backscattered wave if the flow of blood goes through the radar wave path. Consequently the radar measurement is affected by all

the mentioned effects.
It has been shown in [11] that Doppler radar can be used to characterize the mechanical activity of the heart and provides information comparable to impedance cardiography. Impedance cardiography uses special electrodes in order to inject current into the thorax and measures a voltage between sensing electrodes. This requires direct body contact and is a disadvantage compared with the Doppler radar sensor. The two-channel Doppler radar is based on a commercially available microwave motion sensor KMY24, operating at 2.45 GHz. Based on an approximation for the near field, as given in [22] (operating frequency $f = 2.45\,\mathrm{GHz}$, antenna width $D = 3.5\,\mathrm{cm}$ and muscle tissue $\varepsilon_\mathrm{r} = 53$) and from SAR measurements it is concluded that all measurements took place in the near field of the utilized antenna. However the near field characteristic of the module's antenna is unknown, because not all details about the antenna design are known. In-vivo measurements were conducted on more than one position on the thorax with the Doppler radar sensor. The measurements show that the radar signal depends substantially on the position on the thorax and that multiple measurements at the same position yield repeatable results. Therefore it is crucial to find the best position before conducting the measurement.
The investigation was continued in [23] where it is proposed to extract points of no movement in a heart cycle to characterize the heart motion phases. This is based on the capability of Doppler radar sensors to measure speed, direction of movement and the change in direction. The discriminative criterion for the case that the object movement is zero, is extracted from the time derivatives of the two quadrature receiver output signals. A local extreme of both signals indicates that the velocity of the movement is zero and therefore both derivatives are jointly zero. It is pointed out that the advantage of this analysis is a well-defined criterion, which is insensitive to signal offset and other often unknown system parameters, that enables the detection of resting states during the object movement. Simultaneous measurements were conducted with the Doppler radar sensor positioned at the sternum and a standard 1 lead ECG. It is found that the derivatives of the obtained signals exhibit several simultaneous zero-crossings. These common zero-crossings can be utilized to separate the different phases of the heart's pumping function (for a detailed analysis see [23]).
These results are confirmed in [24] where a handheld device for simultaneous measurement of electrical (ECG) and mechanical (CW-Doppler radar) cardio-vascular activities is presented. The measurements were conducted for several positions on the left thorax without breathing. A signal with the heart beat period was observed for all positions, however, the signal shape differs significantly for different sensor positions. It is concluded that the position dependent shape results from the detection of different movements of the underlying structures (aorta, right heart, left heart) at different penetration depths. This inevitably entails a challenge for the interpretation of the obtained signal. Further it is deduced that the broad radar radiation beam of the utilized system is the reason for the comparable signal information content. The method described in [11] was used to extract characteristic timing points with a clear distinction of the systole and diastole. In addition, the influence of posture of a subject on signal shape was investigated. The signal shape differs significantly when the subject is in supine or standing position. In conclusion, due to the mentioned

position and posture dependent signal shapes the use of the pulse shape properties for the detection of characteristic timing points is hampered. However this issue can be conquered partially for certain sensor positions by using the detection of simultaneous zero-crossings in both radar channels.

3 Reflectometer Sensor System

This chapter describes the reflectometer sensor system model and the basic structure of the reflectometer sensor.

3.1 System Model

The system model is depicted in Figure 3.1. It shows the reflectometer sensor consisting of the reflectometer circuit, the adaptive impedance matching network and the on-body antenna. The adaptive impedance matching network is supposed to reduce the antenna mismatch and therefore increase the signal radiated into the body. A realizable adaptive impedance matching network is not capable to eliminate the mismatch completely and the reduction of mismatch depends on the load impedance. In order to suppress the residual constant part of the reflection a reflectometer circuit is used. The formation of the time-dependent reflection coefficient, which is assumed to be a superposition of several reflections, is also a part of the system model.

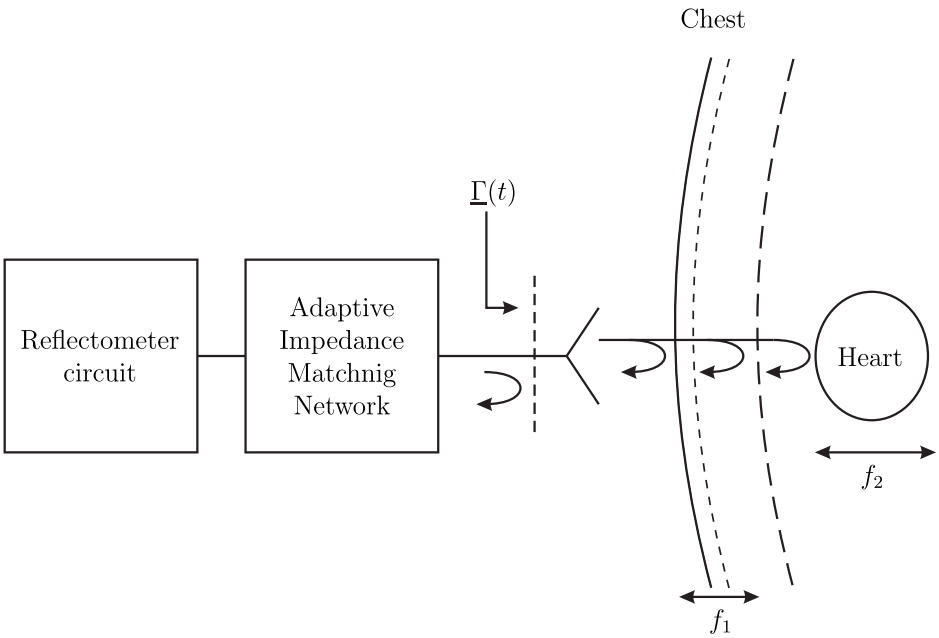

Figure 3.1: System model

3.2 Basic Structure of Reflectometer Sensor

The reflectometer sensor with a detailed representation of the reflectometer circuit with reflected power canceller is illustrated in Figure 3.2. It is based on a quadrature

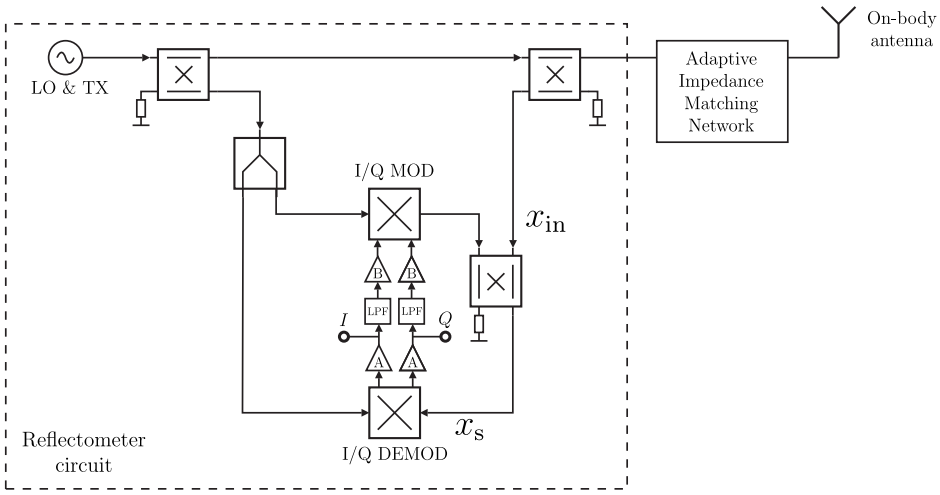

Figure 3.2: Reflectometer sensor

direct-conversion receiver in order to eliminate the null/optimum detection point problem by applying arctangent or complex signal demodulation. The LO and TX signal is generated by an RF source and distributed by a network consisting of couplers and power dividers.

The principle of operation of the canceller circuit is the superposition of the received signal by a signal with same amplitude but opposite phase, generated by the canceller circuit. In order to do this the received signal is mixed with the transmit signal (down-conversion) in the I/Q demodulator and the resulting low-frequency signal is low-pass filtered with a cut-off frequency below the heartbeat frequency. The obtained filtered signal contains a DC component resulting from the static part of the reflection coefficient and a time-variant component resulting from respiration. This signal is up-converted and used for the cancellation of the unwanted static and respiration signal, while the heartbeat signal component is not suppressed and remains available as in-phase and quadrature signal at the output of the receiver.

Due to the operating principle of the feedback canceller circuit it is assumed that the DC-offset resulting from self-mixing is reduced and as a consequence also the flicker noise.

4 Investigation of EM-Wave Propagation

4.1 What is the purpose of this chapter?

The purpose of this chapter is to get an idea of the phenomena that take place when an electromagnetic wave propagates inside the chest region. The investigation uses a rectangular waveguide at different positions to excite a wave into the chest and the reflected signal is evaluated. In order to investigate a wide frequency range the waveguide is excited by a wideband pulse. In this way the effect of position on the reflected signal can be investigated.

In [25] electromagnetic waves scattered by a human heart model at different polar and azimuthal incidence angles are investigated. The heart model consists of a myocardium, right and left atria with ventricles and is surrounded by free space. It is shown that scattering depends on a variety of parameters as the orientation of the heart as well as polarization and mode of the electromagnetic wave. In the present investigation the complete torso is taken into account, such that effects resulting from different properties of the chest are included.

In this work, it is assumed that the occurrence of phase and/or amplitude modulation of a continuous wave reflected signal is caused by a superposition of dynamic and static effects. Static effects originate from, e.g., fixed phase reflections due to fixed position and orientation on a chest and polarization, while dynamic effects are caused by time varying processes and are described by, e.g., Doppler effect. Depending on the interaction of these two effects either amplitude or phase or both are affected. Here only the static effects of the reflected wave are investigated.

4.2 Properties of Human Body Tissues

As the RF signal from the sensor antenna has to travel through the human body to be reflected at the heart and returned back to the antenna, it is important to consider the properties of the intermediate medium, the body tissues. The dielectric properties of human body tissues are described by the relative permittivity ε_r and electric conductivity σ. Both quantities are functions of frequency and can be calculated for a frequency range 10 Hz - 100 GHz using a parametric model and parameter values

derived by C. Gabriel and colleagues [26]. Table 4.1 lists the dielectric properties of some tissues relevant for this work for $f = 868$ MHz.

Tissue name	σ, [S/m]	ε_r	$\tan\delta$	λ, [m]	Penetration depth, [m]
skin dry	0.85617	41.576	0.42646	0.052435	0.040842
skin wet	0.83301	46.212	0.3733	0.049972	0.044047
heart	1.2129	60.107	0.41708	0.043644	0.034638
lung deflated	0.84586	51.538	0.33989	0.047449	0.045685
lung inflated	0.45125	22.063	0.42357	0.072	0.056434
muscle	0.93213	55.109	0.35028	0.045848	0.042904

Table 4.1: Human body tissue properties, based on [26]

As can be seen, during respiration the dielectric properties of the lung change significantly. Deflated lungs have an $\varepsilon_r = 51.5$ and $\sigma = 0.846$ S/m while inflated lungs have an $\varepsilon_r = 22.06$ and $\sigma = 0.452$ S/m. For the different phases of the heart no data was found such that the changes of the dielectric properties cannot be assessed. But it is self-evident that the dielectric properties change during the cardiac cycle due to the fact that the heart is filled with blood during diastole and blood is pumped into the arteries during systole and blood has different ε_r and σ than the heart muscle. Also the volume changes of organs in the near field of the antenna affect the reflection coefficient, and consequently the reflected signal. For many organs a change in volume is associated with changes of the dielectric properties. In the case of an antenna applied to the chest, the respiration leads to changes in the reflection coefficient of the antenna due to the fact that the lung occupies a portion of the antenna near field.

4.3 EM-Simulation

The investigation is conducted by means of the electromagnetic field simulator EMPIRE XCcel^{TM} utilizing a human body model (Figure 4.1). The human body model is defined by a volume with a equidistant mesh called voxel. Where electrical (Gabriel model) and thermal parameters are assigned to each voxel. A rectangular waveguide filled with a dielectric ($f_c = 695$ MHz) is exited with a broadband pulse and the response is evaluated. This approach is not consistent with the reflectometer measurement where a continuous wave signal is used. Furthermore the human body model is a static model which does not imitate the periodic motion of a heart and further time dependent changes. Thus the results can only provide an indication of what is actually causing the effects in a real measurement.

Simulations are done for several arbitrarily chosen waveguide positions on the chest. The excitation pulse and its frequency spectrum are shown in Figure 4.2. The pulse covers a frequency range from about 0.8 to 9.2 GHz and is centered at 5 GHz.

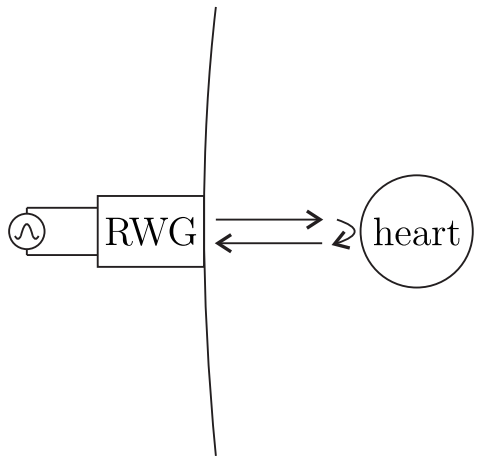

Figure 4.1: Rectangular waveguide placed on human chest

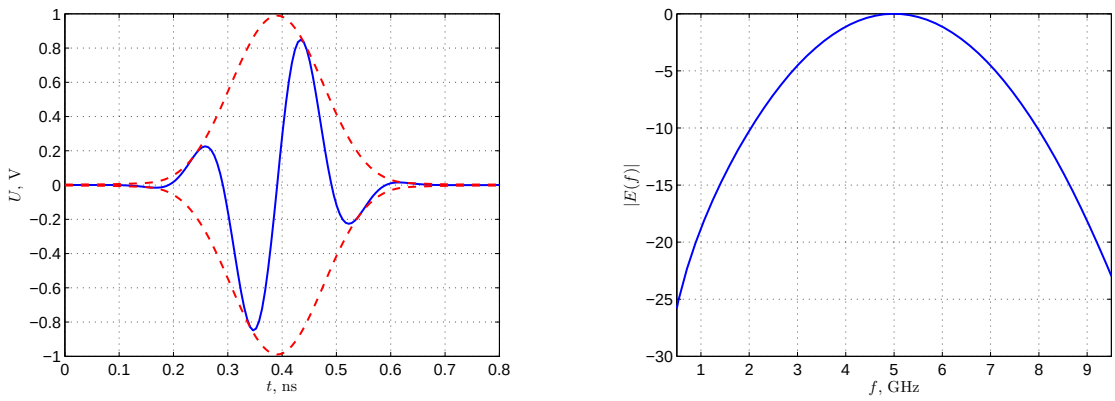

Figure 4.2: Excitation pulse and normalized spectrum

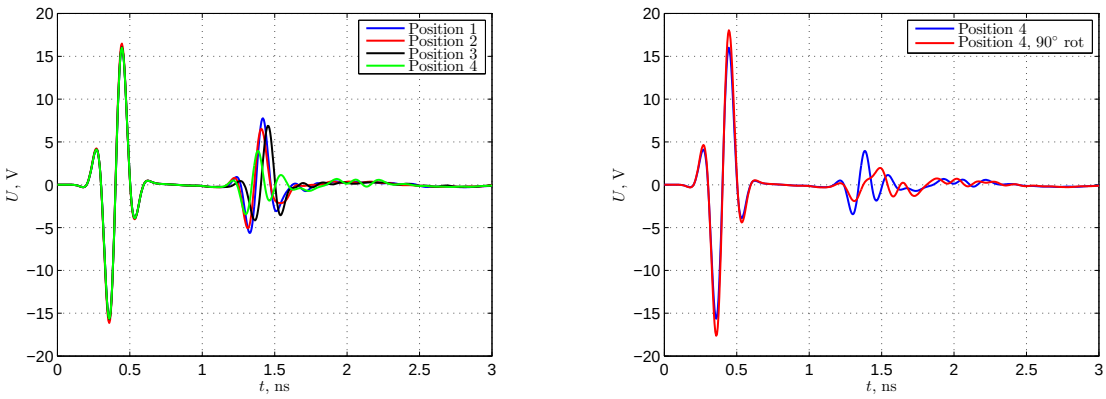

(a) (b)

Figure 4.3: Pulse responses for different positions (a) and different waveguide orientation (b)

In a first step the pulse responses shown in Figure 4.3a and 4.3b are evaluated and compared. Figure 4.3a illustrates responses of four different positions, Figure 4.3b shows a comparison of responses for the same position but different orientations of the waveguide.

The first pulse is the excitation pulse shaped by the waveguide followed by the skin reflection. The skin reflection is different for each position but occurs almost at the same point in time. Additionally the reflection depends on the orientation of the waveguide. These variations in skin reflections result from the fact that the chest is not a uniform surface. Thus the waveguide aperture does not lie flat on the chest which leads to gaps between sections of the aperture and the chest, so that the reflection is altered. Additionally the properties of the underlying layers differ for different positions on the chest. Reflections caused by inner layers occur after the skin reflection. Due to the pulse duration there is a superposition of several reflections and it is hard to distinguish between the single reflections. In order to figure out the heart response alone a second simulation is needed. By changing the electromagnetic material properties of the heart the respective reflected signal is also changed. From the comparison (Figure 4.4) of two simulations for the same position with different heart properties it is possible to figure out the time delay where the heart response occurs. In this scenario the heart material parameters are changed from the standard values to those of a perfect electric conductor (PEC). For the latter case the heart response increases because the magnitude of reflection coefficient increases to 1.

Based on the method described in [27], the impulse response of the heart can be determined. Figure 4.5 shows a channel model of the conducted simulations. The excitation pulse spectrum $E(f)$ is shaped by the waveguide, then enters the body where it is reflected and attenuated by several layers. Subsequently it is reflected by the heart and travels back to the waveguide.

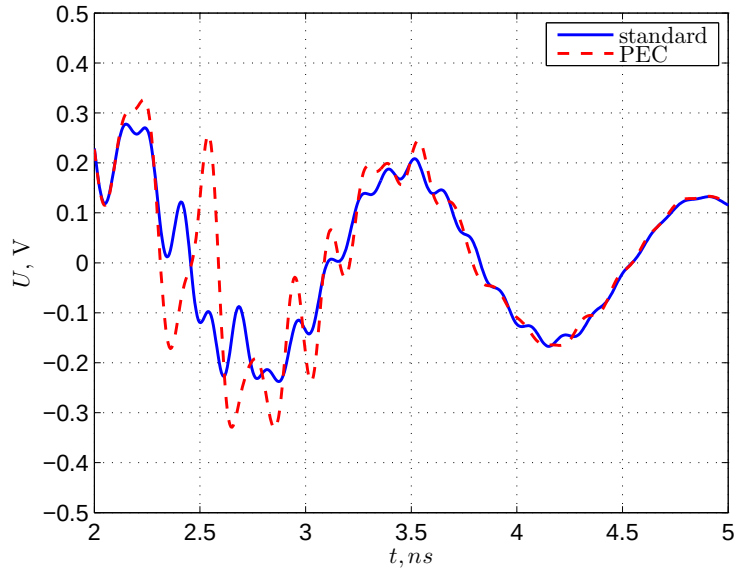

Figure 4.4: Pulse response for different heart properties

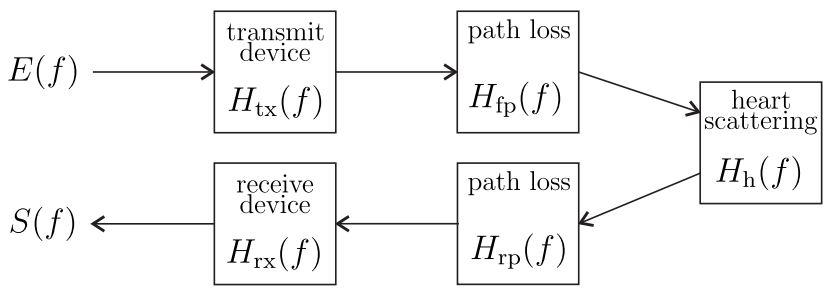

Figure 4.5: Channel model of the simulation setup

The contributions of the waveguide and the path loss in the body can be found, by means of a second simulation where the heart is replaced with a perfectly conducting plane, such that the wave is reflected totally for all frequencies. Thus for those two described simulations the following relationships are obtained:

$$S_{\mathrm{t}}(f) = E(f) \cdot H_{\mathrm{tx}}(f) \cdot H_{\mathrm{fp}}(f) \cdot H_{\mathrm{h}}(f) \cdot H_{\mathrm{rp}}(f) \cdot H_{\mathrm{rx}}(f), \tag{4.3.1}$$

$$S_{\mathrm{r}}(f) = E(f) \cdot H_{\mathrm{tx}}(f) \cdot H_{\mathrm{fp}}(f) \cdot (-1) \cdot H_{\mathrm{rp}}(f) \cdot H_{\mathrm{rx}}(f), \tag{4.3.2}$$

where $S_{\mathrm{t}}(f)$ is the response for the standard case and $S_{\mathrm{r}}(f)$ for the case that the heart is replaced with a perfectly conducting plane. The transfer function of the heart can be found by dividing $S_{\mathrm{t}}(f)$ by $S_{\mathrm{r}}(f)$ and multiplying by -1 :

$$H_{\mathrm{h}}(f) = -\frac{S_{\mathrm{t}}(f)}{S_{\mathrm{r}}(f)}. \tag{4.3.3}$$

$S_{\mathrm{t}}(f)$ and $S_{\mathrm{r}}(f)$ are band-limited signals with out-of-band components which become imprecise due to numerical inaccuracies of the electromagnetic field simulation. Thus the computation of the ratio $S_{\mathrm{t}}(f)/S_{\mathrm{r}}(f)$ introduces inaccuracies for lower and higher frequency components as shown in Figure 4.6 (left). For instance a negative spike can be seen at 12.5 GHz and a positive at 0 Hz. Furthermore the shown function $H_{\mathrm{h}}(f)$ is constant for frequencies above 12.5 GHz, despite the input signal contains almost no energy in this frequency range. These inaccuracies lead amongst others to an oscillating impulse response (see Figure 4.6, right) and to a negative impulse at $t = 0\,\mathrm{s}$ which results from the nearly constant frequency spectrum. Frequency windowing can be used in order to suppress these inaccuracies [27]. The window is chosen such that frequency components which are not contained by the input signal are attenuated. However, since the negative impulse ($t = 0\,\mathrm{s}$) in the impulse response cannot be suppressed by the windowing, the results for $t < 1\,\mathrm{s}$ are neglected. In the following, a Gaussian function is used as the windowing function. The application of a window function is indicated by a superscripted W.

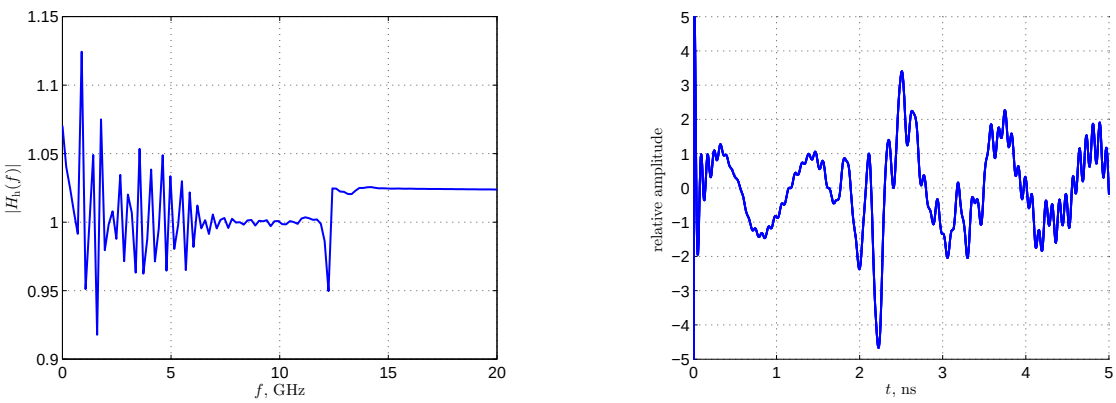

Figure 4.6: Inaccuracies due to band-limited signals

The EM-simulation provides results in the time domain, therefore some additional processing is required (Figure 4.7). First the time-domain responses are transformed into the frequency domain and then the ratio is multiplied by -1. Afterwards the resulting transfer function $H_\mathrm{h}(f)$ is multiplied by a Gauss function $W(f)$ and transformed back to time domain to obtain the impulse response of the heart $h_\mathrm{h}^W(t)$.

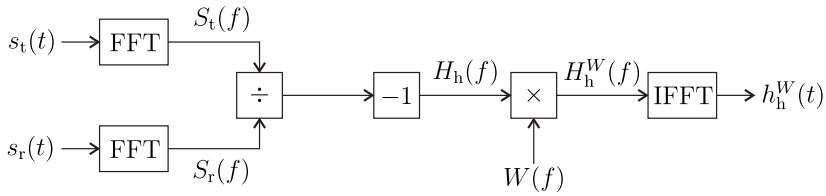

Figure 4.7: Signal processing chain

Figure 4.8 shows resulting signals for three different wavegiude positions on the chest. The curves indicate up to two reflections following the first reflection. With a decrease in peak amplitude for the second and third reflection. Furthermore the first reflection occurs at different points in time with different peak amplitudes and shapes.

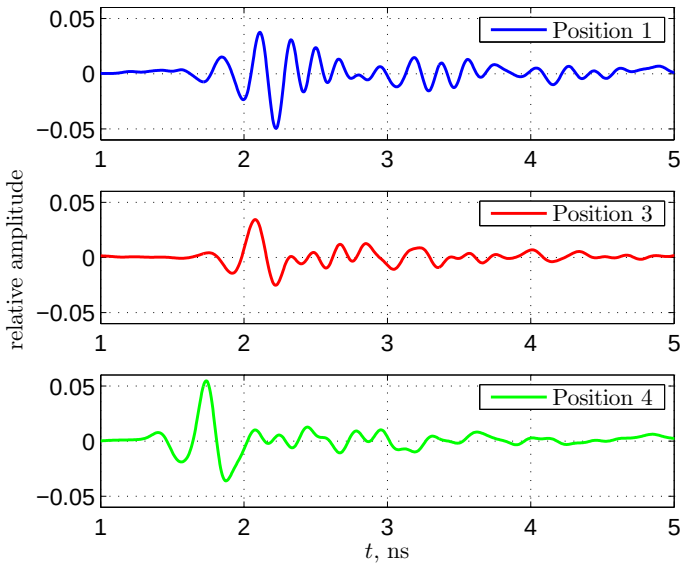

Figure 4.8: Impulse response $h_\mathrm{h}^W(t)$ for different waveguide positions

The time shift of the corresponding reflection results from a variable distance between waveguide aperture and heart dependent on the chosen position. Likewise the peak value is effected by distance, nature of reflecting surface and properties of the layers the wave penetrates in order to reach the heart. Furthermore it is assumed that the second and third reflection results from multiple back-and-forth reflections inside the body. It should be kept in mind that these responses are only valid for the static case. Figure 4.9 exemplary depicts the normalized spectrogram (short-term Fourier transform) of the pulse response for position 1 and 3. It can be seen clearly that the received

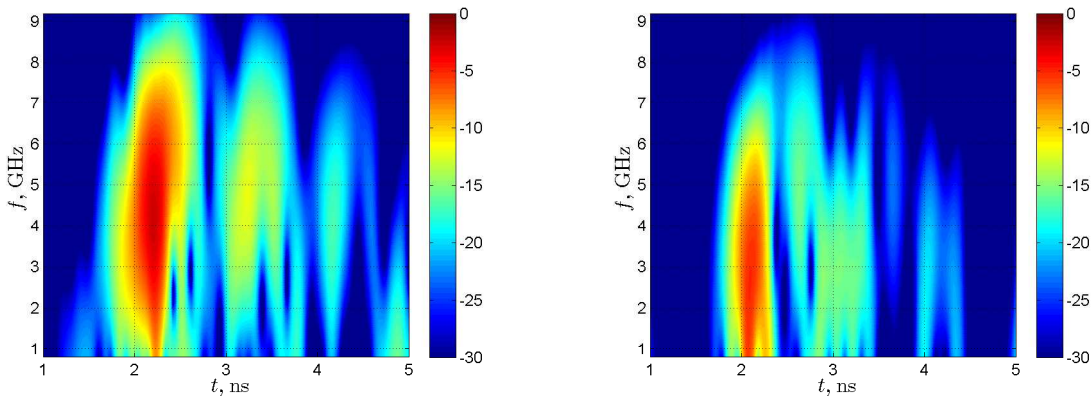

(a) (b)

Figure 4.9: Spectrogram of Impulse response $h_{\mathrm{h}}^{W}(t)$ for (a) position 1 (b) position 3

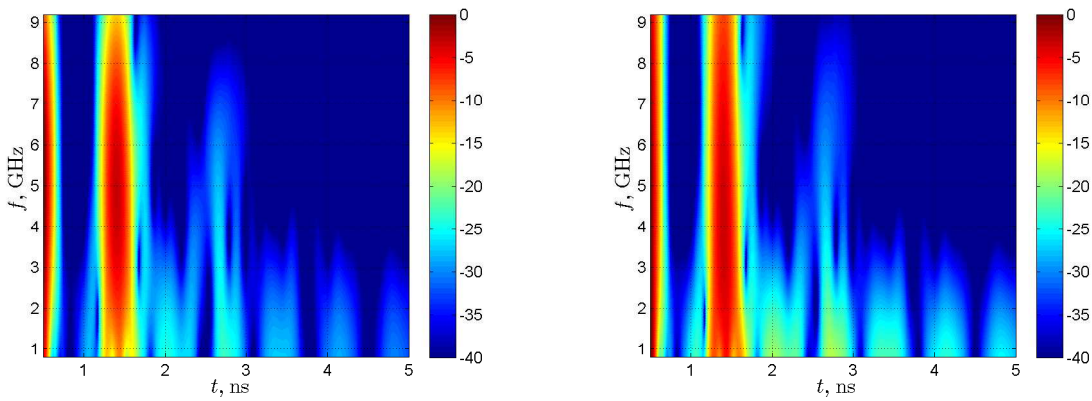

(a) (b)

Figure 4.10: Spectrogram of (a) signal received by waveguide and (b) signal attenuation

signals contain different frequencies. For position 1 the dominant frequency components are around 4.5 GHz, whereas for position 3 the dominant frequency components are around 3 GHz. The second and third pulse follow the first with a delay of 1 ns and 2 ns, respectively. The distance between the waveguide aperture and heart is almost equal for both positions, but body layers between skin and heart differ for both positions.

In Figure 4.10 (a) the spectogram of the signal received by the waveguide is depicted, for the case that the heart is replaced with a perfectly conducting plane. The excitation pulse, skin reflection and the reflection caused by the perfectly conducting plane are visible. In order to assess the frequency dependent attenuation, the shown spectogram is normalized to the spectrum of the excitation pulse and the attenuation is plotted in Figure 4.10 (b). By examining the attenuation of the first reflected pulse ($t \approx 2.6$ ns) it can be seen that, higher frequencies undergo a higher attenuation (approx. 30 dB

at 6 GHz) than lower frequencies (approx. 20 dB at 1 GHz).

In the dynamic case, the reflected signal is a function of time due to the contraction and relaxation of the heart. It is hard to predict how this deformation of the heart affects the reflected signal. From measurement it is known that the amplitude and/or phase of a CW signal is modulated. The amplitude and phase modulation can be explained by the contraction and relaxation of the heart which goes along with deformation of the heart.

4.4 Conclusion

It has been shown that both the skin reflection and heart reflection are dependent on the applicator position on the chest. Although the waveguide is filled with a dielectric in order to minimize the skin reflections, considerable differences between the skin reflections are observed. Some simulated heart impulse responses show that beside the main reflection up to two subsequent reflections can occur.

5 On-Body Antenna

The goal is to design a compact lightweight antenna with low sensitivity to variations in anatomic properties and maximum strength of reflected field from the heart. In contrast to the design of applicators for hyperthermia, where the aim is local heating of tissues and achievement of certain SAR distributions, the reflectometer antenna acts as a transmit and receive antenna. In this application SAR considerations do not play any role because of low power usage. Due to high attenuation of the RF signals inside the human body the received signals are weak and therefore the sensor should be sensitive only to signals coming from the direction of the illuminated object. Consequently this means that backward and side radiation should be minimized. This chapter describes the effect of the human body on microstrip patch antenna characteristics, like impedance match, energy coupling and field distribution.

5.1 Basic Considerations

5.1.1 Antennas Surrounded by Conducting Media

In [28] it is pointed out that the standard antenna analysis techniques fail for antennas in conducting media. The concepts of radiation resistance and antenna gain break down when the antenna is in a conducting medium. It is also shown that the choice of the origin of the coordinate system highly affects the radiation pattern. The reason for this is that most of the energy is dissipated in the immediate vicinity of the antenna, caused by the fields which, for antennas in free space, are related to stored energy. Furthermore it is presented that the analysis of waves in conducting media is possible utilizing the same approach as that for non-conducting media, except that many quantities become complex numbers in conducting media.
Challenges encountered in designing implantable antennas are presented in [29]. The author investigates the effect of lossy surrounding media on the bandwidth, radiation pattern and efficiency of an electrically small antenna. The effect on the reflection coefficient and impedance bandwidth of a spiral antenna is investigated using three different scenarios. In the first one the antenna is placed in free space, in the second it is surrounded by a lossless body phantom and in the last the antenna is placed in a lossy body phantom. It was found that the lossless medium surrounding the antenna changes the relative permittivity and therefore the resonant frequency is lowered but the impact on the bandwidth is very small. Whereas the lossy medium greatly enlarges the impedance bandwidth. However it is pointed out that the significance of

the bandwidth is questionable, due to the fact that it is more related to power lost in the surrounding medium than related to power radiated out of the body phantom. Further it is mentioned that the radiated power depends on the radial distance. The author proposes an encapsulation on the antenna in order to isolate the antenna from the lossy surrounding and reduce the strong near field coupling with the lossy medium which results in a decrease of losses. For this purpose the use of an insulating medium with low losses and a high dielectric constant is recommended, because of the high concentration of the near field in the low loss surrounding of the antenna.

5.1.2 Microstirp Antennas with Protective Cover

A microstrip antenna with a dielectric protective layer radiating into a high permittivity lossy medium is investigated in [30]. The effect of the width of the antenna and thickness of the dielectric protective layer on the relative effective permittivity and consequently on the resonance frequency is presented. It is shown that the relative effective permittivity decreases with increasing width of the antenna. It is pointed out that the reason for this phenomenon is because of the presence of a higher relative permittivity medium over the protective layer, which 'traps' the electromagnetic energy. The same relationship is shown for the thickness of the protective layer and the relative effective permittivity.
In [31] variation of resonant frequency of patch antenna due to accumulation of water over its surface is investigated. The survey is done for patch antennas without radome and with radome. The accumulation of water over the patch or the radome results in an exponential decrease of resonance frequency due to the fact that water is a dielectric medium. It is observed that the initial decrease of resonance frequency in the case of antennas without radome is much higher than in the case of antennas with radome. The shift in resonance frequency can be significantly reduced by use of a radome. Additionally it is observed that with increasing water layer thickness the impedance match of patch antenna with and without radome worsens. This effect is known for dielectric superstrates but in case of water it is stronger due to the high permittivity of water.

5.1.3 Antenna Loading

There are two types of antenna loading: pure reactive and resistive. Pure reactive loading appears when the antenna is loaded with a lossless medium. Reactive loading means that the antenna is covered by a lossy medium. The presence of a medium in the near field of an antenna causes, among other things, a shift in resonance frequency and deteriorates impedance matching. The near field is relatively strong and stores energy in the electric and magnetic fields, which directly result from current distribution. Consequently a medium in the near field of an antenna will affect the current distribution and causing the mentioned effects. In the case of a lossy medium, like the human body, power is extracted from the near field. Thus a protective cover between

antenna and lossy medium can decrease the influence and sensitivity of the antenna regarding loading. However the protective cover affects the antenna dimensions, the effective permittivity, the antenna input impedance and the bandwidth. As a consequence the antenna with protective cover has to be optimized for radiation into the body when applied to the body.
A measure known from hyperthermia is the usage of a so called water-bolus which is filled with deionized water. Deionized water has a high permittivity and a low conductivity and may be considered as a lossless medium, resulting in reactive loading of the antenna. The main reason for utilization of a water bolus in hyperthermia is tissue surface cooling in order to minimize hot spots. In some cases (see [32] and [33]) the usage of a water-bolus results in better electromagnetic coupling, due to reduction of the high difference between in permittivity at the skin interface and consequently the penetration depth of the electromagnetic field can be increased. In addition the return loss sensitivity is decreased. In [34] no effect of water bolus thickness on SAR penetration depth was found for a horn antenna.

5.2 Electromagnetic Simulation

5.2.1 Simulation Setup

The simulation setup is shown in Figure 5.1, it consists of a patch antenna covered by one or more protective layers and a simplified homogenous human body model situated above the protective layer. The medium representing the human body has a dielectric constant $\varepsilon_{\mathrm{r,p}} = 45$ and conductivity $\sigma_{\mathrm{p}} = 0.8$ S/m, representing average chest tissue permittivity and conductivity at $f = 868$ MHz. For the antenna a substrate with height $h_1 = 1.5$ mm and dielectric constant $\varepsilon_{\mathrm{r,sub}} = 10.2$ is used. The high dielectric constant of the substrate is chosen in order to keep the antenna dimensions small and concentrate the reactive field in this region.

5.2.2 Interaction between Antenna and Human Body

5.2.2.1 Antenna Detuning

In a first step an unloaded antenna is simulated, it has a patch width $w = 73.03$ mm and length $l = 52.88$ mm. The substrate dimensions are $174 \times 174\,\mathrm{mm}^2$ ($\lambda_0 = 345.38$ mm). A minimum return loss of 33.6 dB at $f = 871.2$ MHz is obtained, see Figure 5.2. As can be seen the unloaded antenna has a narrow bandwidth, which indicates a high quality factor. The radiation pattern is shown in Figure 5.2 (right), where $\phi = 0°$ and $\phi = 90°$ stand for cuts through the xz-plane and yz-plane, respectively.

By means of an electromagnetic field simulator the effect of a lossy homogeneous phantom on the antenna characteristics is simulated. The phantom is situated above

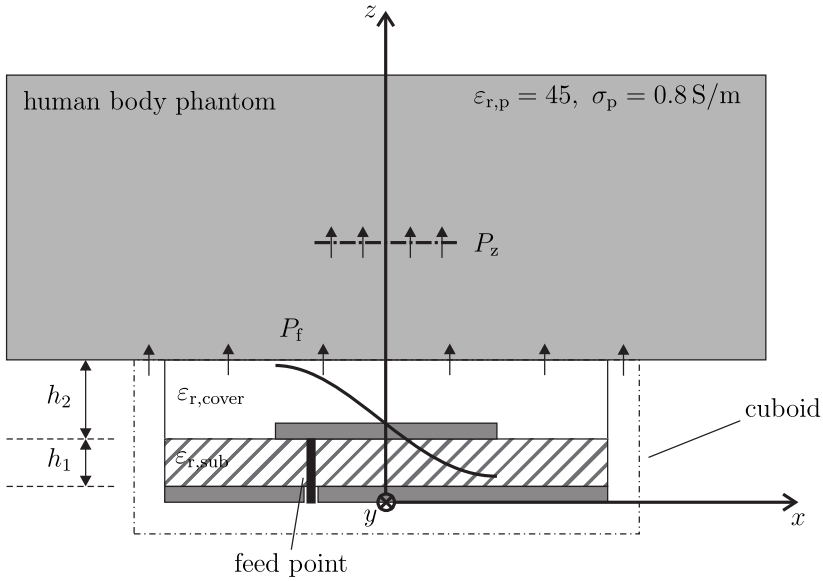

Figure 5.1: Simulation setup

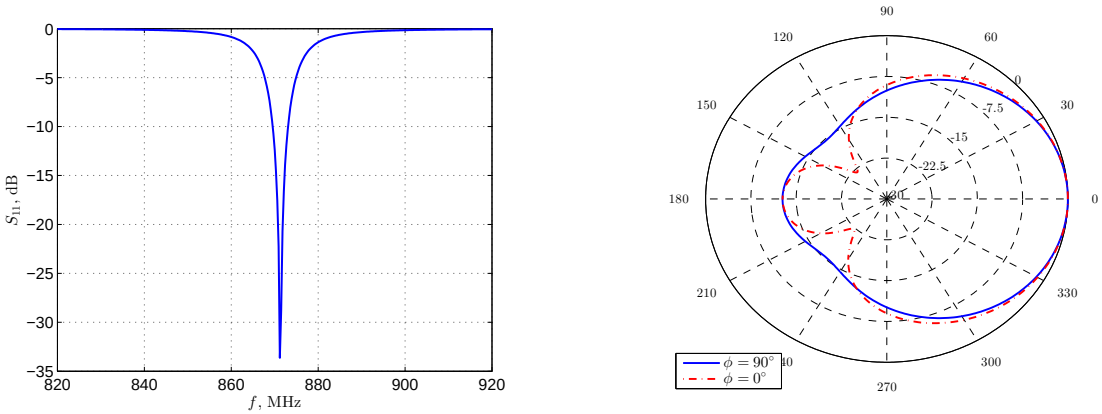

Figure 5.2: Return loss (left) and radiation pattern (right) for antenna in free space

a patch antenna and the distance between antenna and phantom is varied in order to investigate the impact of the antenna-phantom distance on the antenna matching. Figure 5.3 shows the sensitivity of the return loss with respect to a phantom situated at different heights above the antenna. A shift of the return loss minimum and additionally a return loss degradation, especially for distances shorter than 30 mm, is observed. At that distance the phantom seems to enter the near field region of the antenna. For greater distances the shift in frequency of the return loss minimum may result from reflections at the air-phantom interface. Furthermore the reflection coefficient is shown in the smith chart for different distances (Figure 5.3, right). The shown effect points to a reduction of the quality factor of the antenna.

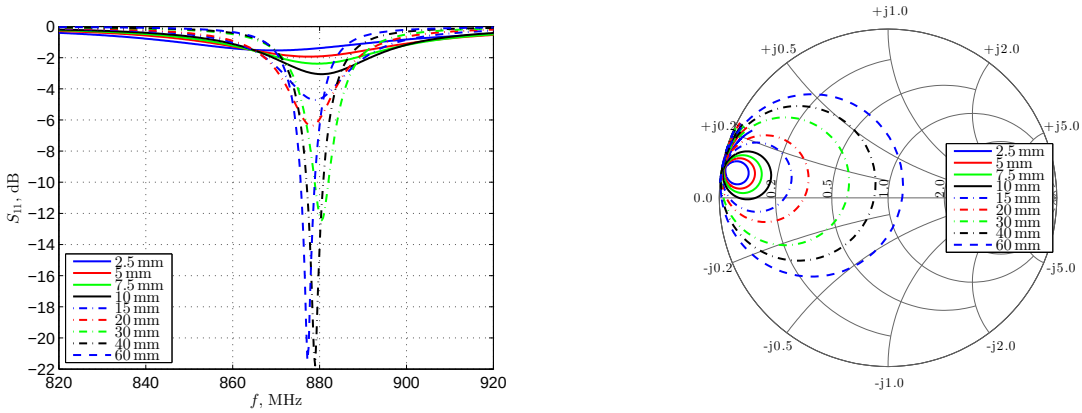

Figure 5.3: Return loss variation of patch antenna, for different distances h_2 between antenna and phantom

The real and imaginary part of the antenna impedance as a function of frequency for different distances is depicted in Figure 5.4. The real part decreases with decreasing

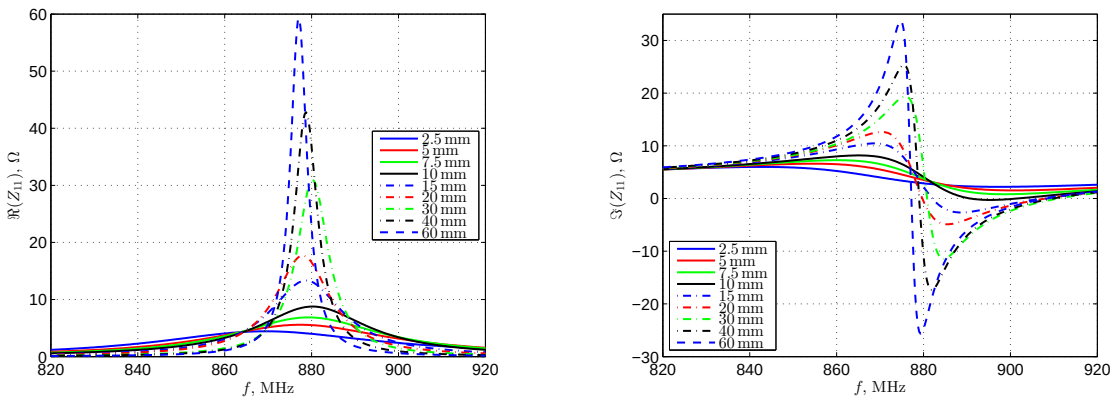

Figure 5.4: Real and imaginary part of antenna impedance for different distances h_2 between antenna and phantom

distance between antenna and phantom resulting from the severe loading. For the

imaginary part a loss of symmetry about the resonance frequency can be observed, where the reactance becomes more and more inductive for smaller distances and finally is non-resonant for distances below 7.5 mm.
Figure 5.5 shows the real and imaginary part of the antenna impedance for a loss-free ($\sigma_\mathrm{p} = 0$) and lossy ($\sigma_\mathrm{p} = 0.8$ S/m) phantom situated 1 cm above the antenna. As

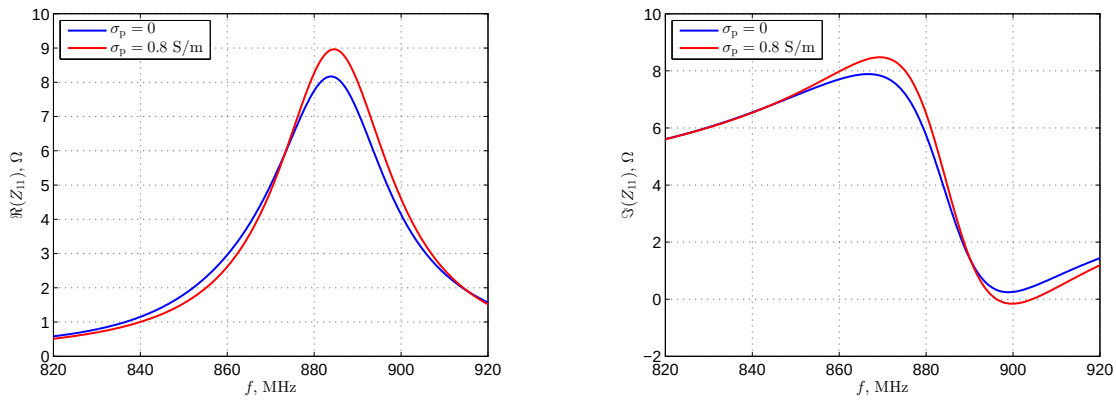

Figure 5.5: Real and imaginary part of antenna impedance for loss-free and lossy phantom

can be seen the phantom losses have a minor effect on the input impedance, thus the detuning results mainly from dielectric loading.
A simplified model of the antenna loaded by a human body is shown in Figure 5.6 [35]. The loading can be represented as a series inductance and a resistor parallel to

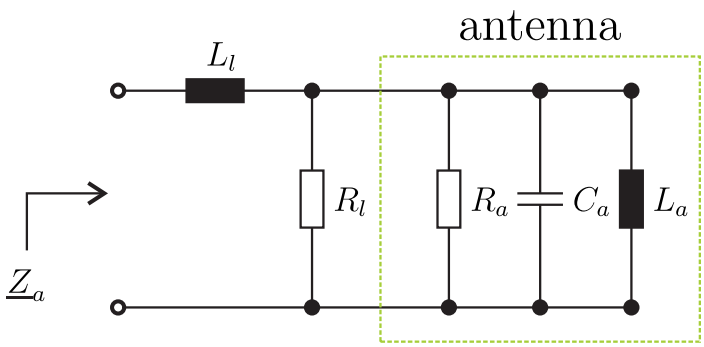

Figure 5.6: Circuit model of loaded antenna

a resonator, which represents the antenna. The loading is a function of the distance between the antenna and the body and depends on the body structure. It can be concluded that the antenna impedance is almost a short for very small distances between antenna and dielectric and therefore critical to match with conventional passive matching networks. Consequently the effect of the human body has to be taken into account during antenna design.

5.2.2.2 On-Body Matched Antenna

In a second step an antenna covered by a 1 cm thick air layer/gap, which can be realized of Styrofoam is investigated. The antenna was optimized in order to obtain a good return loss. The electric and magnetic field components along the z-axis above the center of the patch antenna are shown in Figure 5.7. It can be seen that the x-

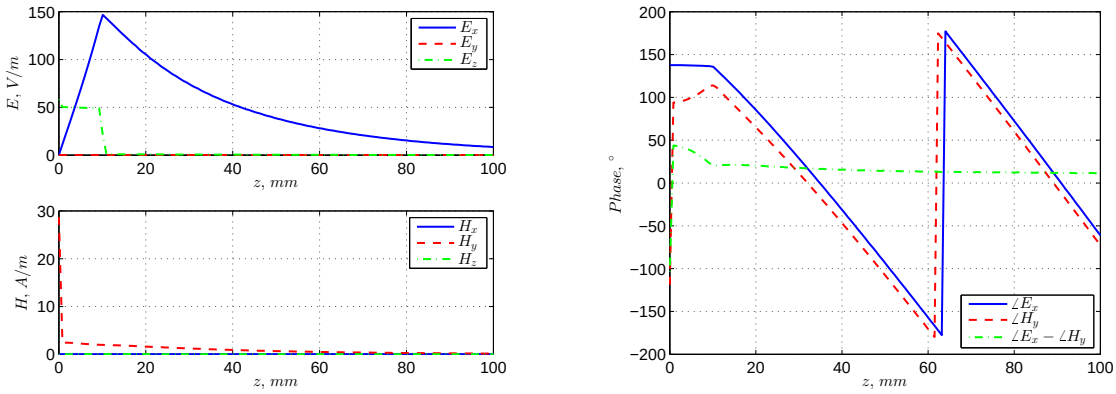

(a) (b)

Figure 5.7: Magnitude (a) and phase (b) of electric and magnetic field components along $x = y = 0$

component of the E-field builds up in the foam layer and decays inside the phantom. The electric field normal to the antenna (E_z) is constant in the foam layer and abruptly changes at the foam-phantom interface. This is due to the difference in permittivity between foam layer and phantom. This is in agreement with the boundary conditions for the electric field. Those state that the normal component of the displacement flux $\vec{D}$ is continuous across an interface between two dielectric media, resulting in:

$$\varepsilon_1 \vec{E}_{1n} = \varepsilon_2 \vec{E}_{2n}, \tag{5.2.1}$$

with $\vec{E}_{1n}$ and $\vec{E}_{2n}$ the normal components of the electric field at the boundary, and ε_1 and ε_2 the permittivity of medium 1 and 2, respectively. The tangential components of the electric field are continuous across the interface:

$$\vec{E}_{1t} = \vec{E}_{2t}. \tag{5.2.2}$$

The tangential magnetic field component $\underline{H}_y$ is also continuous at the interface and decays inside the foam layer and phantom. On the right side of Figure 5.7 the phase of the dominant field components ($\underline{E}_x$,$\underline{H}_y$) inside the phantom is depicted. The phase difference of those field components is around 20° at the air-phantom interface and decreases inside the phantom. Such that it can be concluded that the reactive fields are not dominant (at least along the considered direction) and that the region inside

the phantom can be identified as radiating near field or Frensel region. In this region the shape of the radiation pattern may vary with distance. Based on that assumption that the reactive near field is not dominant, the optimization of the antenna sensor is manly based on evaluation of the z-component of the real part of the Poynting vector. Figure 5.8 shows the electric and magnetic field components along the x-direction (left) and y-direction (right) in the middle of the foam layer between the antenna and the phantom. The dominant electric filed components are E_{x} and E_{z}, where the dominant magnetic field components are H_{y} and H_{z}. Calculating the Poynting vector from

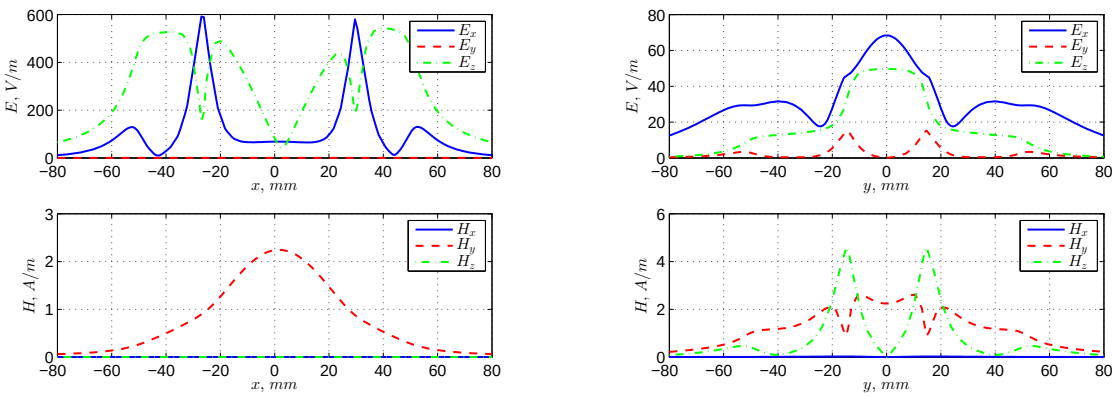

Figure 5.8: Electric and magnetic field in-between antenna and phantom

the existing field components shows that, beside a Poynting vector z-component also components into x and y-direction are existent, which could lead to increased coupling between patch elements of an antenna array.
Figure 5.9 (left) illustrates the real part of the Poynting vector z-component intensity at a depth of 3 cm inside the phantom in a fragment of the xy-plane. This fragment has the size of $6 \times 6\,\mathrm{cm}^2$, which is approximately the size of the cross-section of the heart. The corresponding electric and magnetic fields are depicted on the right of Figure 5.9. It can be seen that the radiated power is focused at that depth inside the phantom, resulting in a maximum strength of reflected power from an object located at that depth.
Figure 5.10 shows contour plots of the real part of $\underline{\vec{S}}_{\mathrm{z}}$ at four depths inside the phantom for a 1 cm thick foam layer. The contour lines are plotted at -3 dB steps such that the darkest area in the center of the plot represents the 3 dB beam area. Defocusing of the radiated power with increasing distance from the antenna can be observed.

5.2.3 Definition of Parameters

In order to quantify the antenna characteristics the near-field directivity, coupling efficiency and 3 dB beam area are defined in the following and evaluated. The near-field directivity (NFD) was defined for a horn antenna in [36] as:

$$NFD = P_{\mathrm{f}}/P_{\mathrm{T}}, \tag{5.2.3}$$

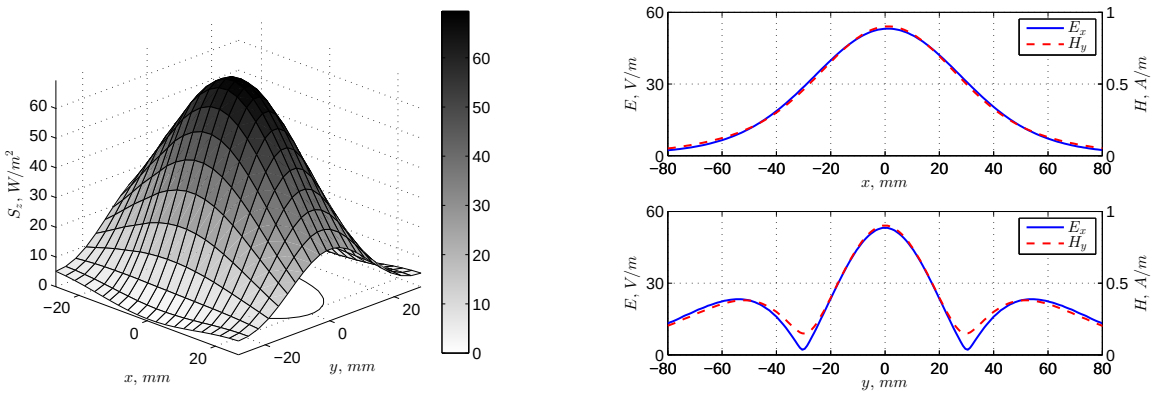

Figure 5.9: Real part of z-component of the Poynting vector at $d = 3$ cm in xy-plane (left). Tangential electric and magnetic field components in the E-plane and H-plane at $d = 3$ cm (right)

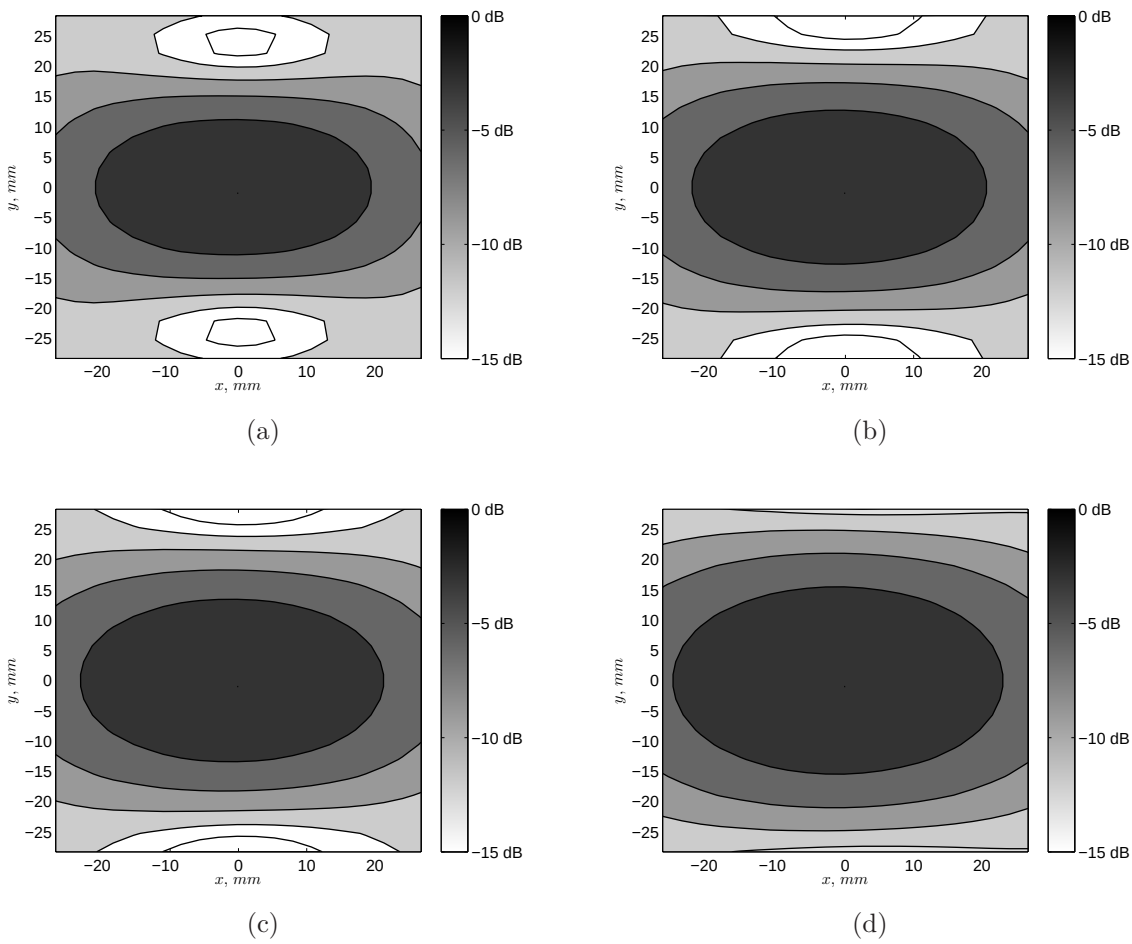

Figure 5.10: Contour plot of real part of Poynting vector z-component in xy-plane at different depths: 1 cm (a), 2 cm (b), 3 cm (c) and 4 cm (d)

where P_f is the power radiated into broadside direction through the face of a cuboid enclosing the antenna and P_T is the total radiated power through the surface of the cuboid, see Figure 5.1. The definition of the coupling efficiency was given also in [36] as the ratio of the power radiated through the front of the antenna overlapping with the face of a cuboid to the power fed to the antenna. This measure is used in a slightly altered form due to the fact that a patch antenna has no distinct front like a horn antenna. Instead of the power P_f we integrate the real part of the Poynting vector over a surface ($6 \times 6\,\mathrm{cm}^2$) located at a depth of 3 cm inside the phantom and obtain the power P_z:

$$e_\mathrm{c} = \frac{P_\mathrm{z}}{P_{in}}. \tag{5.2.4}$$

The 3 dB beam area is used in order to assess the focusing of power radiated by an antenna inside the phantom at a certain depth, similar to the definition of the near-field 3 dB beam radius in [37] for circular apertures of currents (electric, magnetic and Huygen's). It is defined as the radius of the smallest circle which contains all points where the Poynting vector is higher than -3 dB relative to the strongest value in that plane, measured from the center of the beam. This definition of the 3 dB beam radius is applicable for a circular aperture due to the fact that the resulting field distribution is concentric, in other cases it is not. Therefore a 3 dB beam area which contains all points where the Poynting vector is higher than -3 dB relative to the strongest value in that plane is defined. This measure is used in order to assess the focusing of power radiated by an antenna inside the phantom at a certain depth.

5.2.4 Investigation of Top Dielectric Layer

The shown effect of antenna loading varies additionally with different subjects due to individual body properties. A simple method to mitigate the interaction of a lossy dielectric load with the reactive near filed is to use a protective superstrate (dielectric cover). In the following it is tried to design a patch antenna covered by a dielectric layer in order to mitigate the detuning effect. Different dielectric materials with varying heights will be investigated as superstrate. In addition the effect on the power radiated into the human body is examined.
During simulation the patch width ($w = 28$ mm) is kept constant and the patch length ($l \approx 5$ mm) is altered to obtain a resonance frequency of 868 MHz for the different setups. Additionally the feed point is changed in order to obtain an input impedance close to $50\,\Omega$.

5.2.4.1 Variation of Superstrate Permittivity

Figure 5.11 depicts the near-field directivity and coupling efficiency as a function of the dielectric constant of the cover material with height $h_2 = 1$ cm. Near field directivity is lowest for an air gap ($\varepsilon_\mathrm{r} = 1$) and increases to more than 98% for covers made of

high permittivity materials. It is highest for $\varepsilon_r = 10$ and decreases slightly for $\varepsilon_r = 20$. Coupling efficiency e_c is highest for $\varepsilon_r = 5$, but decreases for $\varepsilon_r = 20$ nearly to the

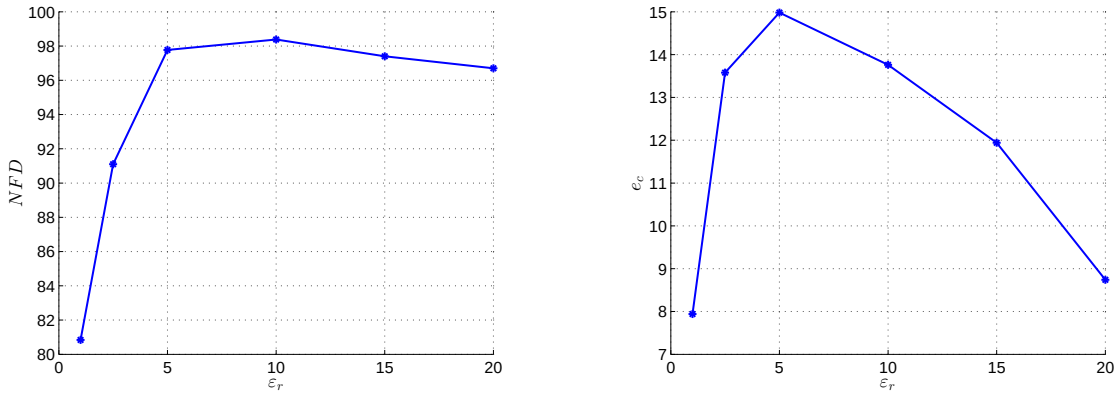

Figure 5.11: Near-field directivity and coupling efficiency vs. cover permittivity

same value as for the air gap despite high near-field directivity. In Figure 5.12, the Poynting vector intensity, for a power of 1 W fed to the structure, is shown for a cover permittivity of 1, 10 and 20. The lower dotted line indicates the phantom interface, the upper shows the location of the surface for calculation of P_z. Especially a formation of side beams in the xz-plane for the higher permittivity cover and in the yz-plane for the air gap can be seen. The near-field directivity alone is not a good measure to assess the power flow for this application, thus it is necessary to evaluate the Poynting vector intensity in the yz-plane and xz-plane. A comparison of Poynting vector intensity leads to the conclusion that minimal side beam formation and backward radiation is achieved with a cover material with a permittivity $\varepsilon_r = 10$.
In Figure 5.13 the 3 dB beam area and quality factor are depicted as a function of the cover permittivity. The 3 dB area is biggest for $\varepsilon_r = 2.5$ and $\varepsilon_r = 5$ and almost the same for the other simulated permittivities. In conjunction with the coupling efficiency it is possible to assess the focusing and amount of power that can be reflected by an object or part of that object located at that depth. As can be seen the quality factor decreases with increasing permittivity, which points the higher loading of the antenna sensor.

5.2.4.2 Variation of Superstrate Height

NFD and e_c versus cover height h_2 is depicted for three different cover permittivities in Figure 5.14. Increasing the cover height h_2 slightly increases e_c for cover materials with $\varepsilon_r = 10$ and $\varepsilon_r = 20$. For $\varepsilon_r = 1$ coupling efficiency increases with decreasing height h_2. Near-field directivity is nearly constant for materials with higher dielectric constant, but reduces strongly for the air layer. This means that the amount of power radiated into backward direction and laterally increases for $\varepsilon_r = 1$ with increasing h_2. In Figure 5.15 the 3 dB beam area and quality factor versus cover height are illustrated.

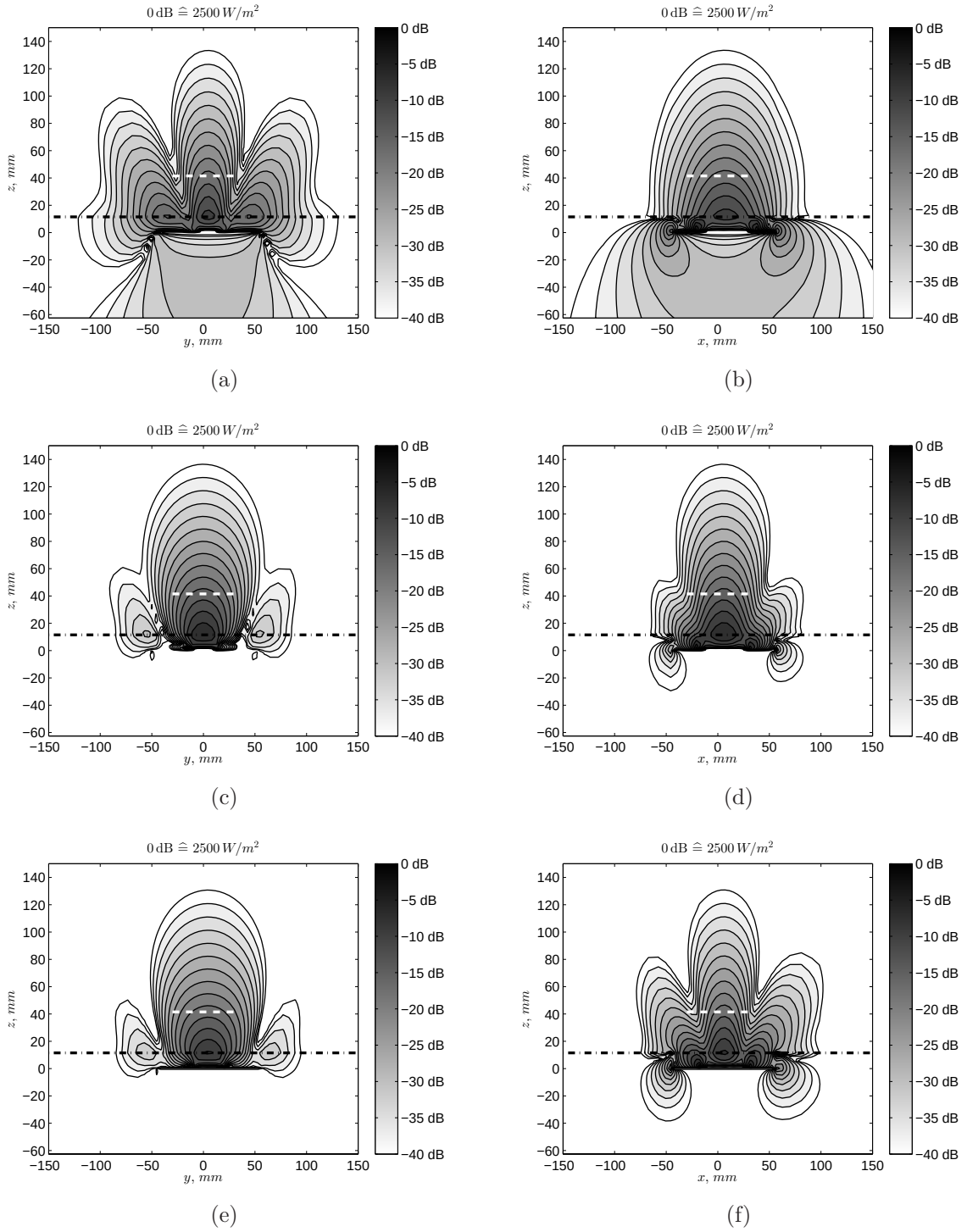

Figure 5.12: Poynting vector z-component intensity in yz-plane (a,c,e) and xz-plane (b,d,f) for cover permittivity 1 (a,b) ,10 (c,d)and 20 (e,f)

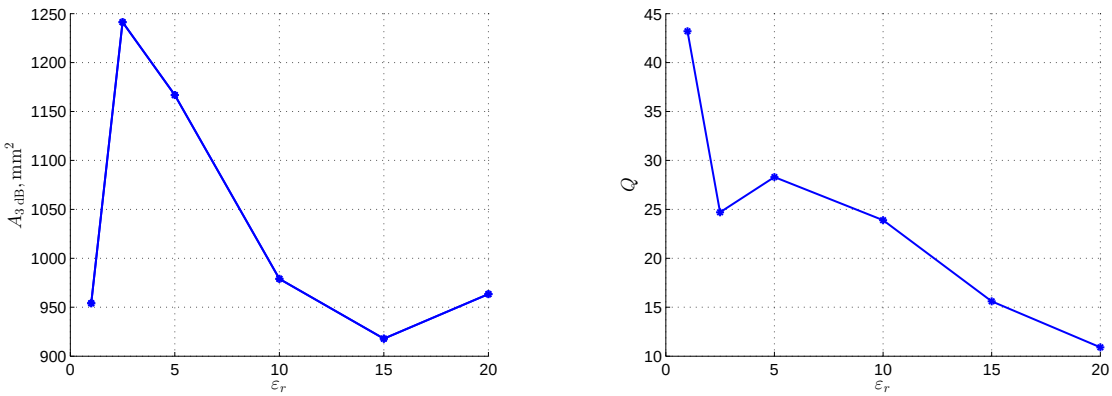

Figure 5.13: 3 dB beam area (a) and quality factor (b) vs. cover permittivity

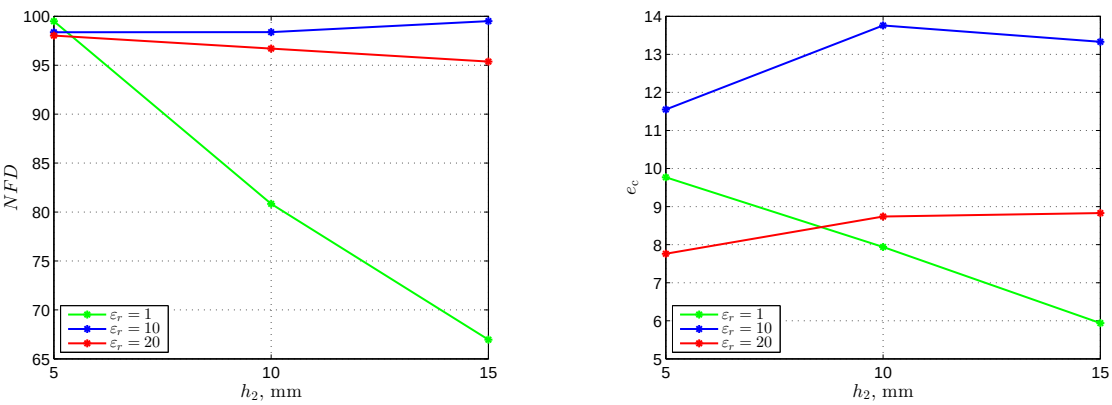

Figure 5.14: Near-field directivity (a) and coupling efficiency (b) vs. cover height

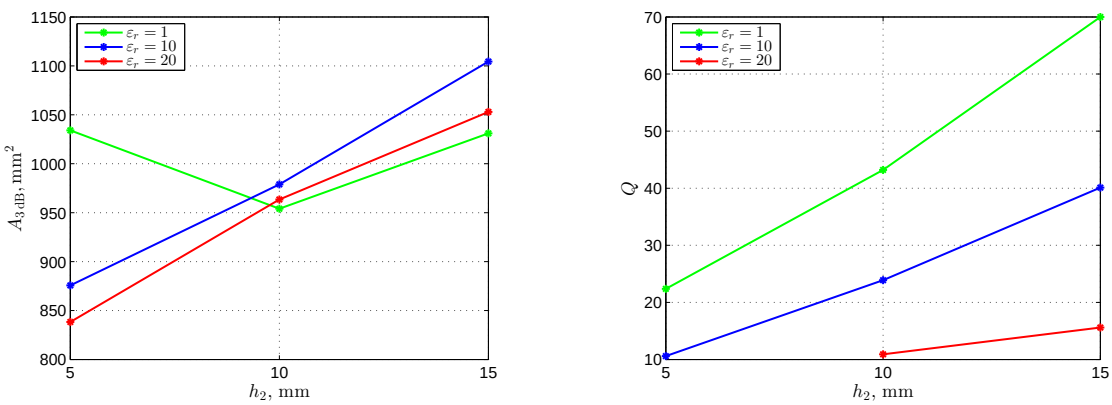

Figure 5.15: 3 dB beam area (a) and quality factor (b) vs. cover height

The beam area increases with increasing h_2 for $\varepsilon_r = 10$ and $\varepsilon_r = 20$. Quality factor increases with increasing height h_2 for the shown permittivities.
Cover height affects the power distribution inside the phantom as can be seen in Figure 5.16 for $\varepsilon_r = 10$. For $h_2 = 0.5$ cm side beam are more pronounced in the xy-plane and

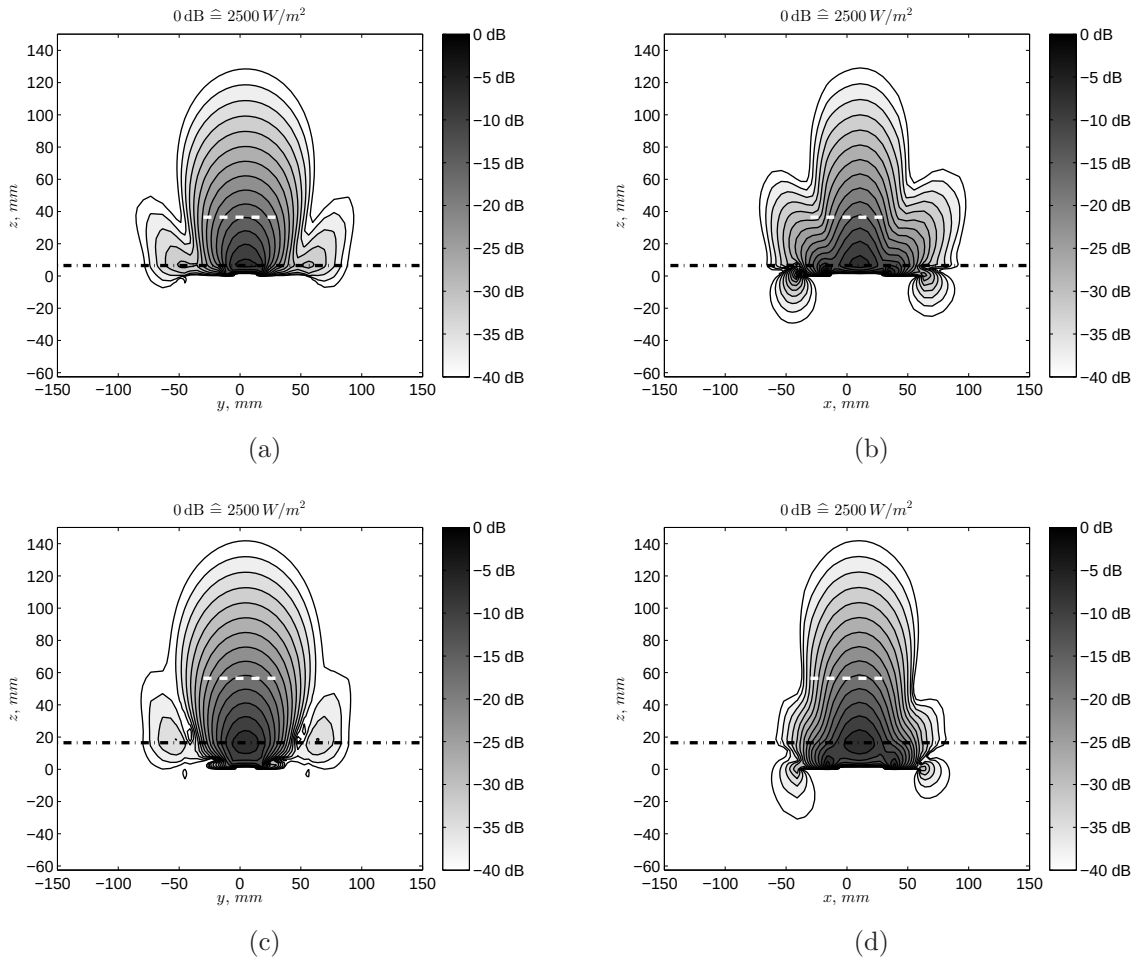

Figure 5.16: Poynting vector z-component intesity in yz-plane and xz-plane, cover height 0.5 cm (a, b) and cover height 1.5 cm (c, d), $\varepsilon_r = 10$

reduce for $h_2 = 1.5$ cm. For the other two materials higher side lobes formation can be observed.
At this point it can be concluded that a thick superstrate with the same permittivity as the substrate gives the best results. Apart from that standard substrate thicknesses are available from 0.1 - 3.2 mm, which is at least one third of the optimum height. Thus superstrate thicknesses of 5 mm or higher are only feasible by stacking several dielectrics. Another option is to use liquids with the needed permittivity which have to be filled into a shell.

5.2.4.3 Variation of Patch Width

The effect of patch width on coupling efficiency is shown in Figure 5.17, the patch width is varied by ±40%. Decreasing patch width result in decreased coupling efficiency,

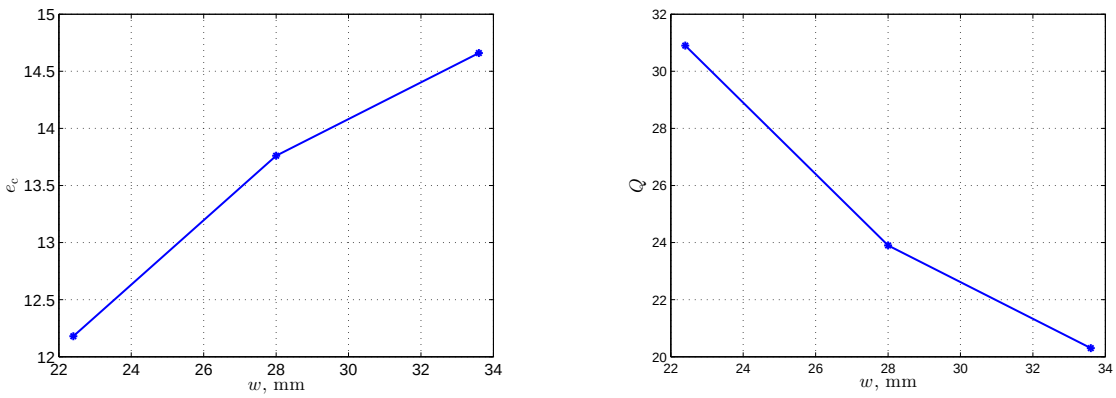

Figure 5.17: Coupling efficiency and quality factor vs. variation of patch width

near-field directivity is almost constant. On the one hand a larger patch width gives a better radiation performance, on the other it reduces the input impedance of the patch antenna such that it is difficult to get an impedance close to 50 Ω. The quality factor of the sensor versus patch width is shown in Figure 5.17 (right), it decreases with increasing patch width. This indicates a stronger loading of the sensor.

5.2.4.4 Variation of Ground Plane Size

The effect of ground plane size on NFD and e_c is illustrated in Figure 5.18. For smaller ground planes the near-field directivity decreases, the coupling efficiency is almost unaffected. Figure 5.19 shows the real part of the Poynting vector z-component

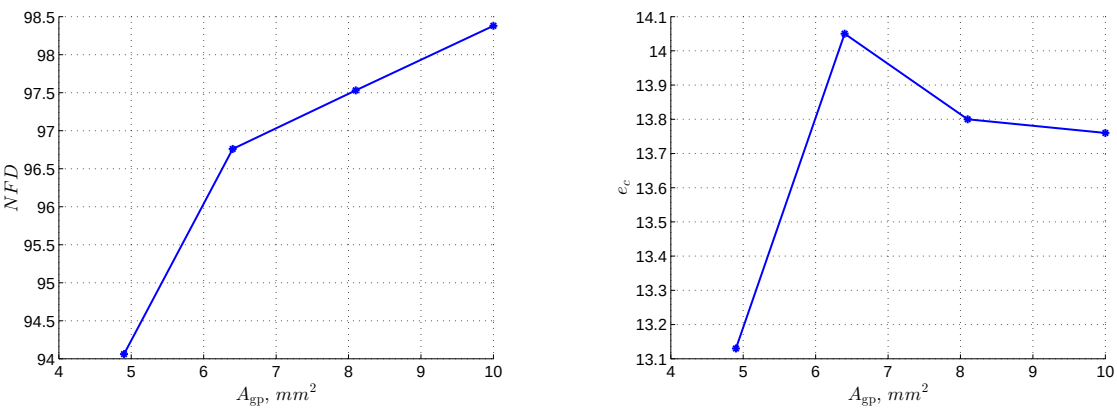

Figure 5.18: Near-field directivity (a) and coupling efficiency (b) vs. ground plane size

intensity in the yz-plane (a) and xz-plane (b) for a ground plane size of $49\,\mathrm{cm}^2$ for a cover permittivity $\varepsilon_\mathrm{r} = 10$. It can be seen that a reduction of ground plane leads to a

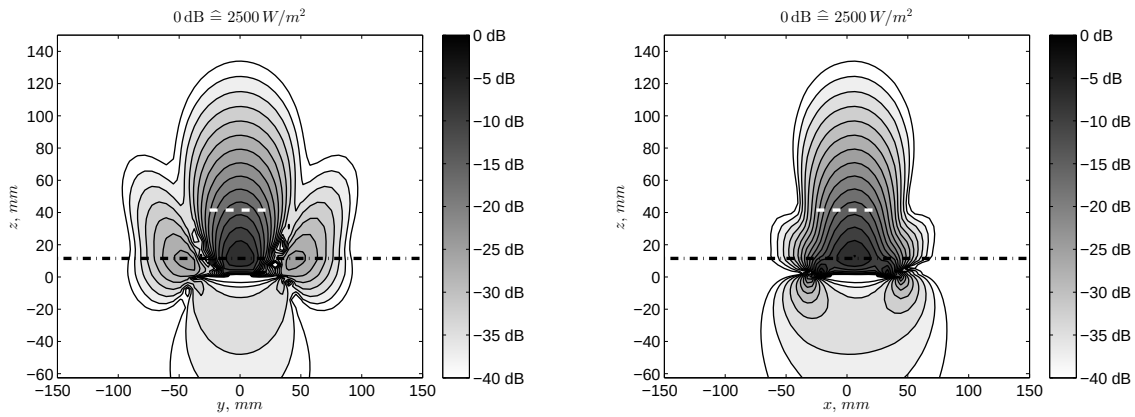

(a) (b)

Figure 5.19: Poynting vector z-component intensity in yz-plane (a) and xz-plane (b) for reduced ground plane size

distinct formation of side lobes in the yz-plane, compare to Figure 5.12. Also in both planes a smaller ground plane results in an increased backward radiation. This goes along with smaller NFD for smaller ground planes.

5.2.4.5 Return Loss Sensitivity

The sensitivity of the reflection coefficient with respect to variation of the dielectric properties of the phantom is examined. Figure 5.20 shows the sensitivity of the return loss for cover materials with $\varepsilon_\mathrm{r} = 1$ (a) and $\varepsilon_\mathrm{r} = 10$ (b), where the permittivity and conductivity of the phantom was varied by $\pm 10\%$ (initially: $\varepsilon_\mathrm{r,p} = 45$, $\sigma_\mathrm{p} = 0.8$ S/m). It can be seen that the sensitivity of the return loss with respect to variations of the phantom dielectric properties is minor in both investigated cases. Furthermore the effect of permittivity variation in stronger than the effect of variation of conductance. Moreover it is observed that a decrease in permittivity shifts the return loss minimum to lower frequencies, whereas a decrease in conductivity has the opposite effect. The low sensitivity may results from the fact that the reactive near field is concentrated in the region below the phantom.
Unconsidered in this investigation is the choice of the feed point, there may be other feed points where the input impedance sensitivity is higher. It can be concluded that even an air layer is sufficient to decrease return loss sensitivity if the antenna is designed for that certain scenario. In addition sensor-phantom distance variation may have stronger effect on return loss than variation of dielectric properties.

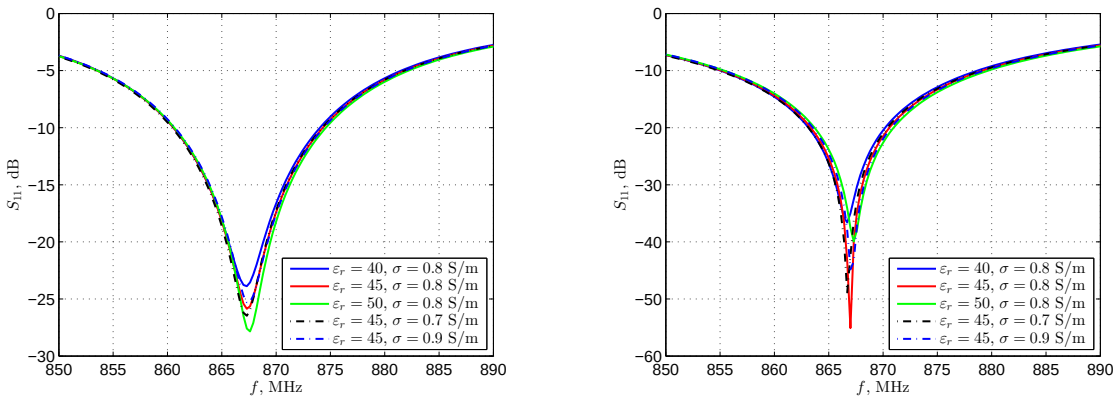

(a) (b)

Figure 5.20: Return loss sensitivity for 1 cm thick cover: (a) $\varepsilon_r = 1$ and (b) $\varepsilon_r = 10$

5.2.5 Investigation of Layered Dielectric Cover

In this section the effect of a layered dielectric cover is investigated. The superstate is realized by two stacked dielectrics, where the lower dielectric has a permittivity $\varepsilon_{\mathrm{r,l}} = 10$. The permittivity of the upper dielectric is varied ($\varepsilon_{\mathrm{r,u}} = 20$, 30 , 40 and 75) during simulation. Materials for the upper layer with a permittivity higher than the substrate are chosen is order to decrease the difference in permittivity between sensor and phantom. The effect of the permittivity of the upper dielectric and the combination of different cover heights on the aforementioned quantities is investigated. In this scenario it was necessary to lessen the patch width to 23 mm (reduction of 17.86 %), otherwise an input impedance close to 50 Ω was not achievable for all setups.
Simulation results show that coupling efficiency is approximately 10% and $NFD = 98\,\%$ for the investigated setups. Comparing with the single layer dielectric cover with $\varepsilon_{\mathrm{r,l}} = 10$, these measures decreases the coupling efficiency. The Poynitng vector z-component intensity is depicted in Figure 5.21. As can be seen, the permittivity of the upper dielectric cover has a minor influence on the power distribution. Side beam are slightly more pronounced for covers with lower permittivity.
In the field of Hypothermia a so called water bolus is used in order to increase energy coupling. A water bolus is a pillow filled with distilled or fresh water ($\varepsilon_{\mathrm{r,l}} = 75$), where conductivity is the main difference between distilled and fresh water. A dielectric layer made of a shell filled with an elastic dielectric material would be beneficial in order to compensate irregular body contours. Additional in the case of water as dielectric material, the realization is very easy. The shell is made of a thin plastic sheet and can be neglected in simulation.
Based on those considerations it was decided to further investigate the effect of a water bolus with $\varepsilon_{\mathrm{r,u}} = 75$. Table 5.1 shows the results for different dielectric cover h_{diel} and bolus h_{bolus} heights. As can be seen the effect on e_{c} and NFD is small. For lower dielectric cover heights smaller quality factors are obtained, which indicates higher loading of the sensor. Additionally the height of the bolus has a minor effect on the quality factor.

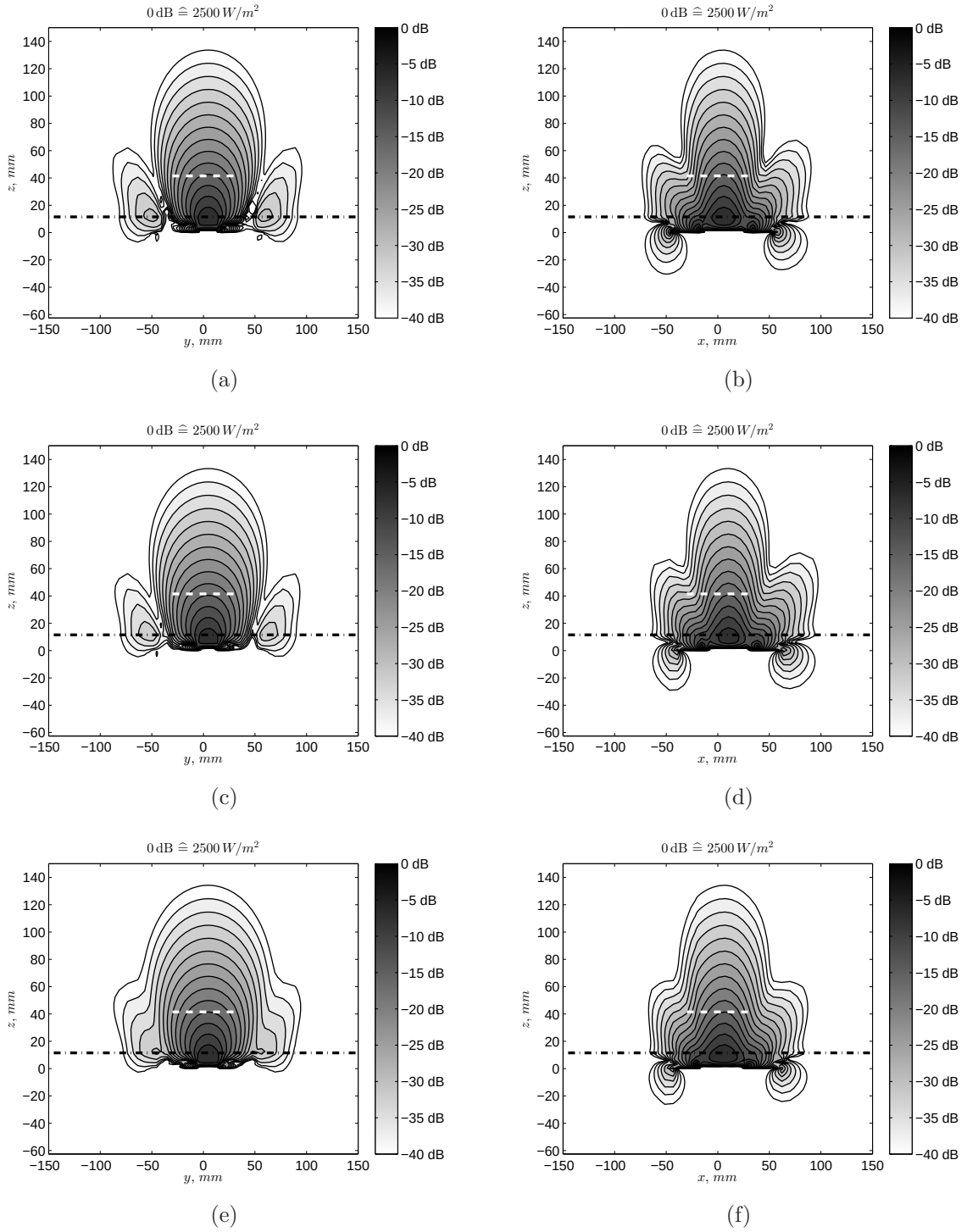

Figure 5.21: The Poynitng vector z-component intensity in yz-plane and xz-plane, $\varepsilon_{\mathrm{r,u}} = 20$ (a, b) $\varepsilon_{\mathrm{r,u}} = 40$ (c, d) and $\varepsilon_{\mathrm{r,u}} = 75$ (e, f)

h_{diel}, cm	h_{bolus}, cm	e_{c}, %	NFD %	Q
0.5	0.5	10.46	98.5	9.9
0.5	1.0	11.03	98	7.66
1	0.5	10.86	98.5	19.13
1	1	12.54	97.9	20.39

Table 5.1: Coupling efficiency, 3 dB beam area and quality factor Q for different layer heights

5.2.6 Final Antenna Configuration

Due to the investigation and practical reasons it was decided to use a material for the lower dielectric cover with a standard height of 3.2 mm and permittivity $\varepsilon_{\text{r,l}} = 10$. The upper dielectric is realized by a water bolus with a height of 5 mm. For this configuration also a reduction of patch width ($w = 15$ mm) was necessary in order to get an input impedance close to $50\,\Omega$. The sensor dimensions and simulated coupling efficiency, 3 dB beam area and quality factor are listed in Table 5.2.

width × length, cm	ground plane, cm	e_{c}, %	3 dB-area, mm^2	Q
1.5 × 4.94	6.6 × 9.95	9.5	990.41	12.63

Table 5.2: Coupling efficiency, 3 dB area and quality factor Q for different layer heights

Figure 5.22 illustrates the real part of the Poynting vector $\underline{\vec{S}}_{\text{z}}$ for the final antenna sensor. As can be seen backward radiation and formation of side maxima is negligible.

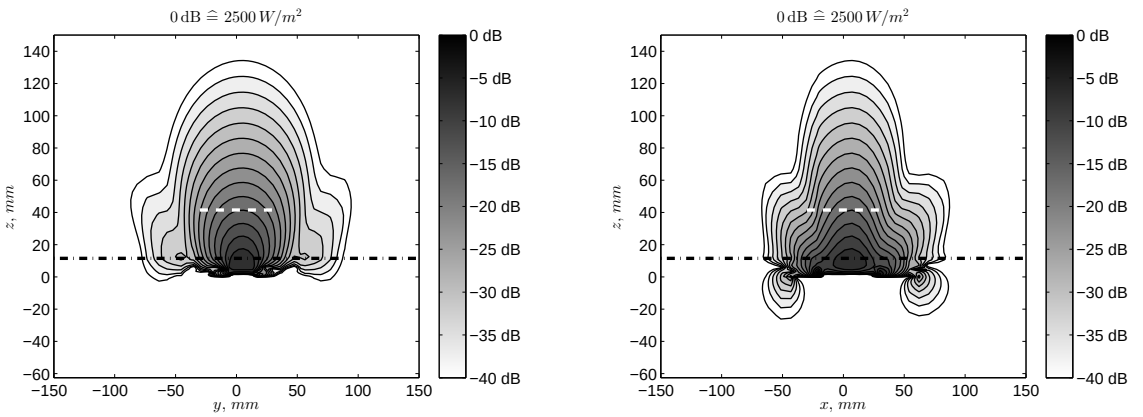

(a) (b)

Figure 5.22: Poynting vector z-component intensity in yz-plane (a) and xz-plane (b)

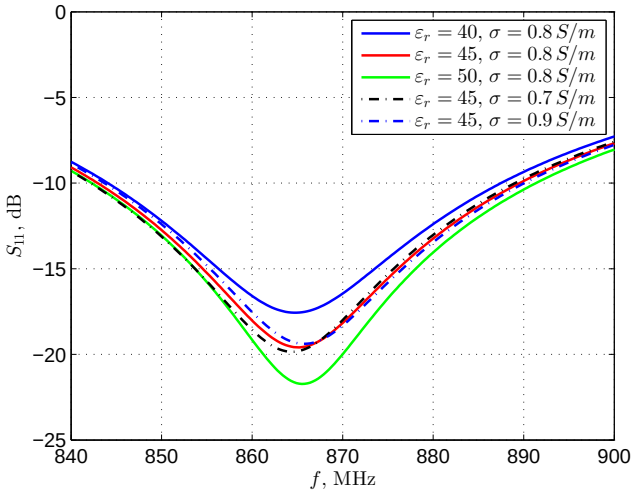

Figure 5.23: Return loss sensitivity

The return loss sensitivity of the final sensor design is illustrated in Figure 5.23. Due to the low quality factor the sensor exhibits a broad impedance bandwidth. Permittivity variations have a stronger effect on return loss than conductivity variations. The return loss sensitivity is stronger than in the other investigated setups but still acceptable.

In a last step the antenna structure applied to a human body model is simulated. The human body model is defined by a volume with an equidistant mesh, where a tissue with electrical and thermal parameters is assigned to each mesh cell. In order to reduce simulation time only the chest part, which is extracted from the whole body model, is used in the simulation. The intention is to investigate the field distribution inside and outside of the human body and the effect on the antenna characteristics (return loss, resonance frequency). Another interesting point is to find out which parts of the heart are illuminated by the antenna.
Figure 5.24 shows the simulated return loss and antenna impedance for the case that the antenna structure is applied to the human torso (blue curves). As can be seen the return loss is degraded considerably, taking a look at the input impedance it becomes clear that the degradation comes from an increase of the real part of the antenna impedance $\underline{Z}_\mathrm{T}$. The increased real part of the antenna impedance points to a lower antenna loading. In contrast to the simple homogeneous phantom the human body model is a multilayer structure with an uneven surface. Such that the reflections at the inner interfaces and the surface unevenness are not considered in simulations with the homogeneous phantom. Additionally the permittivity of the first layers of the human body torso model (skin, fat and cartilage) is less than the permittivity of the homogeneous phantom. In order to figure out where this discrepancy comes from, a three-layer phantom was simulated. It consists of a skin layer ($\varepsilon_\mathrm{r} = 41.6$, $\sigma = 0.86\,\mathrm{S/m}$, $d = 2\,\mathrm{mm}$), a fat layer ($\varepsilon_\mathrm{r} = 5.47$, $\sigma = 0.05\,\mathrm{S/m}$, $d = 3\,\mathrm{mm}$) and a muscle layer ($\varepsilon_\mathrm{r} = 55.11$, $\sigma = 0.93\,\mathrm{S/m}$). The return loss and input impedance for the homogeneous (red curve) and layered phantom (green curve) are also depicted

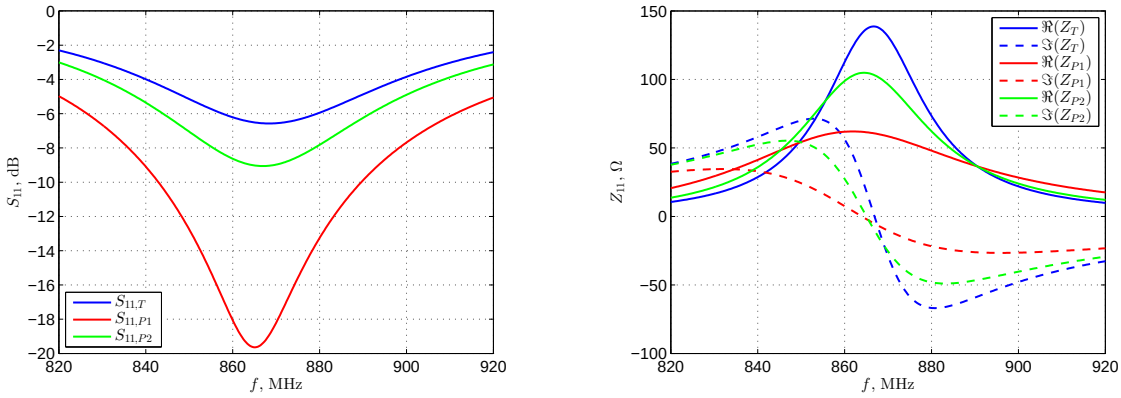

Figure 5.24: Return loss and input impedance

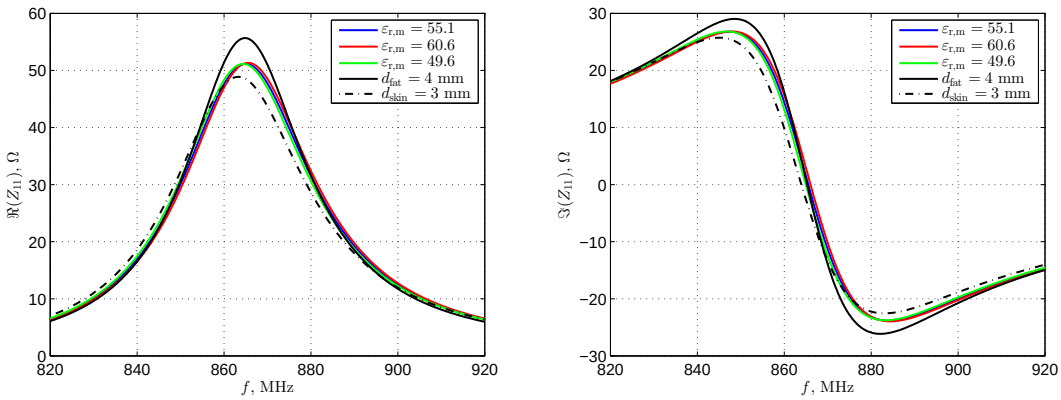

(a) (b)

Figure 5.25: Input impedance sensitivity for layered phantom

in Figure 5.24. From the comparison it can be seen that the impact on the resonance frequency is negligible, but the real part of the antenna impedance increased significantly for the three layer phantom and the torso model. The antenna loading in case of the human torso ($Q = 32.25$) and layered phantom ($Q = 23.26$) is less than for the homogeneous phantom. Higher quality factor implicates lower loading and thus the return loss is more sensitive to dielectric property variations. In the case of the layered phantom the coupling efficiency increased to $e_c = 13.73\,\%$ in comparison with the homogeneous phantom. Backward and side radiation is unaffected.

The feed point of the antenna is shifted in order the achieve matching for the layered phantom and a sensitivity analysis is conducted. Figure 5.25 shows the input impedance sensitivity for the layered phantom. During the analysis the permittivity of the muscle layer $\varepsilon_{r,m}$ was varied by $\pm 10\,\%$ and the thickness of the skin and fat layer was increased by 1 mm. The blue curve represents the initial setup with the values mentioned above. As can be seen the effect of variation of muscle layer permittivity is neglectable. Variation of skin and fat layer thickness affect mainly the real part of the

input impedance, however the effect is minor.
The Poynting vector z-component intensity is shown in Figure 5.26 when the sensor is applied to the torso model. It can be seen that only a portion of the heart is illuminated by the antenna and that the backward and side radiation in negligible. Thus it is assumed that placing the antenna at different positions on the chest and illuminating different heart regions may give some information about the heart phase related the that region, by evaluation of the reflected signal.

5.2.7 Return Loss Measurement

Figure 5.27 illustrates the measured and simulated real and imaginary part of the antenna impedance, for the antenna applied the a homogeneous phantom (a)-(b) (except curve Sim 2, layered phantom) and human torso (c)-(d). The experimental homogeneous phantom consists of a container filled with a tissue-equivalent liquid. The measurement was repeated several times to prove reproducibility. It can be seen in Figure 5.27 (a)-(b) that there is a deviation between measurement and simulation. The higher resonance frequency in the measurement may result from fabrication tolerances, which have a stronger impact due to the high dielectric medium in which the antenna is embedded. The higher real part may result from the fact that the container material has a low dielectric constant. Simulation results are shown for a homogeneous (black dashed curve) and layered (black dashed curve) phantom.
Figure 5.27 (c)-(d) shows a good match between simulation and measurement for the antenna applied to human torso. In measurement the antenna was applied to different positions on the chest of two individuals (Meas 1-3: individual 1). The deviation of the input impedance for the shown measurements is higher than expected. Resonance frequency as well as the real part of the antenna impedance exhibit quite large variation.

5.3 Conclusion

The investigation shows that the defined parameters in section 5.2.3 alone are not sufficient to assess the sensor characteristics. Thus it is necessary to evaluate the Poynting vector intensity plots in tandem with the parameters in order to get an idea of the effect of different covers. The effect on power coupling is in the range of a few percent. However the different dielectric covers strongly influence the field distribution and consequently backward and side radiation.
For a homogeneous phantom the return loss sensitivity with respect to variations of the dielectric properties is small, even for an air gap when the antenna is designed for such a scenario. The cover permittivity and height influence the sensor quality factor. An oversimplified homogeneous phantom is suboptimal in order to investigate antenna loading and return loss sensitivity. Due to the fact that it loads the antenna sensor to a greater extent than the human body model.

Measurement and simulation show a good agreement, however the variations in return loss are high for different positions and individuals.

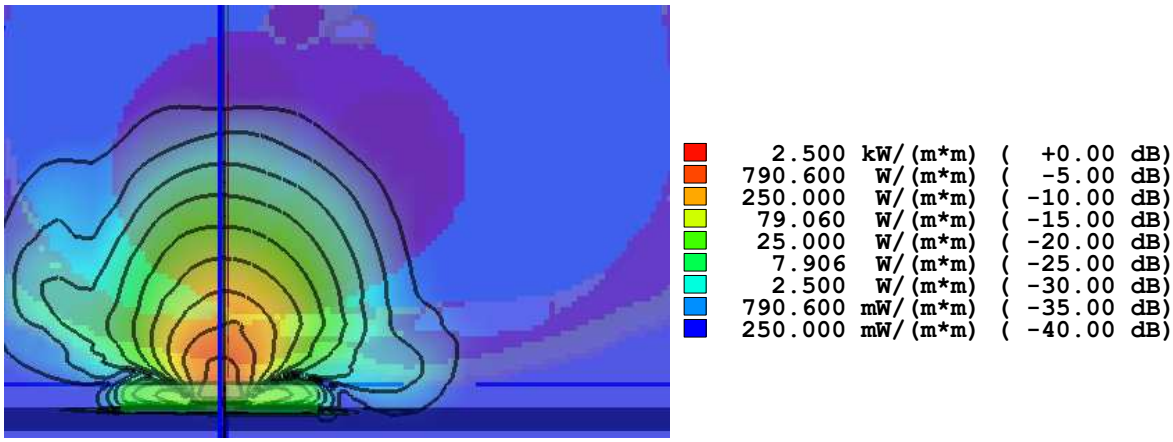

(a)

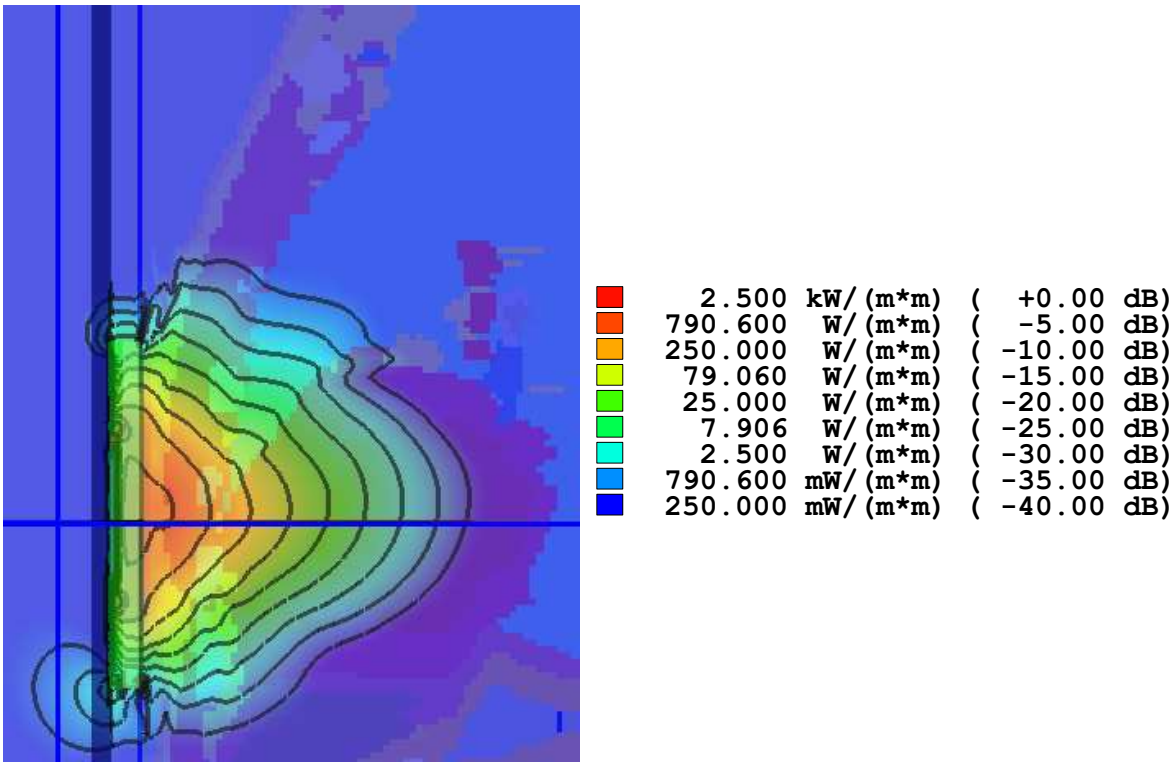

(b)

Figure 5.26: Poynting vector z-component intensity in yz-plane (a) and xz-plane (b)

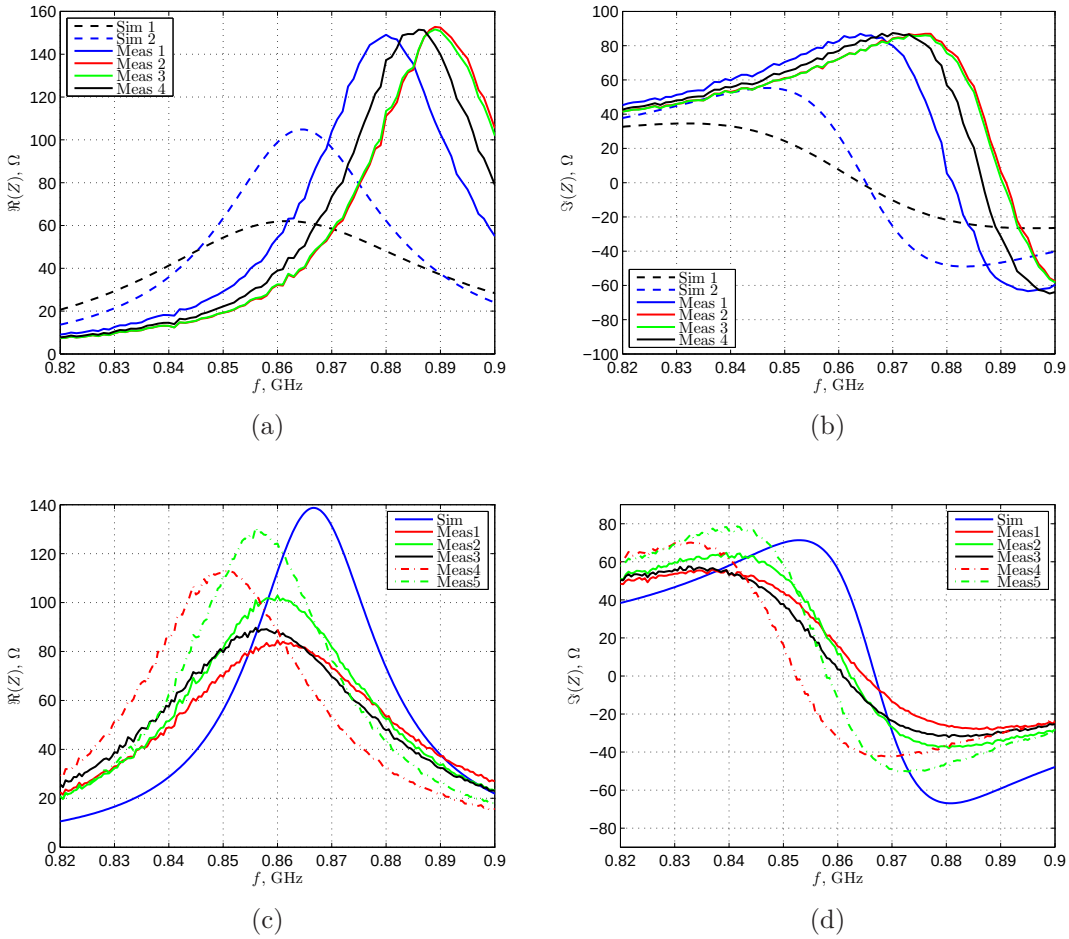

Figure 5.27: Comparison of the antenna impedance obtained from simulation and measurement. (a-b) homogeneous phantom and (c-d) human torso

6 Adaptive Impedance Matching Network

In section 5.2.7 it can be seen that the input impedance of the antenna is sensitive to positioning and varies for different individuals. For that reason an adaptive matching circuit is used in order to reduce the antenna mismatch (see Figure 6.1). Such a system consists of a controllable matching circuit, mismatch measurement circuit and control circuit (analog or digital). In this chapter the individual blocks are investigated and a completed network is experimentally characterized.

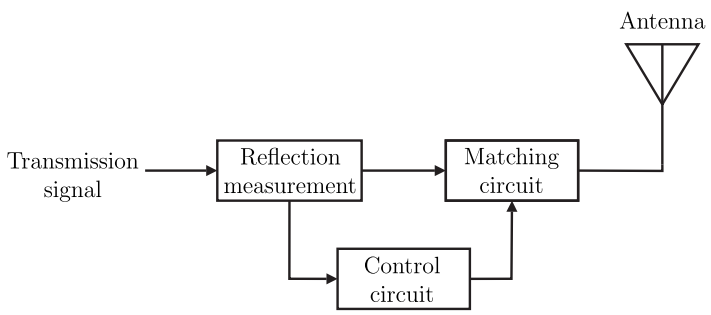

Figure 6.1: Block diagram of adaptive matching network

6.1 Tunable Impedance Matching Network

A vast variety of matching networks can be used to match the complex impedance of a load to the system impedance. In general, one can distinguish between distributed, lumped and a synthesis of distributed and lumped matching networks. Furthermore different topologies (Π-, T- or L-networks) covering different impedance matching domains are well known. There is also a great number of tuning devices, such as varactors or banks of capacitors and inductors.
The goal is the coverage of a large region of the Smith Chart by the matching network in order to improve the matching of a large range of impedances. Theoretically the Π-network enables complete Smith Chart coverage assuming ideal components with an unbounded value range. Due to the parasitic influences and component properties, the coverage is limited, i.e., only load impedance within a limited matching domain can be matched perfectly.

A Π-network with varactor diodes as tuning devices was chosen as the tunable matching network (see Figure 6.2). In a first step the matching domain was determined by

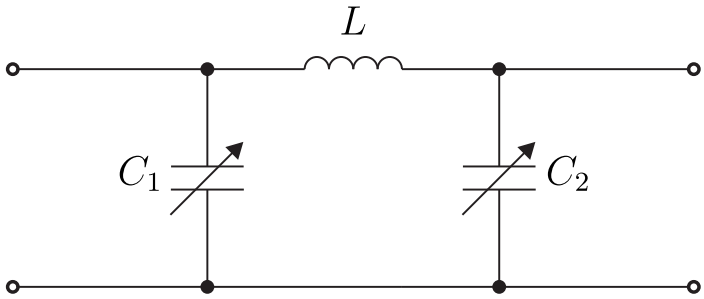

Figure 6.2: Π-network

means of a circuit simulator assuming ideal components with finite component tuning range. Figure 6.3 shows the possible matching domain for an inductor with $L = 2$ nH and variable capacitors with a tuning range $C = 1 - 100$ pF. Conventional variable

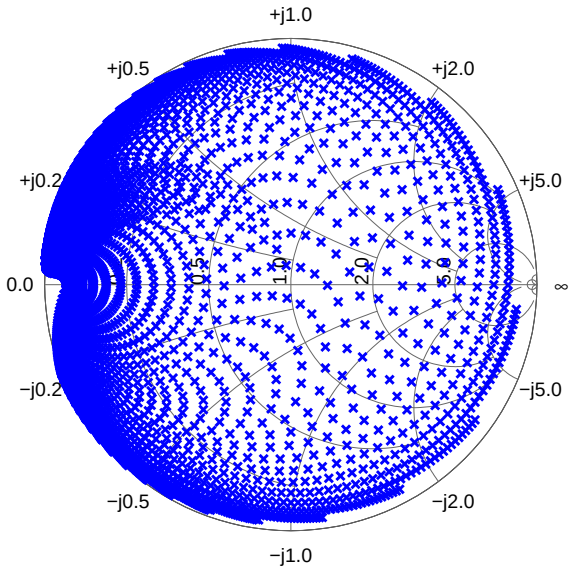

Figure 6.3: Simulated matching domain, ideal components

capacitance diodes have a limited and nonlinear voltage dependent tuning range. A further limiting factor of the capacitance values is the restricted tuning voltage range. Such that a reasonable capacitance value range is e.g. $C = 8 - 20$ pF for Infineon BB545 or $C = 2 - 7$ pF for Infineon BBY51 (voltage range: 0-5 V). In Figure 6.4 the matching domain for $L = 4.7$ nH and the varactor diode BB545 is illustrated. As can be seen the load impedances that can be perfectly matched are limited to a considerably smaller area of the Smith Chart. However this does not mean that the matching of impedances situated outside this area cannot be improved. The matching domain additionally reduces if losses are taken into account.

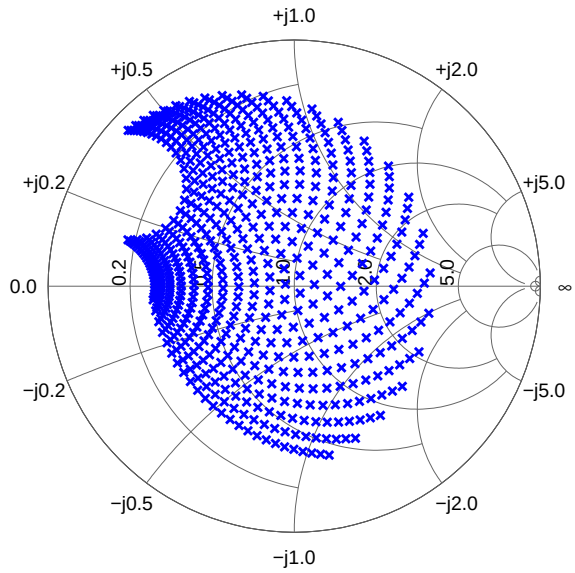

Figure 6.4: Simulated matching domain, $L = 4.7$ nH and varactor diode BB545

The complete matching network with DC-coupling capacitors and tuning voltage supply circuit is depicted in Figure 6.5.

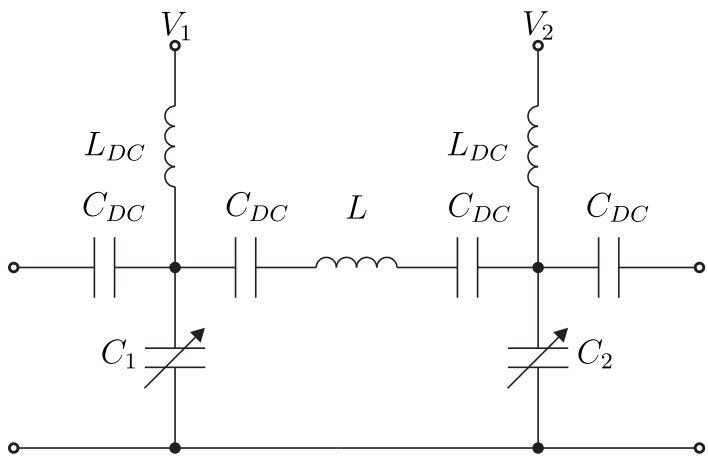

Figure 6.5: Complete Π-network

A discrepancy between first measurements and the simulation was observed. It was tried to improve the accuracy of the simulation model by taking parasitic elements and transmission lines in between the components into account. However still a big discrepancy persisted. A possible reason for this discrepancy may result from inaccurate modelling of the used components. Especially the modelling of the variable capacitance diode is challenging due to fact that not only the capacitance is a function of the applied voltage, but also the parasitic series resistance. Consequently by trying different inductor values in combination with different varactor diodes an acceptable

solution was found. In Figure 6.6, the matching domain for an inductor $L = 3$ nH and varactor diodes (BBY51) with a capacitance range $C = 3 - 7$ pF (bias: $0 - 5$ V) is shown. At this point it becomes clear that a direct calculation method for the

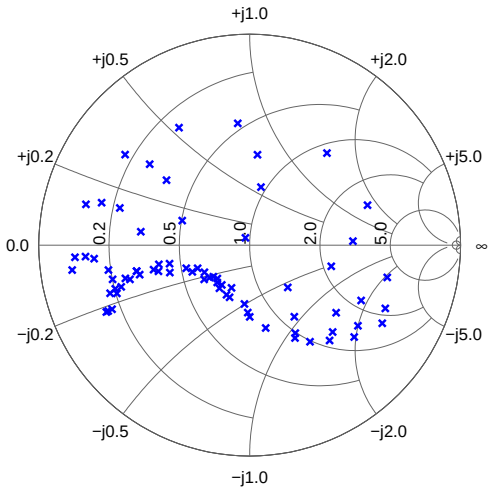

Figure 6.6: Measured matching domain

control of the matching network is not applicable without further improvement of the accuracy of the circuit model. In a first approach the direct calculation method was tried, but failed due to the mentioned reasons. That is why it was decided in a second approach to use an optimization method, as will be described in a later section.

6.2 Reflection Measurement Circuit

In order to determine the reflection coefficient or the voltage standing wave ratio it is necessary to measure separately the incident and reflected wave. For this purpose a directional device (directional coupler) and power detectors can be utilized.

6.2.1 Directional Coupler for Reflection Coefficient / VSWR Measurement

A directional coupler is a 4-port network that samples the signal on the through line, in such a way that discrimination between forward and reflected wave is achieved. The following convention for the ports is used: port 1 is the input port, port 2 is the through port, port 3 is the coupled port and port 4 is the isolated port. The device under test is connected to port 2, the detectors are connected to port 3 and 4. In order to achieve a good separation of forward and reflected wave high isolation is desired.

The quantity that defines the coupler's ability to isolate forward and backward waves is called directivity D and is defined as:

$$D = S_{31,\mathrm{dB}} + S_{21,\mathrm{dB}} - S_{32,\mathrm{dB}}, \tag{6.2.1}$$

where $S_{31,\mathrm{dB}}$ is the coupling C, $S_{21,\mathrm{dB}}$ is the insertion loss IL and $S_{32,\mathrm{dB}}$ is the isolation I. It is crucial to choose a high quality (high directivity) coupler for reflection coefficient measurements in order to minimize errors. For non-ideal couplers the measurement of forward and reverse power is error-prone. However it can be shown that forward power measurements are less sensitive than reverse power measurements to directivity [38].

6.2.1.1 Uncertainty in Reflection Measurement

Beside noise, which is not considered here, the dominant sources of error in a reflection measurement system are directivity, test port match and load match [39]. These error sources are present in both scalar and vector systems. Additional error sources are reflection of the detectors and the finite bits of analog-to-digital converter [40].

Forward Power Measurement Errors: The power detected at the coupled port, in forward power measurements, is the superposition of the desired forward coupled wave and the undesired reverse reflected wave coming from the DUT (assuming that the load in not matched). The resultant wave is the vector addition of the wave voltages and therefore has a variable impact on the measured power depending on the phase shift between both waves. The upper and lower bound power error for a forward measurement can be given as [38]:

$$P_{\mathrm{F,e}} = 10 \cdot \log\left(10^{\frac{-IL-RL-D}{10}} + 1 \pm 2 \cdot 10^{\frac{-IL-RL-D}{20}}\right), \tag{6.2.2}$$

where RL is the return loss at the impedance discontinuity. Figure 6.7 depicts the upper and lower bound measurement error for a coupler with a 1 dB insertion loss for various return losses. It can be seen that a significant error is caused when a device with a low directivity is used. Depending on the phase difference of the forward and reflected wave, the measured power can fall anywhere within a large range. The error is larger for smaller return losses due to a stronger reverse reflected wave. Utilizing a device with a directivity of 15 dB or better reduces the forward power measurement errors below 1 dB [38].

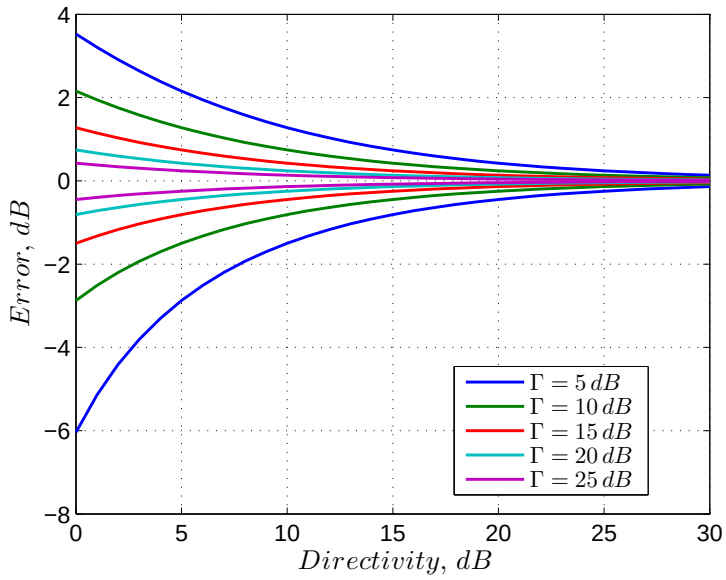

Figure 6.7: Forward power measurement error

Reflected Power Measurement Errors: Reflected power measurements are in contrast to forward power measurements more challenging, since the reflected power is much lower than the forward power. Consequently in order to achieve the same certainty of measurement as in forward power measurements a higher directivity is required. In [38] the maximum and minimum reflected power measurement errors are given by:

$$P_{\mathrm{R,e}} = RL + IL + 10 \cdot \log\left(10^{\frac{-IL-RL}{10}} + 10^{\frac{-D}{10}} \pm 2 \cdot 10^{\frac{-IL-RL-D}{20}}\right), \tag{6.2.3}$$

Figure 6.8 illustrates the measurement error as a function of directivity for different return losses. It is evident that reverse power measurements are more sensitive to the couplers directivity than forward power measurements. In the case that the directivity minus insertion loss is equal to the return loss, the leaked forward wave and coupled reflected wave are equal in magnitude and may superimpose destructively, resulting in an infinite error (worst case scenario). In order to reduce the measurement error to the order of 1 dB a directivity of 15 dB better than the return loss of the DUT is needed. It is concluded [38] that a directivity of 30 dB or better is required to accurately measure the reflected power from a load with a return loss of 15 dB, which is significantly higher than the typical directivity (15-20 dB) of most couplers.

Return Loss Measurement Errors: Measurements of return loss are based on forward and reflected power measurements, consequently erroneous measurements of forward and reflected power result in an error in the return loss measurement. Assuming

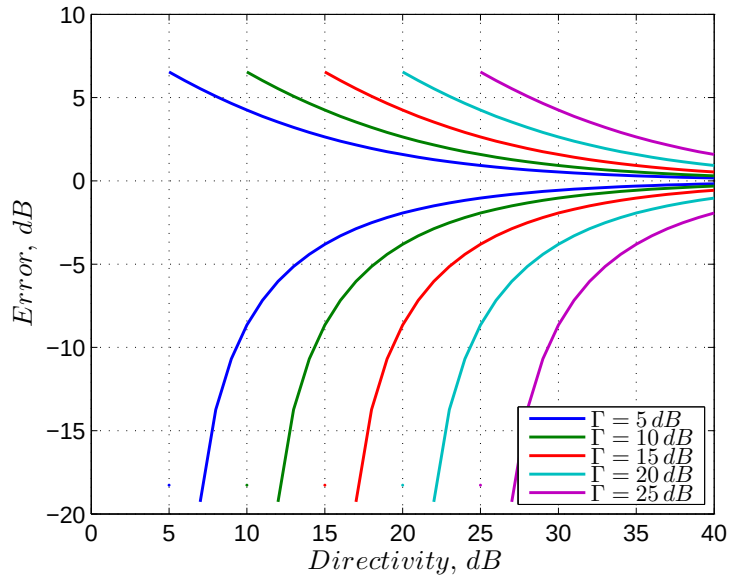

Figure 6.8: Reflected power measurement error

a device with the same directivity for forward and return coupled ports, the return loss can be given as [38]:

$$
\begin{aligned}
RL_{\mathrm{e}} &= P_{\mathrm{F,e}} - IL - P_{\mathrm{R,e}} && (6.2.4)\\
&= RL + IL + 10 \cdot \log\left(10^{\frac{-IL-RL}{10}} + 10^{\frac{-D}{10}} \pm 2 \cdot 10^{\frac{-IL-RL-D}{20}}\right) \\
&\quad -10 \cdot \log\left(10^{\frac{-IL-RL-D}{10}} + 1 \pm 2 \cdot 10^{\frac{-IL-RL-D}{20}}\right). && (6.2.5)
\end{aligned}
$$

The return loss measurement error versus return loss for various directivities is shown in Figure 6.9. Except for very high values of return loss, the return loss measurement error is dominated by the error of the reflected power measurement. As mentioned before, accurate measurement require a device with a directivity of at least 15 dB better, than the return loss of the device under test.

Effect of Output Impedance Mismatch: It should be pointed out that a return loss measurement only detects the reflection caused by the load, not whether the load is matched to the system impedance (50 Ω in RF systems). The measurement actually only indicates whether the load is matched to the output impedance of the directional device, which differs in the non-ideal case from the system impedance. In the case that, based on this measurement a matching circuit is tuned in order to improve matching of a device under test, the device under test would be matched to an impedance not equal to the system impedance.

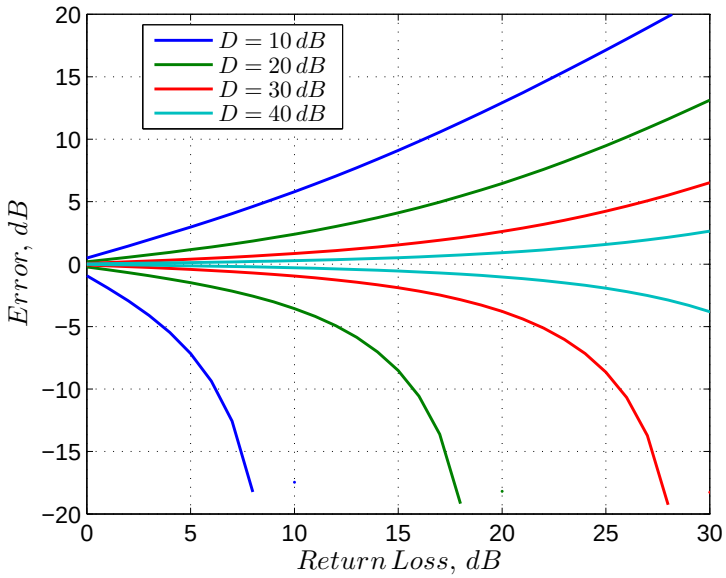

Figure 6.9: Return loss measurement error

Reflections caused by Detectors Reflections of detectors, connected to the coupled and isolated port, are too high to be neglected. The reflected waves will flow to the opposite port, attenuated only by the insertion loss and cause an additional error. In order to separate the detectors two directional devices in series can be used. This approach prevents that the detectors are connected directly.

In our application the goal is to obtain an antenna return loss of 20 dB or better. This necessitates a coupler with a directivity of at least 35 dB for reliable uncorrected return loss measurements. This is hard to achieve and therefore it was decided to use a calibration method to improve the measurement accuracy of the system. A common calibration procedure for one port networks is the OSL (Open, Short, Load) calibration. By means of this calibration approach the errors caused by the system directivity, frequency response and port match are reduced. Typically the improvement in accuracy is better than 20 dB [41]. The effective directivity after calibration equals essentially the return loss of the load used for calibration [39].
As mentioned before a calibration requires measuring the complex reflection coefficient of three different known loads in order to determine the error terms of the measurement system by solving a system of three linear equations. This demands that the circuitry used for reflection measurement can determine the magnitude and phase of the reflection coefficient. The concept of the utilized measurement circuit is presented in the next section.

6.2.2 Reflection Measurement Circuit

Figure 6.10 shows the block diagram of the measurement system. The arrangement consists of a dual directional coupler that samples the incident and reflected signals. Two attenuators are used to adjust the signal levels in both paths. In the path of the incident wave a 3 dB Hybrid is used for the creation of an inphase and quadrature signal. The reflected wave is split by a power divider. The gain & phase detector AD8302 is utilized for the measurement of the magnitude and phase of the reflection coefficient.

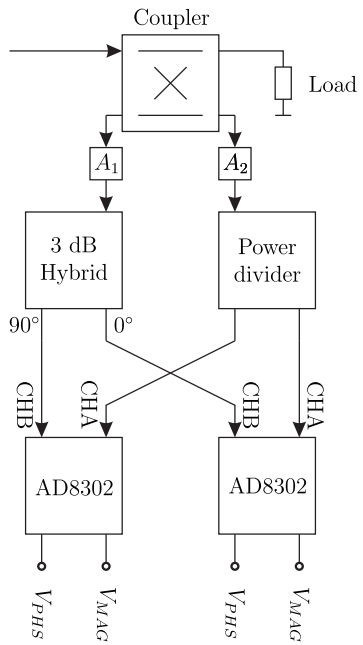

Figure 6.10: Reflection measurement concept

6.2.2.1 Gain & Phase Detector

The AD8302 has a dynamic input range from -60 dBm to 0 dBm and operates from supply voltages of 2.7-5.5 V. Figure 6.11 shows an approximation of the transfer function for the magnitude ratio and phase between the two signals at inputs CHA and CHB. The magnitude output is scaled to 30 mV/dB and the phase output is scaled to 10 mV/Degree. The magnitude error is smallest when the magnitudes of the input signals are both -30 dBm and stays below ±0.5 dB for magnitude ratios of ±25 dB (+25°C). This error originates from the fact that the transfer function becomes nonlinear at the lower and upper bound of the dynamic range. The phase accuracy is reduced for phase differences around −180°, 0° and 180°, here also the phase transfer function exhibits strong non-linearity where the error becomes ±6°. A major limitation of the considered gain & phase detector is the ambiguity of phase difference. It cannot be distinguished whether the phase difference is positive or negative without a priori

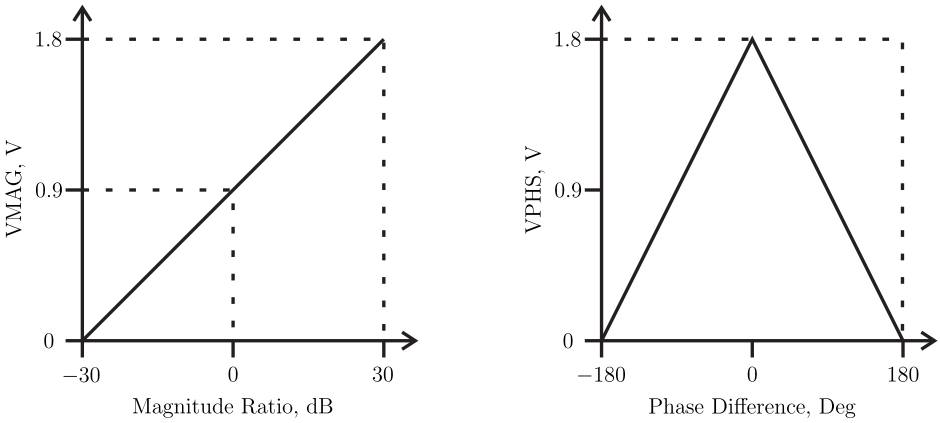

Figure 6.11: Transfer function approximation for magnitude ratio (left) and phase (right)

knowledge which signal leads or lags the other in phase. This issue can be resolved by using a second gain & phase detector, a power divider and a hybrid coupler in order to generate a 90° phase shifted signal. Figure 6.12 shows the relationship between the phase output voltage and the phase difference for reference (blue) and phase shifted input signals (red and green). The second phase difference information will be used only for the determination of the sign of the reference signal.

6.2.2.2 Power Budget

Consider a power of the incident signal of 10 dBm, a nominal reference return loss of 20 dB and a 10 dB dual directional coupler. In order to provide a power $P_{\mathrm{OPT}} = -30$ dBm at the input of channel A and B, a 27 dB and a 7 dB attenuator is required in the channel A and channel B path, respectively (see Figure 6.13). For this setup a voltage $V_{\mathrm{MAG}} = 900$ mV is measured when the return loss of the load is 20 dB. Figure 6.14 illustrates the voltage V_{MAG} versus magnitude ratio and the associated load reflection coefficient and power levels at channel B. This setup allows measurement of return loss from 0 dB to -50 dB, with a reduced accuracy at the lower limit.

6.3 Control Unit

The control unit is based on an Arduino board and an 8 bit digital to analog converter (MAX5115). Output signals of the measurement system are read and processed by the Arduino. Three 10 bit analog-to-digital converters are used to measure V_{MAG} and V_{PHS} (reference and phase shifted signal). A 2-wire serial (I^2C) interface in used for communication with the DAC.

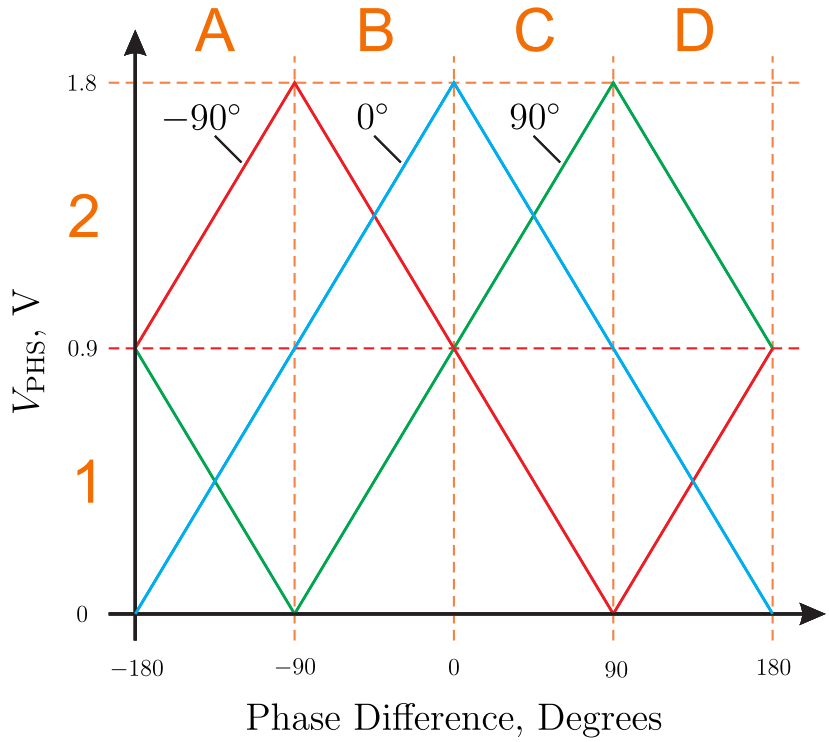

Figure 6.12: Phase detector output voltage vs. phase difference

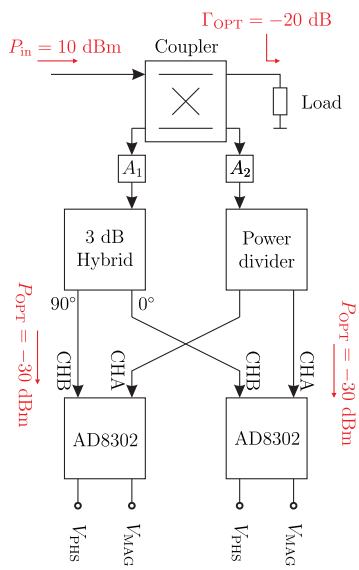

Figure 6.13: Power Budget

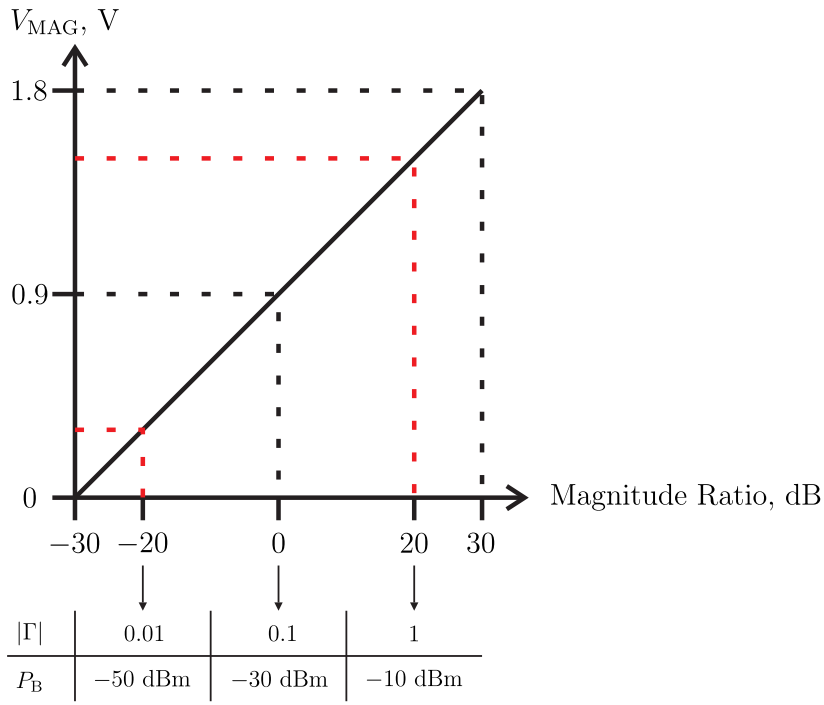

Figure 6.14: V_{MAG} versus magnitude ratio

6.3.1 One-Port Calibration

A one-port calibration of the reflection measurement system is done by three known standards. The standards are measured to determine the three error terms of the measurement system, namely the system directivity error e_{00}, system frequency response error term $e_{10}e_{01}$ and port match error term e_{11} [41]. The measured reflection coefficient Γ_{M} is related the the actual reflection coefficient Γ_{A} by the three error terms:

$$\Gamma_{\mathrm{M}} = e_{00} + \frac{e_{10}e_{01}\Gamma_{\mathrm{A}}}{1 - e_{11}\Gamma_{\mathrm{A}}}. \tag{6.3.1}$$

Solving for Γ_{A} we obtain:

$$\Gamma_{\mathrm{A}} = \frac{\Gamma_{\mathrm{M}} - e_{00}}{e_{11}(\Gamma_{\mathrm{M}} - e_{00}) + e_{10}e_{01}}. \tag{6.3.2}$$

By measuring the three known standards, three linear equations are obtained and a solution for the three error terms can be found. The determination of the error terms is done by MATLAB, it offers a function that solves linear systems.

For calibration and measurements the relationship between magnitude ratio and magnitude output voltage (V_{MAG}) and phase difference and phase output voltage (V_{PHS}) are approximated by a polynomial (see Figure 6.15). The relation of phase difference

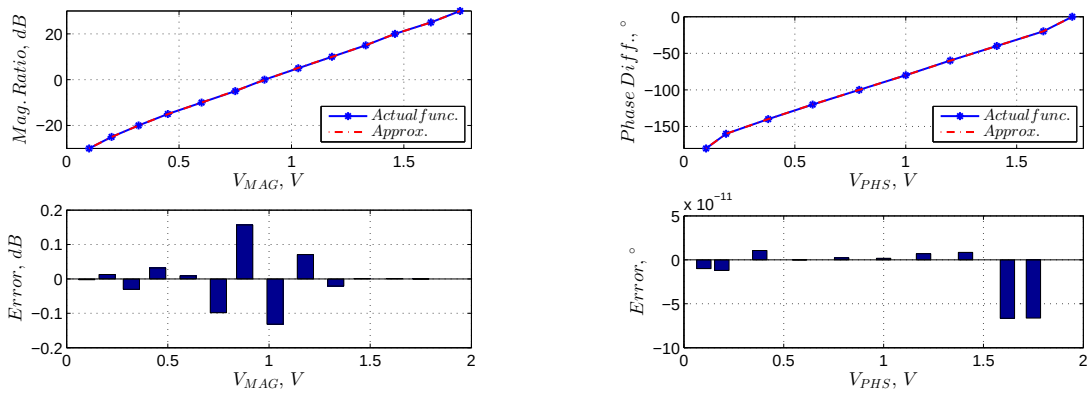

Figure 6.15: Magnitude ratio and phase difference vs. output voltage approximation

and V_{PHS} is approximated only for phase differences from $-180°$ to $0°$, due to symmetry reasons. The approximation error is shown in the lower part of the Figure 6.15. A comparison of measurements done with vector network analyzer and reflectometer of several loads is shown in Figure 6.16. The maximum absolute error for the measured

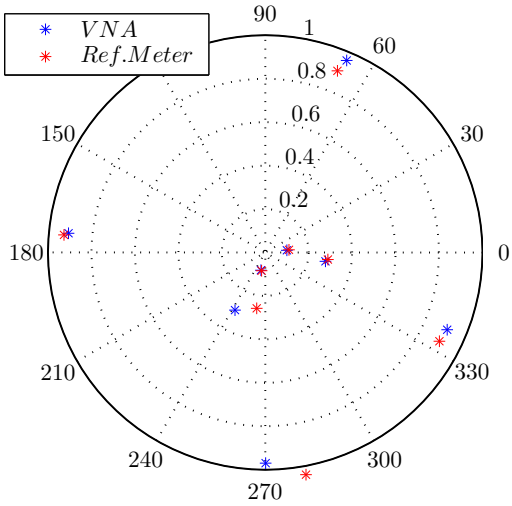

Figure 6.16: Comparison of VNA and reflectometer measurements

loads is 0.07 dB and 19° for the magnitude ratio and phase difference, respectively.

6.3.2 Optimization Method

In order to improve the matching of the antenna an optimization method is required that is based on the sequential examination of trial solutions. A good candidate is the

pattern search method of Hooke and Jeeves. It is a subset of the direct search algorithm and does not require any information about the gradient of the objective function. The pattern search is based on a sequence of exploratory moves about a base point followed by pattern moves. In simple terms, the objective of the exploratory move is to find the best point in the vicinity of the current point. If successful, then a move into the direction of the best point is performed, else the size of the exploratory move is reduced and a new exploration is done. The procedure terminates when a maximum number of iterations, minimum step-size or minimum change of function value is reached.
The numerical computing environment MATLAB, developed by MathWorks, offers an implementation of the pattern search algorithm. It allows the definition of he mentioned convergence criteria, such that it can be adapted to the problem. The objective function has to be defined in a separate MATLAB file. It takes the input variables and returns the function value. In our case there is no objective function that can be defined due to lack of knowledge. Instead of a function definition, the function values are obtained from measurements.

6.4 Experimental System Evaluation

In a final step the adaptive matching system, containing all described components, is tested. Known loads are connected to the matching network, the matching procedure is executed and subsequently the reflection coefficient is measured by the reflectometer. The magnitude of the reflection coefficient with and without adaptive matching system is compared in order to assess the amount of improvement. Due to the fact that the matching domain does not cover the smith chart uniformly the improvement dependents on the phase of the reflection coefficient at the load. Table 6.1 shows the results for several loads. As can be seen the matching of all measured loads was im-

#	Γ (before)	Γ (after)
1	$0.26\angle-98.7°$	$0.003\angle 97.2°$
2	$0.29\angle-6.5°$	$0.014\angle-154.3°$
3	$0.9\angle 68.3°$	$0.1\angle-152.8°$
4	$0.9\angle-27°$	$0.1\angle-118.81°$
5	$0.93\angle 175°$	$0.043\angle-176.8°$
6	$1.04\angle-79.6°$	$0.56\angle-123.5°$

Table 6.1: Reflection coefficient before and after adaptive matching

proved. Even for high reflection coefficients (load 3, 4 and 5) the mismatch could be reduced significantly. Only for load 6 the improvement is minor, which results from the fact that the region of the smith chart where this load is situated is not covered by the matching circuit (see Figure 6.6).

7 Reflectometer Circuit

In chapter 2 the measurement principle and the obtained signal is discussed. It is shown that the measured signal contains several frequency components corresponding to different physical effects. At this point it is distinguished between wanted and unwanted signal components. Wanted-signal components are those which can be related to the heart state. These components are situated in the frequency range above 1 Hz. As unwanted-signal components the static signal (0 Hz) and the signal resulting from respiration (0.2-0.4 Hz) are categorized. It is desired to cancel the unwanted-signal components by means of a filter. Due to the fact that the signal resulting from heart activity is composed of a fundamental signal and several harmonics a filter transfer function may introduce distortions of the original waveform, such that besides an appropriate filtering of the signal the degree of distortion has to be taken into account.

7.1 Cancellation Techniques

The purpose of this section is to give a short overview over existing cancellation techniques and to point out the pros and cons of each method. In general, a cancellation circuit is supposed to suppress unwanted-signals and to pass a wanted-signal band. In this case the canceller acts as a high-pass filter. Thus approaches known from the field of DC offset cancellation can be used. In [42] and [43] widely used cancellation circuits are described and analyzed. In Figure 7.1, 7.2 and 7.3 the main cancellation techniques are depicted, namely the AC coupling, feed-forward and backward cancellation.
The AC coupling method consists of a high-pass filter and an amplifier. This method

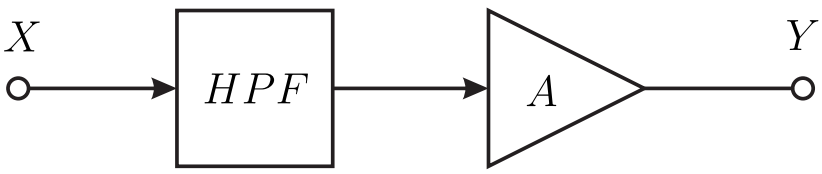

Figure 7.1: AC coupling cancellation technique

is simple and effective but also attenuates the signal band of interest which may cause the loss of information and therefore is suitable for scenarios where the band of interest is far away from DC [42]. The transfer function of the AC coupling canceller is given by:

$$H_{\mathrm{AC}}(s) = A \cdot H_{\mathrm{HPF}}(s). \tag{7.1.1}$$

In the feed-forward scheme the input signal is split and manipulated in two parallel branches. One branch contains an amplifier with gain A which amplifies the input

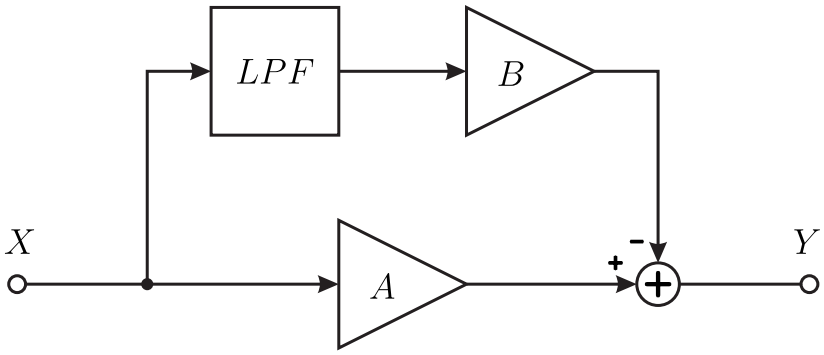

Figure 7.2: Feed-forward cancellation technique

signal. In the other branch the input signal is low-pass filtered and subsequently amplified. The filter attenuates the wanted-signal and passes the unwanted-signal. The output of this branch is subtracted from the output of the amplifying branch. If amplification $A = B$, the output signal contains only the signal of interest. This method is simple but works satisfactory when the gains of both branches are equal [42]. The transfer function is as follows:

$$H_{\mathrm{FF}}(s) = A - B \cdot H_{\mathrm{LPF}}(s). \tag{7.1.2}$$

As can be seen in Figure 7.3 the feedback cancellation technique is based on the feedback of a filtered and amplified version of the output signal. The unwanted frequency

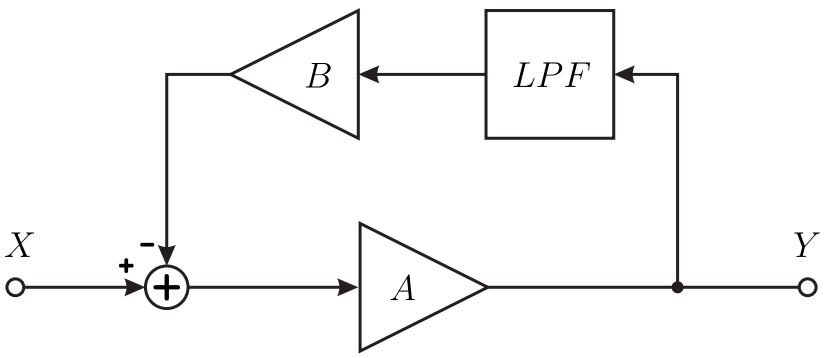

Figure 7.3: Feedback cancellation technique

band passes the low-pass filter and is amplified by the gain B. The resulting feedback signal is subtracted from the input signal such that only the wanted frequency band is preserved. For sufficiently high amplification B the closed loop gain of the unwanted-signal is about $1/B$ [42]. The feedback may cause stability problems so that a proper distribution of the low-pass filter poles and suitable gains A and B are required. Another disadvantage is that the cutoff frequency of the closed loop system

is a function of gain A and B [43]. Higher gain leads to higher cutoff frequency and therefore a lower cutoff frequency of the loss-pass filter is needed for a sufficiently high suppression of the unwanted frequency range. The transfer function of the feedback canceller is as follows:

$$H_{\mathrm{FB}}(s) = \frac{A}{1 + A \cdot B \cdot H_{\mathrm{LPF}}(s)}. \tag{7.1.3}$$

Figure 7.4 compares optimized frequency responses of the discussed cancellers utilizing second-order filters. Optimization variables are the gain of the amplifiers and the cutoff frequency of the utilized filters. The filter type and order is chosen arbitrarily for this comparison, but is equal for the investigated cancellation techniques. The attenuation

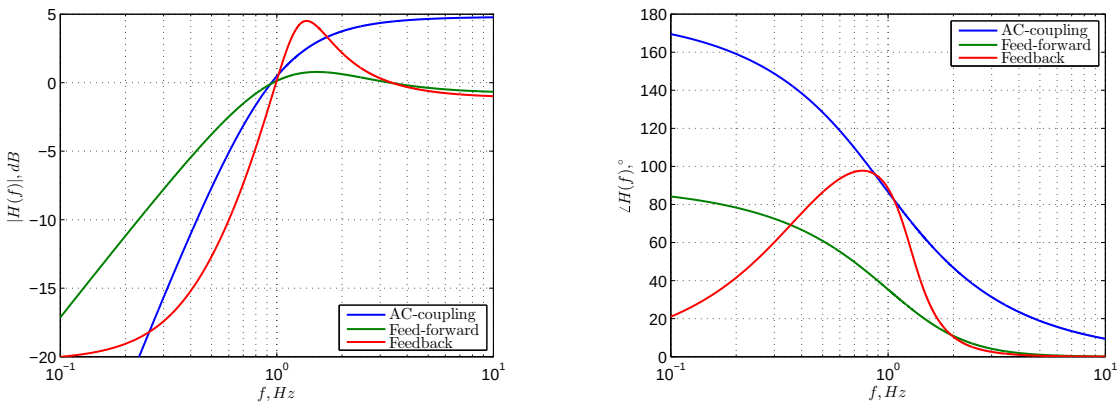

Figure 7.4: Comparison of cancellation techniques

of the AC-coupling canceller of the unwanted frequency range (0-0.4 Hz) is better than -15 dB. The phase response shows a typical response of a second order filter covering 0-180°. In the case of the feed-forward canceller the suppression of the unwanted frequency range is poorer and less step than in the case of the AC-coupling canceller but on the other hand it has a more linear phase response. The frequency response of the feedback canceller shows a sharp roll-off and a better suppression of the unwanted frequency range, compared to the feed-forward canceller. The drawback is a strong non-linear phase response which leads to distortion of the pulse output signal. Phase distortion is a linear type of distortion and therefore reversible. However at this point it is not known whether this type of distortion makes the obtained signal unusable for the target application. The shape of the output signal by now is not assigned to distinct heart states. A correlation of the obtained signal with a reference signal, like ECG or heart sounds is required to evaluate the effect of phase distortion. In the case that it turns out that phase distortion is not disadvantageous higher order filter or filter with steeper roll-off and highly non-linear phase could be utilized.

7.1.1 Digital Cancellation

Figure 7.5 illustrates a digital cancellation technique. The power detector senses the DC signal and feeds it to the digital signal processing (DSP) unit. A correction factor α is computed and fed back to the DAC which produces a voltage in order to compensate the DC signal. This scheme has an inherent drawback, namely the delay of the DSP unit. The calculation of the correction factor α takes time and may result in the lag of the correction voltage behind the time variant DC signal. This may cause over-compensation or under-compensation of the DC signal [42].

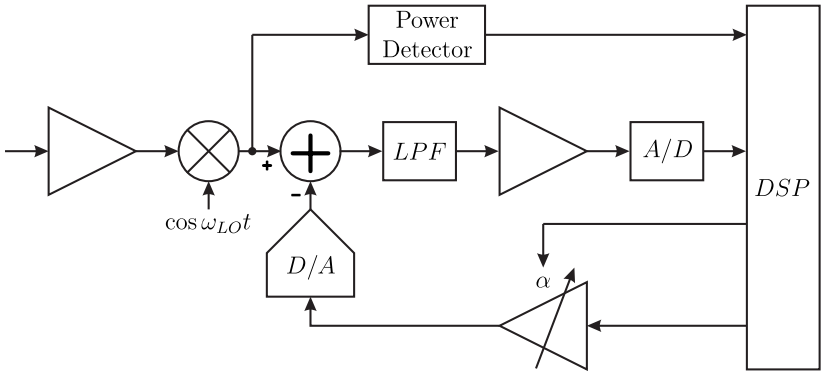

Figure 7.5: Digital cancellation technique [42]

Another approach is digital filtering where the input signal is digitized and manipulated mathematically. In the case of a much higher magnitude of the unwanted-signal relative to the wanted-signal, the ADC input range is constrained to the higher values resulting in a limitation of the ADC resolution for the wanted-signal. For this reason an ADC with high resolution would be required.

7.1.2 Receiver with Reflected Power Canceller

In the same way as mentioned above for the ADC used in digital filtering of the down-converted receive signal, the problem of high dynamic range due to the unwanted-signal components (skin reflection and respiration signal) may degrade ever the down-conversion stage of the receiver. This problem has been solved in CW-radar systems [44] with the introduction of Reflected Power Canceller (RPC). The RPC employs LP-filtering in a Cartesian feed-back loop to attenuate the RF-components of the unwanted reflections at the down-converter input, thus avoiding saturation and maintaining linear operation of the receiver, at the same time, the down-converter output signal exhibits suppression of the unwanted-signal while the wanted-signal above the LP-cutoff remains.
Effectively, the RPC represents the down-converter receiver of a CW-radar including the unwanted-signal filter. The concept was adopted for the receiver of our reflectometer system.

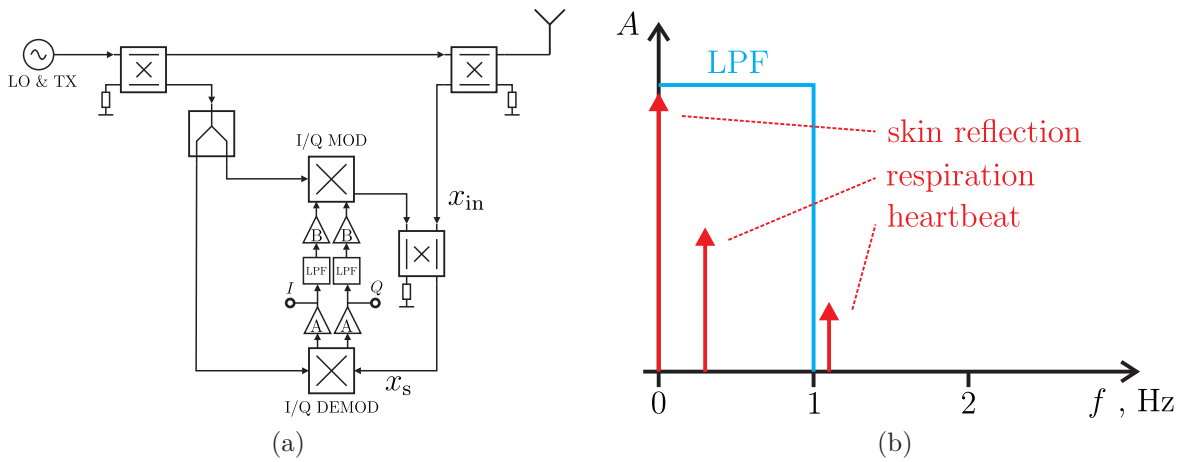

Figure 7.6: Reflectometer circuit with reflected power canceller (a). Reflected signal spectrum (b)

The block diagram of the system is shown in Figure 7.6a together with the configuration of its LP-filter and the respective signals. The signal coming from the antenna enters a control loop, which is supposed to suppress the constant and slowly varying part of the reflected signal. The control loop consists of an I/Q demodulator, an active low-pass filter, amplifiers, an I/Q modulator and a cancellation coupler. After entering the loop the RF signal is converted into an I/Q-signal, which is filtered and amplified (see Figure 7.6b). Subsequently the I/Q-signal is converted into an RF signal and finally superimposed with the signal coming from the antenna. Due to the superposition the constant and slowly varying part of the reflected signal is attenuated. This corresponds to a 180° phase shift caused by the loop.

7.2 Mathematical Model of the Reflected Power Canceller

A low-pass filter is used in order to suppress the wanted-signal and to pass to unwanted-signal components. The general transfer function of a low-pass filter $H(s_\mathrm{n})$ can be written as [45]:

$$H(s_\mathrm{n}) = \frac{H_0}{\prod_i (1 + a_\mathrm{i} \cdot s_\mathrm{n} + b_\mathrm{i} \cdot s_\mathrm{n}^2)}, \tag{7.2.1}$$

with $s_\mathrm{n} = s/\omega_\mathrm{c}$ the normalized complex frequency, $s = \sigma + j\omega$ the complex frequency, ω_c the corner frequency, H_0 the passband gain at DC and a_i and b_i the filter coefficients. The choice of the filter coefficients determines the filter type (Butterworth, Tschebyscheff or Bessel). In Figure 7.7 the block diagram of the closed loop is depicted. The transfer function of the closed loop for the RF-signals is:

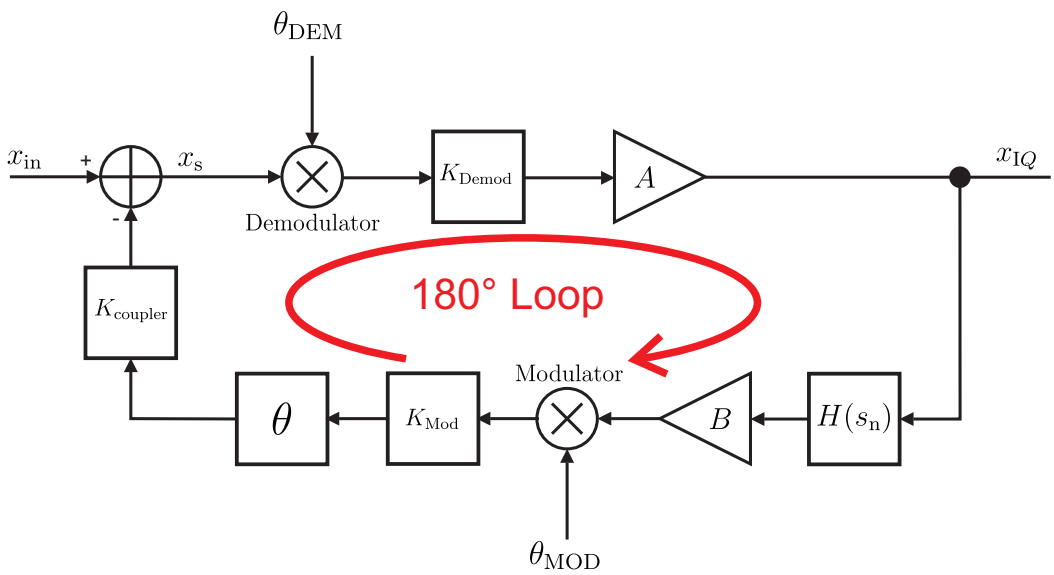

Figure 7.7: Closed loop block diagram

$$H_{\mathrm{Loop}}(s_{\mathrm{n}}) = \frac{x_{\mathrm{s}}}{x_{\mathrm{in}}} = \frac{1}{1 + K \cdot H(s_{\mathrm{n}}) \cdot e^{j\theta} \cdot e^{j(\theta_{\mathrm{MOD}} - \theta_{\mathrm{DEM}})}}, \tag{7.2.2}$$

where K is the open loop gain, θ is the phase offset and θ_{MOD} and θ_{DEM} are the phases of the LO-signal of the modulator and demodulator, respectively. For equal LO-phases ($\theta_{\mathrm{MOD}} = \theta_{\mathrm{DEM}}$) the exponential term in equation 7.2.2 containing these quantities becomes 1. The factor K contains the conversion gain of the modulator and demodulator, the gain A and B and the coupling factor K_{coupler} of the cancellation coupler:

$$K = A \cdot B \cdot K_{\mathrm{Demod}} \cdot K_{\mathrm{Mod}} \cdot K_{\mathrm{coupler}}. \tag{7.2.3}$$

Substituting equation 7.2.1 into 7.2.2, results in:

$$H_{\mathrm{Loop}}(s_{\mathrm{n}}) = \frac{x_{\mathrm{s}}}{x_{\mathrm{in}}} = \frac{\prod_i (1 + a_{\mathrm{i}} \cdot s_{\mathrm{n}} + b_{\mathrm{i}} \cdot s_{\mathrm{n}}^2)}{\prod_i (1 + a_{\mathrm{i}} \cdot s_{\mathrm{n}} + b_{\mathrm{i}} \cdot s_{\mathrm{n}}^2) + K \cdot H_0 \cdot e^{j\theta} \cdot e^{j(\theta_{\mathrm{MOD}} - \theta_{\mathrm{DEM}})}}. \tag{7.2.4}$$

As can be seen the zeros of the obtained transfer function $H_{\mathrm{Loop}}(s_{\mathrm{n}})$ correspond to the poles of the low-pass filter transfer function. The location of the poles of $H_{\mathrm{Loop}}(s_{\mathrm{n}})$ can be changed by altering the factor $K \cdot H_0 \cdot e^{j\theta} \cdot e^{j(\theta_{\mathrm{MOD}} - \theta_{\mathrm{DEM}})}$ for a given LFP function. The down-converted signals I and Q contain the relevant information, thus we are interested in the transfer function related to these quantities:

$$H_{\mathrm{Loop,IQ}}(s_{\mathrm{n}}) = \frac{x_{\mathrm{IQ}}}{\tilde{x}_{\mathrm{in}}} = \frac{A \cdot K_{\mathrm{Demod}} \cdot \prod_i (1 + a_{\mathrm{i}} \cdot s_{\mathrm{n}} + b_{\mathrm{i}} \cdot s_{\mathrm{n}}^2)}{\prod_i (1 + a_{\mathrm{i}} \cdot s_{\mathrm{n}} + b_{\mathrm{i}} \cdot s_{\mathrm{n}}^2) + K \cdot H_0 \cdot e^{j\theta} \cdot e^{j(\theta_{\mathrm{MOD}} - \theta_{\mathrm{DEM}})}}. \tag{7.2.5}$$

where $\tilde{x}_{\text{in}}$ is the down-converted RF signal after the demodulator.

The transfer function of the loop can be adjusted by means of several parameters. These parameters are: the gain A and B, the phase offset θ and parameters related to the utilized filter, like cutoff frequency f_{c}, filter order N and filter type.

The mentioned filter properties affect the signal distortion and time delay which may make the output signal useless. Time delay has to be taken into account due to the fact that the measurement is supposed to be in real-time. Signal distortion can change the signal properties such that the relevant information is corrupted.

A filter function is needed that passes frequencies from 0 - 0.4 Hz nearly unattenuated and attenuates frequencies above 1 Hz. This would require a very high roll-off which is only realizable with a higher-order filter. Another possibility is to use a filter that attenuates the desired frequency range and also introduces a phase shift between the wanted and unwanted frequency ranges of 180°. Such that the lower frequency range (0 - 0.4 Hz) is superimposed destructively and the higher frequency range (1 - 1.7 Hz) constructively. This approach can cause instabilities in the higher frequency range due to the positive feedback and has to be handled with caution. Additionally this approach requires a sharp phase transition which is also only realizable with a higher-order filter. In order to have a phase shift of 180° in the stop-band a filter of at least second order is needed. Furthermore a high amplification is required for a good suppression of the unwanted-signals due to the fact that we are dealing with a control loop. However a high loop gain in tandem with a non-ideal filter would also enhance the heart signal frequency range and degrade the overall filter function. Consequently it is noticed that the desired function of the cancelling loop is hard to achieve and a sensible tradeoff has to be found.

The further investigation of the loop is done based on a second order Bessel filter. The aim is to show the mentioned dependencies of the closed loop transfer function with respect to the gain A and B, the phase offset θ, cutoff frequency f_{c} and the modulator/demodulator phase imbalance $\Delta\theta = \theta_{\text{MOD}} - \theta_{\text{DEM}}$. For a second order filter the closed loop transfer function can be written as:

$$H_{\text{Loop,IQ}}(s_n) = \frac{x_{\text{IQ}}}{\tilde{x}_{\text{in}}} = \frac{A \cdot K_{\text{Demod}} \cdot (1 + a_1 \cdot s_{\text{n}} + b_1 \cdot s_{\text{n}}^2)}{1 + a_1 \cdot s_{\text{n}} + b_1 \cdot s_{\text{n}}^2 + K \cdot H_0 \cdot e^{j\theta} \cdot e^{j(\theta_{\text{MOD}} - \theta_{\text{DEM}})}}. \tag{7.2.6}$$

System stability is guaranteed when all poles are in the left half plane which corresponds to a negative real part. The stability is affected by the gain A and B, the low-pass filter transfer function and by the phases θ, θ_{MOD} and θ_{DEM}. Figure 7.8 shows the pole zero plot for different gain B and $\theta + (\theta_{\text{MOD}} - \theta_{\text{DEM}}) = 0°$. The system has a pair of complex conjugate poles p_1 and p_2 and a pair of conjugate complex zeros z_1 and z_2. With increasing gain the real part of the conjugate complex poles stays constant and the imaginary part increases. The poles stay in the left half plane such that for this phase condition the system cannot become unstable regardless of how much the

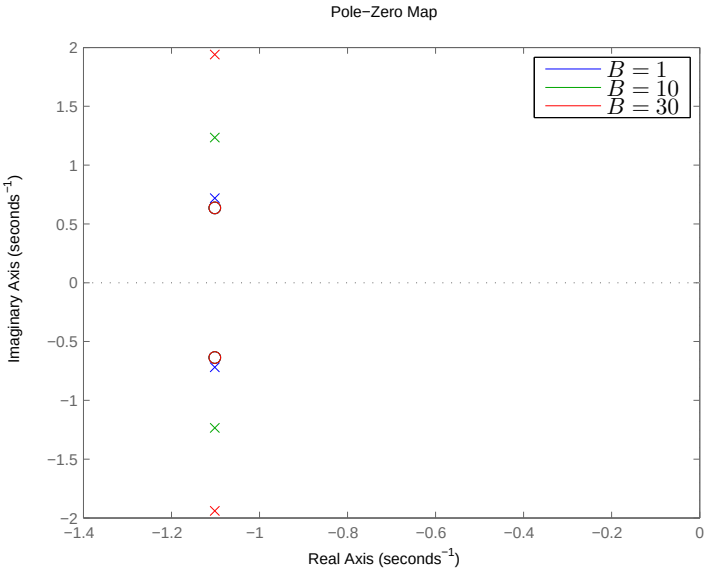

Figure 7.8: Closed loop pole zero plot for different gain B

gain is increased. The gain A has the same effect on the location of the poles as gain B.

The effect of the gain B on the magnitude of the frequency response $H_{\text{Loop}}(f)$ is depicted in Figure 7.9. As previously mentioned a higher gain B leads to a higher suppression of the low-frequency-component and at the same time to an undesired suppression of the frequencies above 1 Hz. This results from the fact that the imaginary part of the poles increases with increasing gain B.

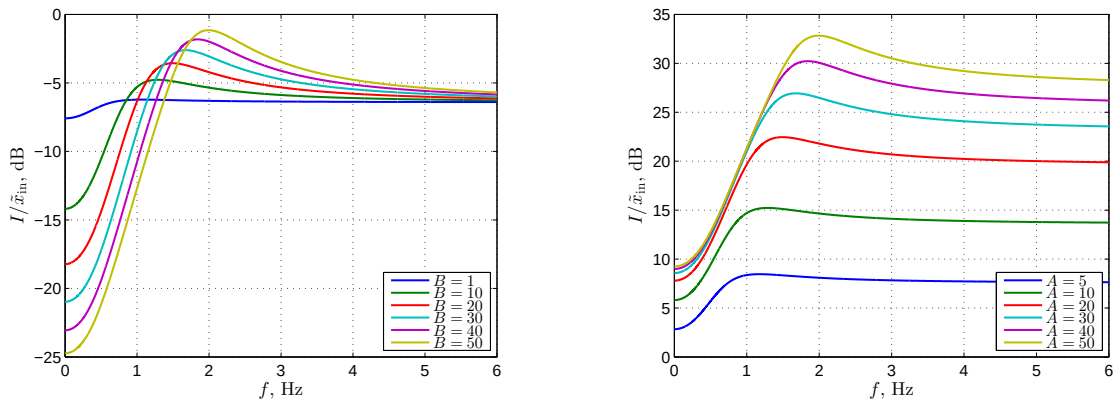

Figure 7.9: Transfer function depending on gain B with $A = 1$ and gain A with $B = 1$, $\theta = 0°$

Figure 7.10 shows the real part of both poles as a function of the phase offset θ for different gain B. The real part of p_1 is negative for all phase and gain conditions (left

Figure). In contrast, the real part of p_2 (right Figure) becomes positive for certain combinations of the phase offset θ and gain B. It can be seen that with increasing gain B the range for the phase offset θ that yields a stable system is reduced. The zero-crossing of the y-axis marks the point where the system becomes unstable.

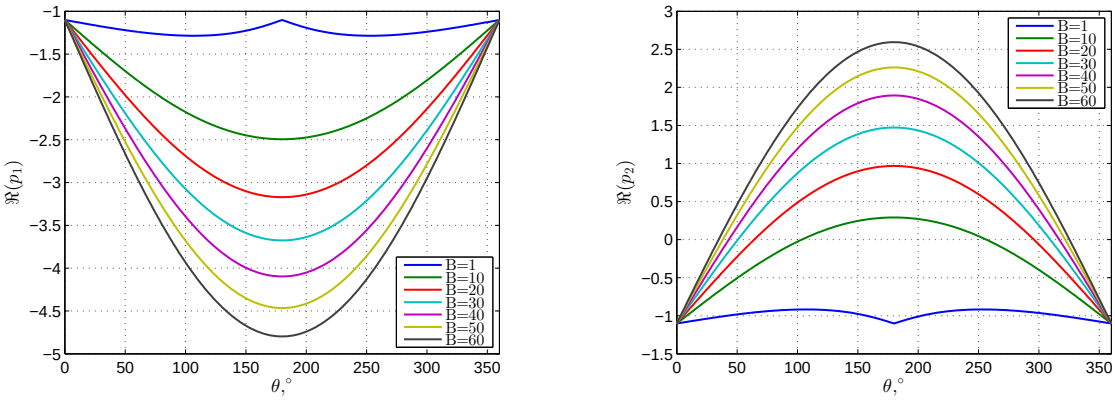

Figure 7.10: Real part of both poles as a function of θ and B

Advanced Design System (ADS) simulation results of the system in time domain for $A = 1$, $B = 30$ and different phase shifts θ are shown in Figure 7.11. The simulated system consists of a simplified model without up and down conversion of the signal. The depicted step responses are in agreement with the mathematical model. As can be seen, the system becomes unstable for phase shifts greater than about 50°. The

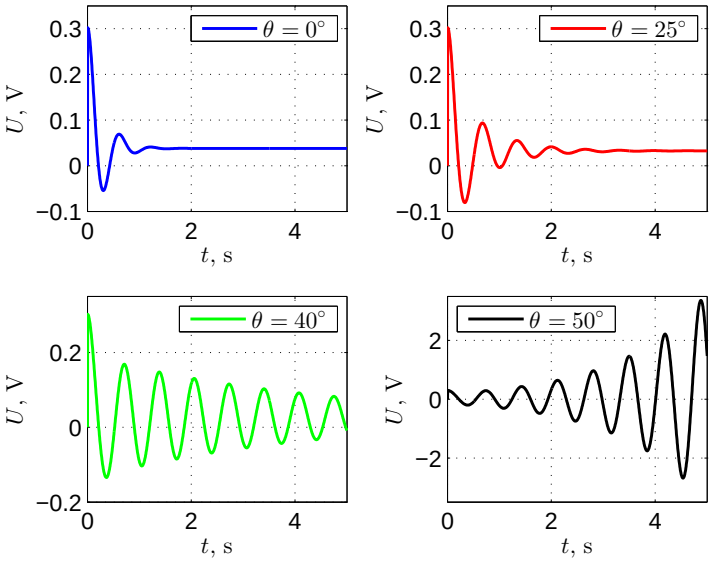

Figure 7.11: ADS simulation results for $A = 1$, $B = 30$ and different phase shifts θ

settling time of the system is 1.5 s and 3.5 s for $\theta = 0°$ and $\theta = 20°$, respectively. Thus

increasing θ results in greater settling time and finally leads to an unstable system. For higher order filters the analysis of the system stability becomes more complicated due to the greater number of poles and the range of θ resulting in a stable system reduces with increasing filter order.

In Figure 7.12 the frequency response dependent on the phase offset θ is shown, for a gain $A = 1$ and $B = 30$. As can be seen, it is possible to adjust the transfer function

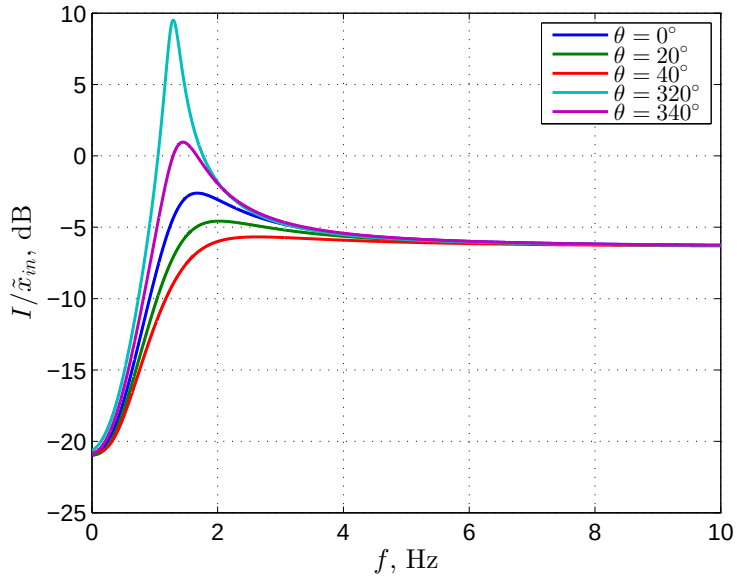

Figure 7.12: Transfer function depending on loop phase θ, $A = 1$ and $B = 30$

by the phase θ. However, certain values of θ lead to an unstable system, such that the range of θ has to be carefully selected. A phase imbalance between the phases of the modulator θ_{MOD} and demodulator θ_{DEM} has a similar effect on the frequency response as the phase offset θ. The phase imbalance can be set to zero by designing the distribution network for the local oscillator signal appropriately. On the other hand, this dependency can also be used to adjust the transfer function of the closed loop.

In Figure 7.13 the frequency response dependent on the cutoff frequency f_{c} of the low-pass filter is depicted. The transition from stop-band to pass-band shifts to lower frequencies with decreasing f_{c}. Additionally the transition is sharper for lower cutoff frequencies. The suppression of the DC-component stays the same but the attenuation of the unwanted low-frequency-components decreases with f_{c}.

It is seen that the transfer function depends on multiple variables, which can be adjusted in order to optimize the transfer function. In the following section the focus is laid on the loop phase offset θ, the cutoff-frequency of the low-pass filter f_{c} and the gain A and B and try to optimize the frequency response in ADS. The optimization is done based on the maximization of the slope of the transfer function in the frequency range from 0.4 - 1 Hz. Simultaneously a small phase variation (small variation in group delay) in the frequency range above 1 Hz is desired in order to minimize signal

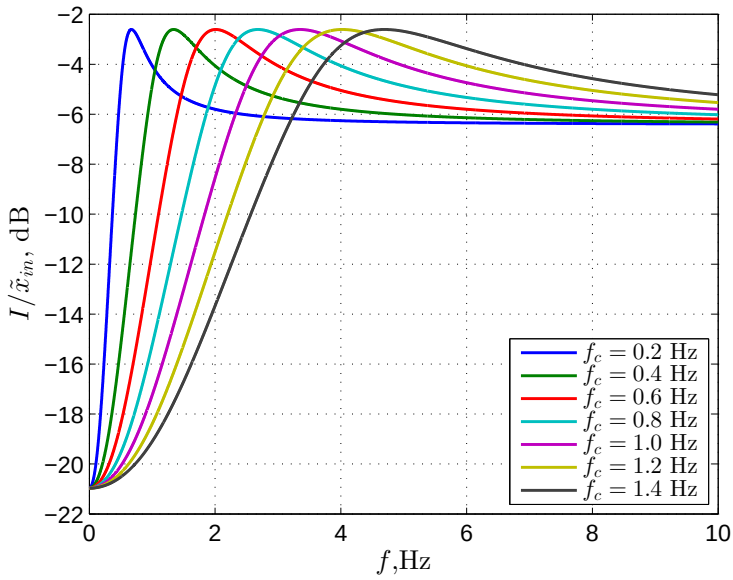

Figure 7.13: Frequency response as a function of LPF cutoff frequency, $A = 1$, $B = 30$ and $\theta = 0°$

distortion. From ADS optimization the results listed in Table 7.1 are obtained. The

	Sol 1	Sol 2
A	1.88	1.81
B	60	34.4
θ	$-11.31°$	$0°$
f_c	0.23 Hz	0.31 Hz

Table 7.1: ADS optimization results

achieved suppression of the unwanted band is below 17.05 dB and 15.59 dB for solution 1 and solution 2, respectively (see Figure 7.1). The passband magnitude is 0-5 dB. Additionally the system has a nonlinear phase response which leads to distortions of the pulse output signal. The resulting step response for solution 1 and 2 is shown on the right hand side of Figure 7.14. In comparison the settling time for solution 1 is more the two times longer than for solution 2.

7.3 Realization and Measurements

There are several factors that can degrade the proper function of the feedback canceller shown in Figure 7.3. These factors are:

- operational amplifier output current saturation,

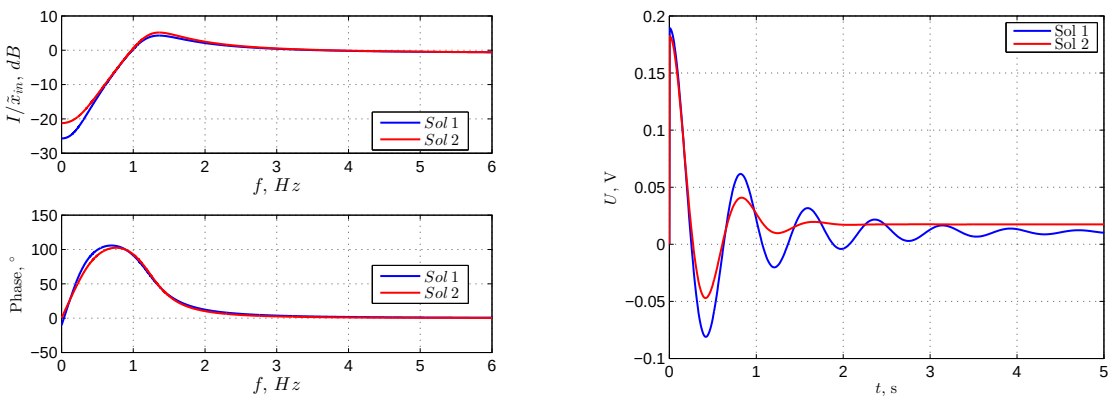

Figure 7.14: Optimized frequency responses and resulting step response

- operational amplifier input offset voltage,
- I/Q demodulator offset,
- I/Q modulator leakage and saturation.

By setting the gain A and B one should consider that a high gain in the DC path can saturate the I/Q modulator. Furthermore the maximum peak output voltage of operational amplifiers is limited and a function of load resistance. The input impedance of the I/Q modulator is around $50\,\Omega$, thus, in order to drive this small resistive load the loop gain must not be set to high. The current saturation of the operational amplifier can be avoided by an extra driver circuit at the output of the amplifier. Another solution for both issues is the distribution of the gain B in the control loop, e.g., by using an additional RF amplifier at the output of the I/Q modulator and reducing the gain in the DC path.
The input offset voltage of operational amplifiers can cause overdrive problems if the signal to be amplified is of the same magnitude as the input offset voltage, because both voltages present at the input are amplified by the same gain. An offset null circuit (see Figure 7.15) can decrease this effect.
The I/Q demodulator outputs exhibit also a DC offset. Without compensation the offset voltage is amplified by the gain A and B and applied to the I/Q modulator input generating an interfering RF signal. Compensation of the DC offset can be done by means of an offset null circuit of the operational amplifiers in the chain.
Another issue is the LO-leakage of the I/Q-modulator which generates an RF-signal even if no I/Q-signals are applied at the inputs, such that the output signal of the modulator is a superposition of the filtered RF-signal and LO-leakage signal. If the filtered RF-signal is of the same magnitude as the LO-leakage then the function of the loop can be degraded. In order to avoid this situation an adequate gain is required. The LO-leakage can also be compensated by applying an LO-leakage compensation technique. One of such techniques is to apply an I/Q DC bias to the input of the modulator.

7.3.1 Filter Circuit

The circuit shown in Figure 7.15 consists of an adjustable amplifier and a second order low-pass filter in Sallen Key topology. Since the modulator and demodulator work optimal if an impedance of $50\,\Omega$ is presented to all inputs and outputs of both devices, a resistor of $R_1 = 50\,\Omega$ parallel to the input and a resistor $R_6 = 50\,\Omega$ in series to the output is added to the circuit. Otherwise the input impedance of the circuit would be very high and the output impedance very low. Offset null circuits are used to compensate the DC offset of the demodulator and the LO-leakage of the modulator. The circuit is designed for a cutoff frequency $f_c = 0.26$ Hz and a gain of 19.2. Its

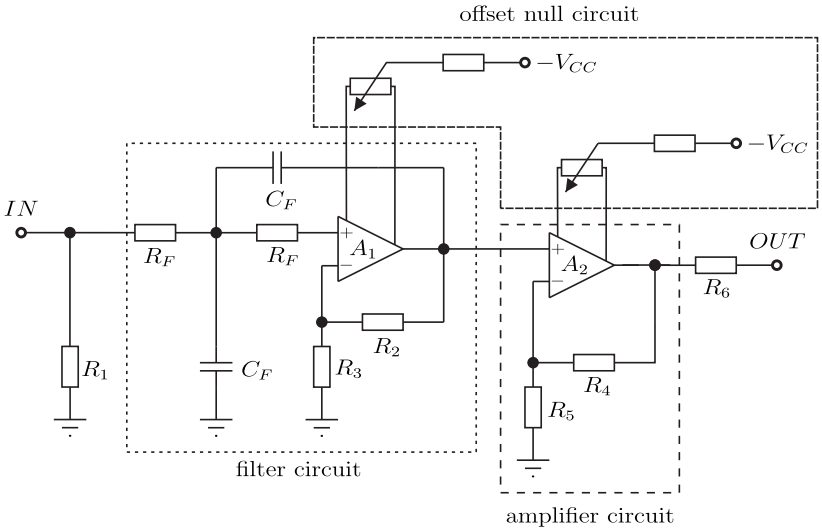

Figure 7.15: Active filter circuit

measured frequency response is depicted in Figure 7.16a.

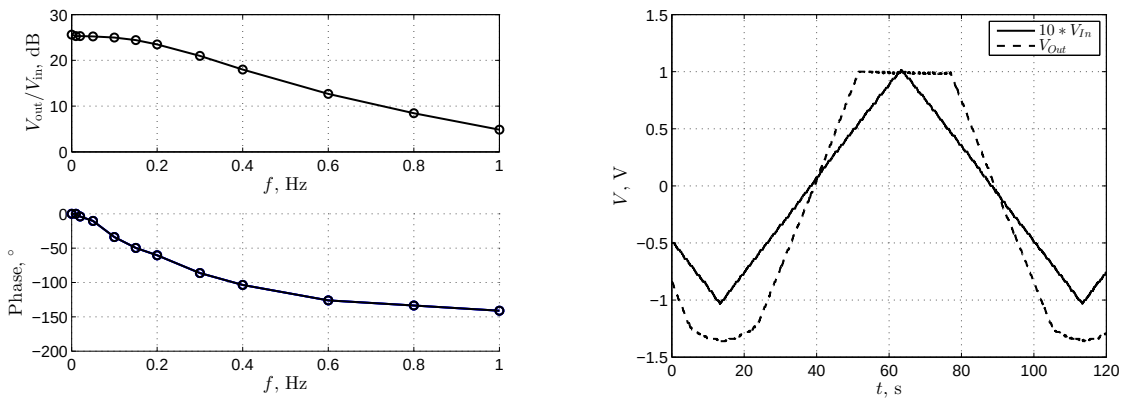

(a) (b)

Figure 7.16: Measured LPF frequency response (a) and current saturation of active filter circuit (b)

Figure 7.16b illustrates the measured input and output voltage versus time for a triangular test circuit. Due to current saturation the output voltage is limited to $V_{\text{out,max+}} \approx 1$ V and $V_{\text{out,max-}} \approx -1.2$ V for positive and negative voltages, respectively. Consequently for a gain of 19.2, the maximum input voltage is limited to ± 50 mV.

7.3.2 Loop Adjustment

In a first step the offset null circuits are used to compensate the I/Q demodulator offset voltage. The I and Q output exhibit an offset of $V_{\text{I,offset}} = 0.700$ mV and $V_{\text{Q,offset}} = -1.86$ mV, respectively. Secondly the LO-leakage is reduced from -26.3 dBm to -52.8 dBm by means of the null circuit of the amplifier circuit. Without this step the adjustment of the loop cannot be done correctly.
The setup shown in Figure 7.17 is used to adjust the loop phase. It is based on measuring the transmission coefficient $\underline{S}_{21}$ of the open loop phase and adjusting the phase with a variable phase shifter. Additionally an RF amplifier with a gain $B_2 = 3.91$ is used in order to achieve the required gain $B = 60$. A signal generated by a network

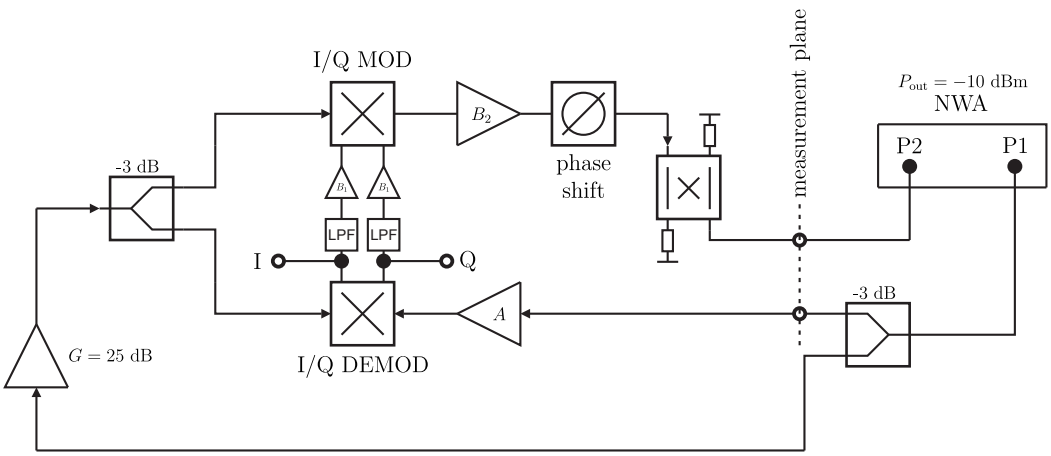

Figure 7.17: Measurement setup for loop phase adjustment

analyzer is divided into two parts, one is used as an input signal for the loop and the second utilized as the LO signal for the modulator and demodulator. The output signal of the loop is fed to the second port of the network analyzer in order the measure magnitude and phase of the transmission coefficient $\underline{S}_{21}$.

In order to examine the closed loop filter characteristic, the measurement setup shown in Figure 7.18 is used. The frequency response is measured from the input (I_{in}, Q_{in}) of an I/Q modulator outside the loop to the output of the I/Q demodulator. A sinusoidal signal is applied to either the I_{in} or Q_{in} input of the I/Q modulator.

The measured frequency response for a phase offset of $-11°$ is depicted in Figure 7.19a and correlates with the simulation results shown in Figure 7.1. The test signal was applied to the Q_{in} input of the I/Q-modulator. As can be seen, the demodulated signal has an I and Q component, where the I signal is at least 6 dB below the Q signal.

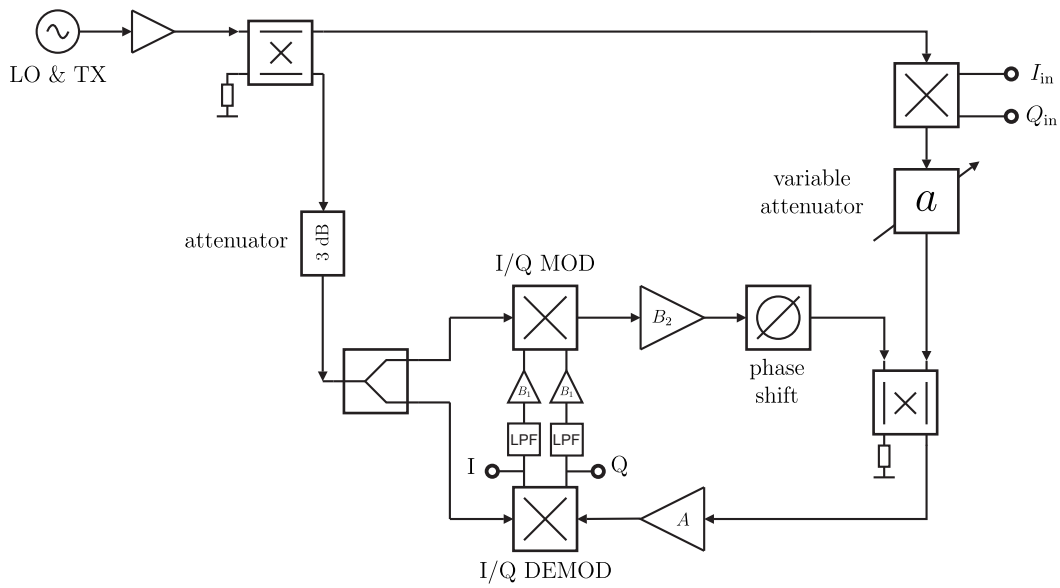

Figure 7.18: Setup for transfer function measurement

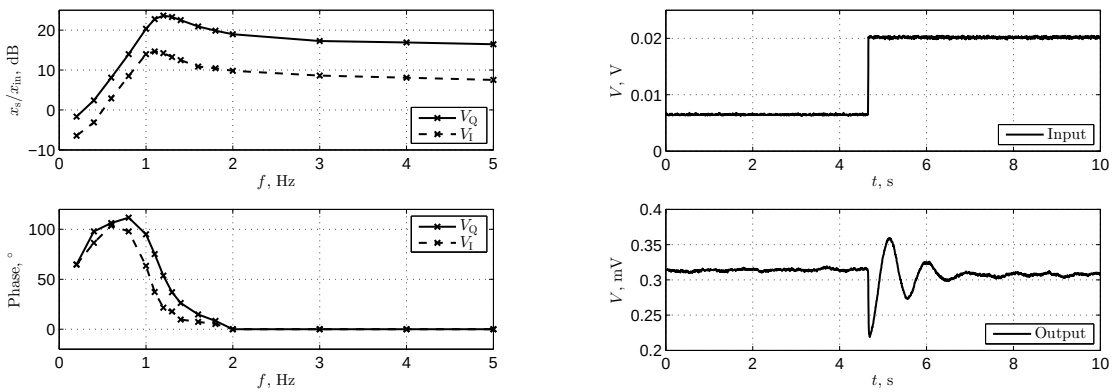

(a) (b)

Figure 7.19: Measured closed loop frequency response (a) and measured step response (b)

This crosstalk results from the fact that the phase of the demodulating signal (LO) is not equal to the phase of the received signal.
The measured step response is depicted in Figure 7.19b. The system settling time is around 4 s.
In the last step the I/Q-modulator and variable attenuator used for signal generation is replaced by a coupler and an antenna in order to conduct the measurement of the heart signal. After placing the antenna on the chest the system settles after approximately 4 s which corresponds to the aforementioned settling time.

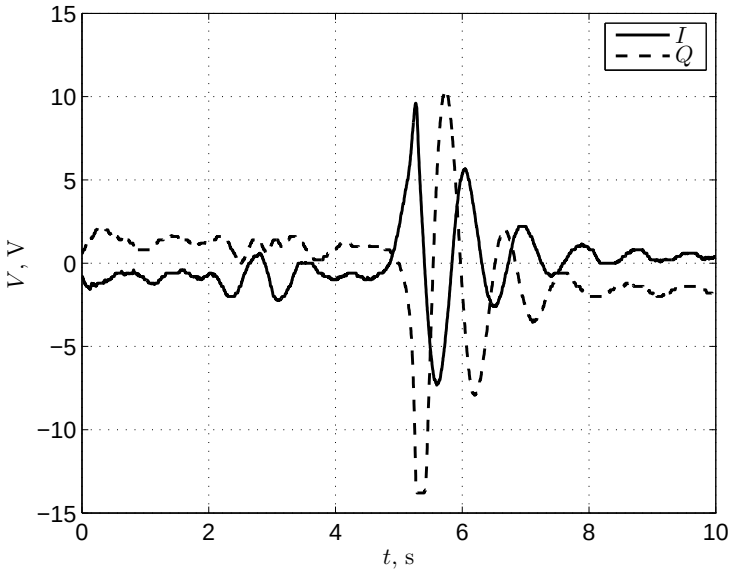

Figure 7.20: Output signal after placing antenna on chest

The entire reflectometer system consists of the canceller circuit with the LO as the transmitter, matching circuit and antenna. First the antenna is placed on the chest and the adaptive matching procedure is started in order to minimize the constant reflection. Then the heart activity is measured.

8 Experimental Evaluation of the Reflectometer

In this chapter the experimental output signal of the reflectometer with canceller circuit is presented and analyzed.

8.1 Evaluation of measured waveforms

The modulated phase is calculated by means of the arctangent demodulation and the amplitude is calculated as the square root of the sum of the squares of the quadrature signals I, Q (Pythagorean theorem). In order to reduce noise, the measured signals are filtered with a moving average filter before calculation of the derived quantities. In a small population survey the impact of the individual body structure and the effect of different positions on the chest is investigated.

Figure 8.1 (a)-(b) shows measured quadrature signals (left) and the calculated amplitude and phase variation (right). It can be seen that both quadrature signals are negative and that the Q-signal has a larger DC-component.
A second measurement (Figure 8.1) (c)-(d) for the same position on the chest was conducted with a longer coaxial cable between antenna port and reflectometer input ($\Delta\theta \approx 100°$). As a result the DC offset and the morphology of the I and Q signals changed. Based on the target-in-clutter model presented in chapter 2, the change in DC offset of the quadrature signals and the modulation of the amplitude, indicate that the static reflection is not suppressed completely (see equation 2.2.22, 2.2.23 and 2.2.20). The DC offset can hamper the proper functioning of the arctangent demodulation (see equation 2.2.21), where the phase is obtained by calculating the inverse tangent of the ratio of Q and I.
It cannot be ruled out that the amplitude is modulated due to the fact that the heart does not only contract and expand but also rotates during the cardiac cycle. Such that the amount of reflection is modulated during the cardiac cycle.
However the morphology of the calculated phase and amplitude for both measurements is quite similar. The constant part of the phase changed from $-100°$ to $63°$ which equals a shift of $165°$, for the second measurement. The actual phase shift for the reflected signal is $200°$ due to the fact that the signal has to pass the cable extension twice. It is assumed that the deviation results from imbalances in the I and Q

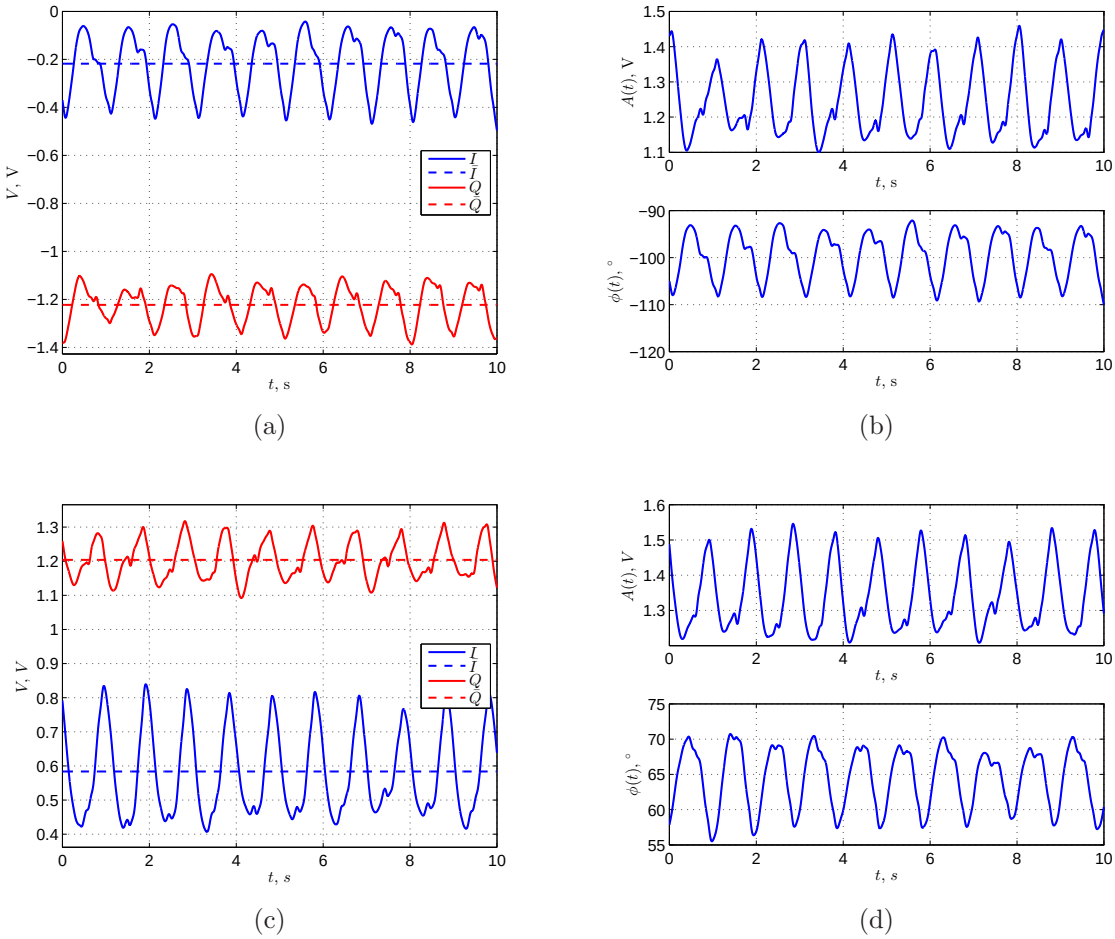

Figure 8.1: Measured quadrature signals and calculated amplitude and phase variation, without cable extension (a,b) and with cable extension, $\Delta\theta \approx 100°$ (c,d)

path (gain imbalance, quadrature error and DC offset) or from a slightly different position due to inexact antenna placement. Additionally the amplitude variation shows for both measurements minor differences with respect to DC-component and signal shape. The two measurements prove that the results are reproducible for a certain position on the chest of an individual person.

Figure 8.2 depicts the spectra of the quadrature signals for both measurements. The first and second harmonic of the heartbeat signal is clearly recognizable in the spectrum of the I signal. In contrast, the spectrum of the Q signals is dominated by the DC component, which is a function of the phase θ. As can be seen, there is no signal component related to respiration in both spectra, which indicates a sufficient suppression.

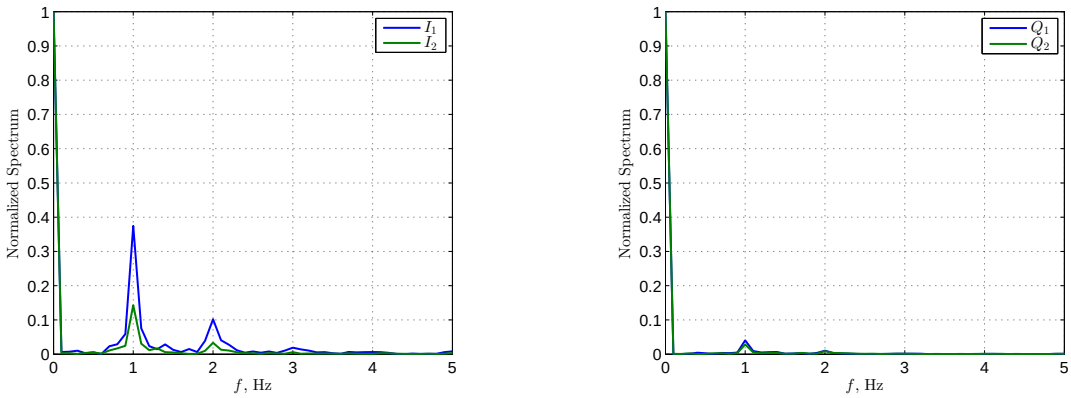

Figure 8.2: Spectra of the measured quadrature signals

Measurements for five different positions (see Fig 8.3) on the chest were conducted and the quadrature signals, the phase variation and instantaneous frequency are compared for position 1-4 (Fig. 8.4). Phase changes are related to the displacement of an object and the instantaneous frequency is related to the velocity of the object movement. As can be seen, the morphology of all mentioned quantities is strongly dependent on the position, which is in compliance with results found in literature ([7] and [24]); nevertheless the waveforms have periodically repeating characteristics.

Figure 8.5 juxtaposes the time derivatives of the I and Q signals, the instantaneous frequency and heart sounds for measurements at position 1. For an assignment of the measured signal state to a mechanical state of the heart, a reference measurement is required which is conducted simultaneously. As a reference, a heart sound measurement is chosen where the first and second heart sound is used to indicate the mechanical state of the heart. The first heart sound indicates the beginning of the systole and the second heart sound indicates the end of systole and the beginning of diastole. Measurements for the mentioned positions are done and it is tried to assign characteristics of the obtained signals to the heart sounds. As can be seen, the simultaneous zero-crossings in the time-derivatives of the I and Q signal and in the instantaneous frequency are co-located. Additionally, the zero-crossings can be assigned to the heart

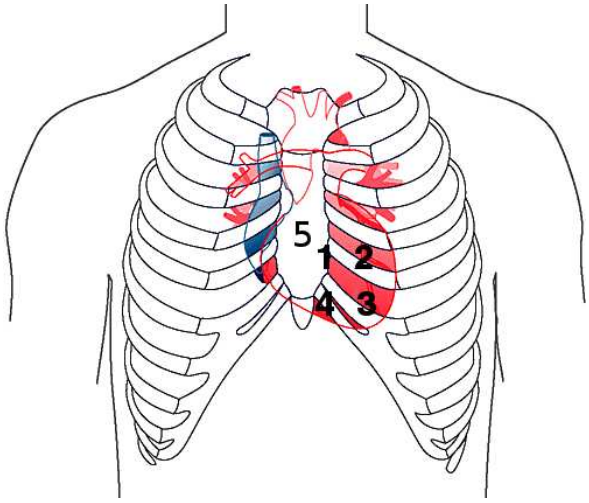

Figure 8.3: Measurement positions

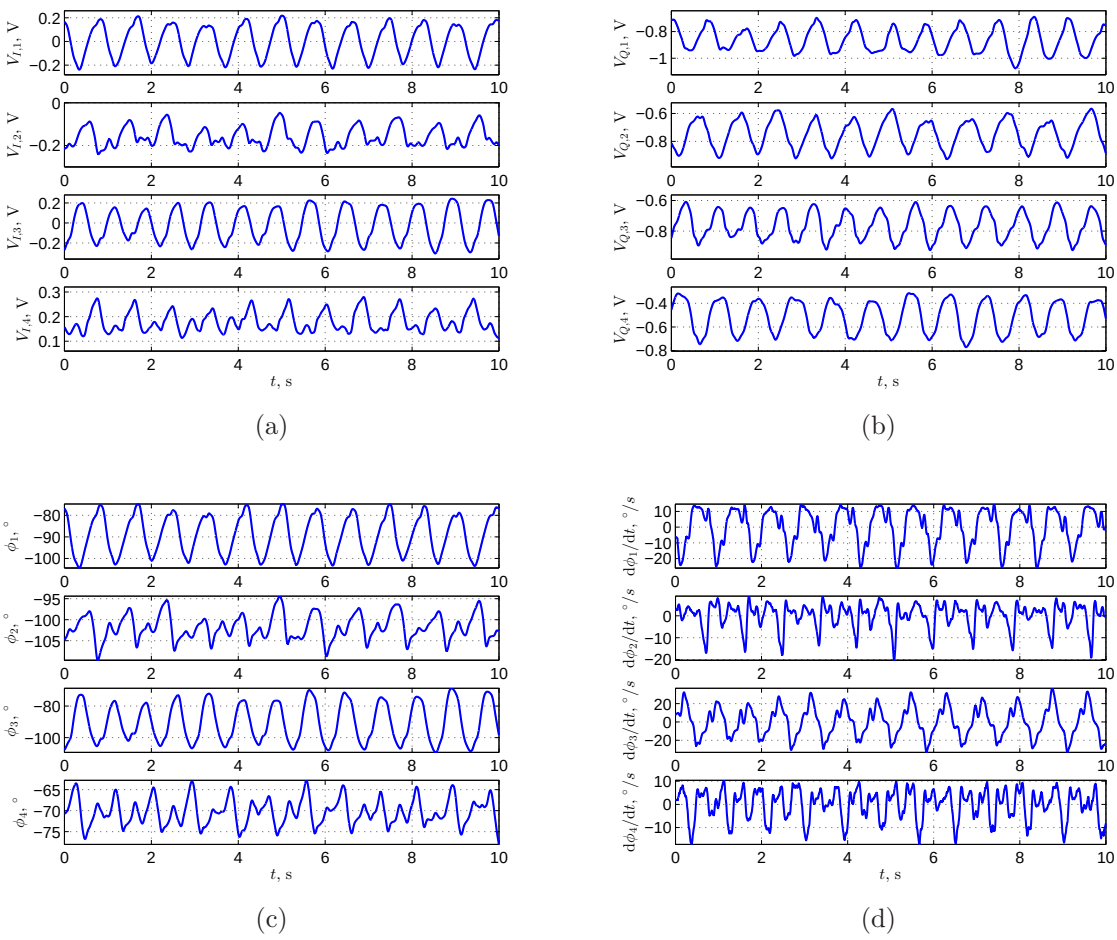

Figure 8.4: Measured quadrature signals (a-b) and calculated phase variation (c) and instantaneous frequency (d), position 1-4

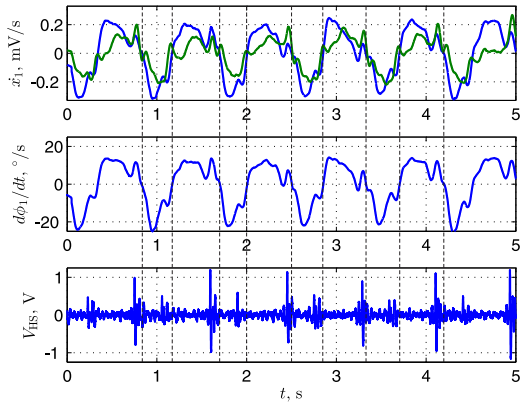

Figure 8.5: Time derivative of I (blue) and Q (green) signals (upper diagram), the instantaneous frequency (middle diagram) and heart sounds (lower diagram).

sounds. Based on equation 2.2.22 and 2.2.23 we obtain for the time-derivatives of the I and Q signal:

$$\frac{\mathrm{d}I}{\mathrm{d}t} = -A_\mathrm{m} \sin\left(\Delta\phi + \phi_\mathrm{h}(t)\right) \frac{\mathrm{d}\phi_\mathrm{h}(t)}{\mathrm{d}t}, \tag{8.1.1}$$

$$\frac{\mathrm{d}Q}{\mathrm{d}t} = A_\mathrm{m} \cos\left(\Delta\phi + \phi_\mathrm{h}(t)\right) \frac{\mathrm{d}\phi_\mathrm{h}(t)}{\mathrm{d}t}. \tag{8.1.2}$$

It can be seen that the time derivatives of the I and Q signal are simultaneously zero if the instantaneous frequency equals zero.
Figure 8.6 shows two measurements of heart sounds and signals obtained simultaneously with the reflectometer at position 5 for one individual. The measurements are conducted with a short time lag and without moving the antenna in order to avoid errors resulting from antenna placement. It can be seen that an assignment of the first

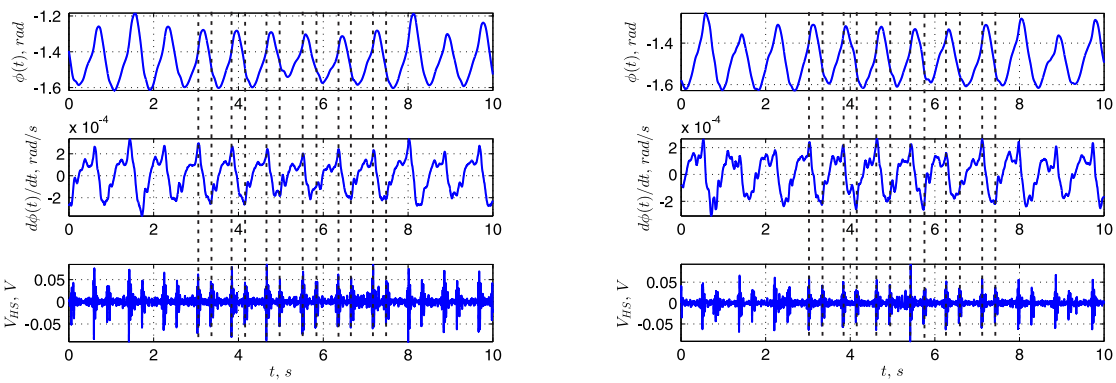

Figure 8.6: Comparison of phase variation, instantaneous frequency and heart sound (upper to lower row) for two measurements at position 5

and second heart sound to characteristics of the waveform of the phase variation and instantaneous frequency is possible. Especially the strong change in the instantaneous frequency during the systolic phase is striking. In addition the first heart sound corresponds to the peak in the instantaneous frequency. During the systolic phase the heart contracts and the ventricular volume decreases. During the diastolic phase an increase of ventricular volume takes place which is in good agreement with the morphology of the phase. Here also the zero-crossings of the instantaneous frequency can be used in order to identify resting states during the cardiac cycle.
In Figure 8.7, measurements at position 5 are shown, where it was tried to reposition the antenna at the same location on the chest as for the first measurement. It can be

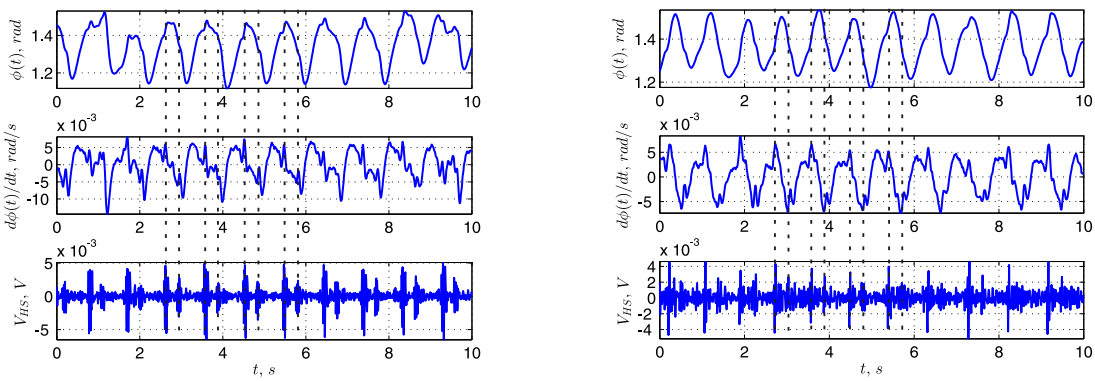

Figure 8.7: Comparison of phase variation, instantaneous frequency and heart sound

seen that the signal morphology of the phase and its time derivative is different for both measurements due to the repositioning. But the changes of the instantaneous frequency during the systole are still present. Due to the fact that the signal shape is different for both measurements, a reliable timing point is the zero-crossing of the instantaneous frequency.
The measurement repeatability could also be proven for a second male person, whereby the waveforms show no similarity compared to other measurements. Figure 8.8 juxtaposes the time derivative of I and Q signals, the instantaneous frequency and heart sounds for two more male persons. Results shown in Figure 8.8a are in compliance with measurements shown in Figure 8.5: The zero-crossings of the instantaneous frequency are co-located with the heard sounds. The measurement depicted in Figure 8.8b shows that the zero-crossings are co-loated to certain states of the heart sounds, but not to the same as in Figure 8.8a.
During measurement it was tried to apply the antenna sensor at the same position on the chest of each individual, then the adaptive matching procedure was performed and subsequently the reflectometer measurement was conducted. As can be seen, the signal morphology is not consistent. This may result from differences in body structure, such that by placing the antenna approximately on the same position on the chest, different parts of the heart are illuminated and the obtained signal waveform also differs.

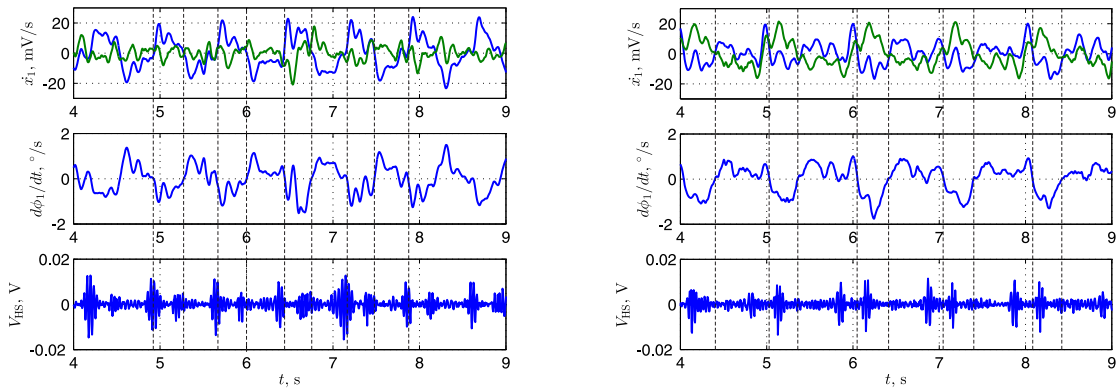

(a) (b)

Figure 8.8: Time derivative of I (blue) and Q (green) signals (upper diagram), the instantaneous frequency (middle diagram) and heart sounds (lower diagram).

8.2 Conclusion

The experimental output signals of the reflectometer with canceller circuit have been presented and analysed. It has been shown that the measurements are reproducible, however significant variations in the signal shape for different positions and persons are existent. The zero-crossing detection seems to be a reliable method for detection of specific heart phases for certain sensor positions. The analysis confirms result found in literature [7] and [24]. However, due to the position dependent signal characteristics, the obtained signals are only suitable to a limited extent as trigger signals.

9 Abstract and Prospective

In this thesis, an on-body reflectometer probe for heartbeat measurement has been investigated. Starting form first initial measurements with a vector network analyzer the underlying theory based on CW Doppler radar technique has been worked out and on-body radar concepts found in literature have been presented. Furthermore a reflectometer sensor system model, containing all components of the reflectometer and describing the formation of the reflected signal, has been presented.
Second, the electromagnetic wave propagation inside the human body and reflections by the heart muscle where investigated by means of EM-simulation assuming a rectangular waveguide radiator filled with a dielectric and excited by a broadband pulse. It was found that the reflection at the body interface and the heart is dependent on the position and orientation of the radiator.
Next, the interaction of a patch antenna, chosen as the sensor antenna, and the human body has been investigated. The radiation characteristic of the antenna has been optimized and the influence of varying body properties has been reduced.
In order to reduce the residual antenna mismatch, which is different for each individual, an adaptive impedance matching network has been designed. The utilized matching algorithm is based on the pattern search method which finds an appropriate matching in a reliable amount of time.
Demodulation and filtering of the received signal is accomplished by a feedback canceller circuit, which has been investigated and optimized. The canceller circuit is capable of filtering the received signal, however the setup is complicated due to the adjustment of several parameter affecting the desired function.
Finally, measurement with the entire sensor system have been conducted and compared to heart sound measurements, which were conducted simultaneously. It has been shown that repeatability and assignment of signal characteristics of the obtained signal to the heart sounds is feasible. However, it has not been possible to obtain the same signal morphology for different individuals and in addition the variation for different positions at the same individual is high, which makes the present sensor hardly suitable for MRI triggering.

In a further work, a profound investigation of the effect of sensor type and position on the chest on signal morphology for different body structures could be conducted and/or an adaptive circuit could be added to the sensor. This could lead to a reduction of the position dependency of the signal morphology to a degree which could allow the use of the sensor as a reliable base for MRI triggering.

Appendices

A Magnetic resonance imaging

Since the target application of the investigated reflectometer probe is to allow triggering of sequences in an MRI system, a basic understanding of MRI is helpful. This chapter is intended to provide a short introduction into the basic functions of MR imaging. It briefly describes the physical principles of MR imaging and generation of cross-sectional images. Furthermore a basic pulse sequence with excitation pulses and gradients is presented. Those who are interested in a comprehensive coverage of this topic are referred to literature on MRI.

Magnetic resonance imaging is a safe and non-invasive method for the creation of detailed pictures of tissues and organs. Safe means that it uses non-ionizing radiation created by magnetic coils. The term non-invasive indicates that no surgery is done. Another advantage is the ability to display several images and oblique cuts through the body.

A.1 Phenomenon of magnetic resonance

Signals from the nuclei of hydrogen atoms are used for the image generation during an MRI examination. A hydrogen atom consists of a nucleus containing a proton and an electron revolving around the nucleus. The proton has a property termed spin, meaning that the proton rotates about its axis [46]. As a rotating mass it has an angular momentum and additionally due to its electrical charge it possesses a magnetic moment and it acts like a small magnet. The latter is the reason why the proton is affected by external magnetic fields and electromagnetic waves. When hydrogen nuclei are exposed to an external magnetic field the magnetic moments tend to align with the direction of the field. The alignment with the magnetic field happens gradually and leads to energy dissipation. In addition the magnetic moments undergo a process called precession, which means that the proton changes the orientation of its rotational axis. The speed of precession is proportional to the external magnetic field and is denoted as Larmor frequency ω_0 [46]:

$$\omega_0 = \gamma_0 \cdot B_0, \tag{A.1.1}$$

where γ_0 is the gyromagnetic ratio and B_0 the strength of the magnetic field. Hydrogen protons have a gyromagnetic ratio of $\gamma_0 = 42.58$ MHz/T, thus for a magnetic field of $7\,T$ the Larmor frequency becomes 298.06 MHz.

Assuming the magnetic field B_0 in the z-direction, the precessing spins align slowly with the magnetic field B_0 and a magnetization into the direction of B_0 builds up. Some of the spins align parallel and some anti-parallel to the magnetic field, where parallel alignment is preferred because it is equivalent to a more favourable energy state. The resulting net magnetization is the difference between parallel and anti-parallel aligned spins and increases with the main magnetic field. By means of an electromagnetic

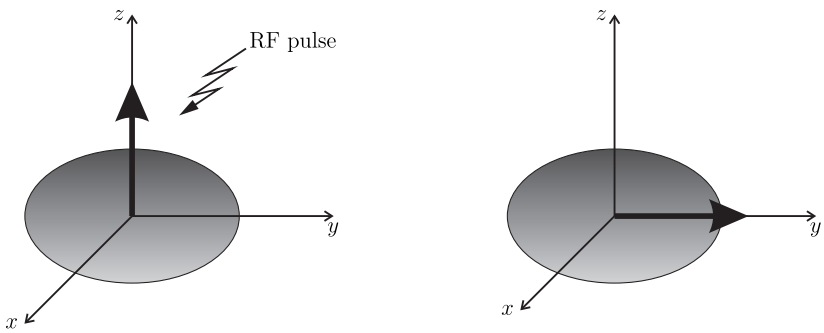

Figure A.1: RF pulse tips the magnetization vector by 90°

wave of the same frequency as the Larmor frequency, generated in a powerful radio transmitter, Energy can be introduced to the spin system (see Figure A.1). The spin system absorbs this energy and the magnetization is rotated perpendicular (xy-plane) to the main magnetic field B_0. This results in a procession about the z-axis and has the effect of an electrical generator which induces an alternating current of the same frequency as the Larmor frequency in a receiver coil. Finally the MR image is generated by processing the collected MR signal with sensitive receivers and computers.

A.2 Slice selection

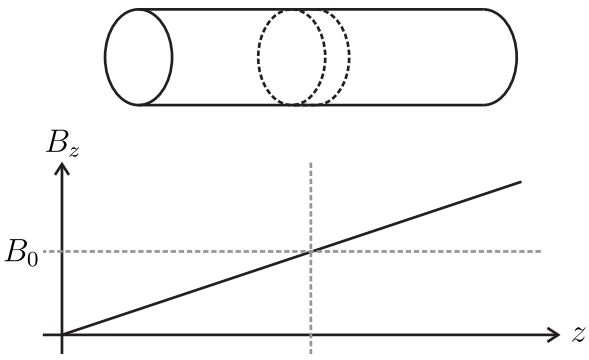

Figure A.2: Slice selection by a gradient field in z-direction

Cross sectional images of the human body are generated by means of an RF excitation pulse which excites only protons in a certain slice and not in the hole body. For this reason magnetic field gradients are generated along the body axis (z-direction) as can

be seen in Figure A.2. The excitation and identification of a slice depends on the Larmor frequency which is proportional to the magnetic field strength. A gradient coil is used to make the magnetic field inhomogeneous in a linear fashion along the z-direction for selective excitation of a certain slice. Consequently there is a gradual change of the Larmor frequency along the z-axis and each slice has a unique frequency. An RF pulse that matches the Larmor frequency of a desired slice excites only protons inside the chosen slice whereas the rest of the body remains unaffected. The slice thickness is related to the strength of the gradient. A strong gradient produces a thin slice and a weak gradient a thick slice.

A.3 Spatial encoding

Spatial encoding is used for the identification of the spatial position of an MR signal. It requires additional gradients along the x- and y-axes and comprises two steps: phase encoding and frequency encoding.

A.3.1 Phase encoding

After the spins have been excited by an RF pulse and precess in the xy-plane, a gradient in the y-direction is turned on for phase encoding. As a result the Larmor frequency of the spins is altered according to their location along the gradient. Spins experiencing a stronger magnetic field increase precession speed and gain phase relative to those spins experiencing lower field strengths. The duration and amplitude of the phase-encoding gradient and the location of the precessing nuclei determines the amount of phase shift. After some time the gradient is turned off and all spins return to their initial precession frequency. This results in a lagging or leading phase of the spins relative to their previous state. Each line in a slice can now be identified by its unique phase due to the fact that the phase changes in a linear manner along the y-axis.

A.3.2 Frequency encoding

The remaining spatial dimension of an MR signal can be identified by a frequency-encoding gradient along to x-axis. Let's assume that this gradient generates a magnetic field that increases in strength from left to right. Then the spins on the left side precess slower than those on the right side which is equivalent to different Larmor frequencies. The signal is collected while the frequency-encoding gradient is switched on and then Fourier transformed to obtain a frequency spectrum containing high frequencies from the right edge and low frequencies from the left edge of the slice. Together phase and frequency encoding facilitate unique spatial identification of volume elements, also known as voxels.

The measured MR signal contains a frequency and phase information. By applying mathematical operations the information can be extracted and the place of origin of the signal can be determined. The position along the x-axis is encoded in the frequency distribution. A Fourier transform can be used to decompose the signal into its frequency components and the location along the x-axis can be identified. The phase distribution contains the position along the y-axis for each frequency. This means that the signal is a sum of all spins precessing with the same frequency but different phases. For the purpose of identification of the phase of an individual spin a set of signals is needed. Therefore the sequence is repeated many times with increasing and decreasing gradient strengths (phase-encoding gradient). To obtain a resolution of n pixels in the y-direction, the measurement has to be repeated n times. This is comparable to solving a mathematical system with many unknowns. A second Fourier transform is applied along the y-axis to derive the phase-encoded spatial information from the set of measurements.

A.4 K-Space

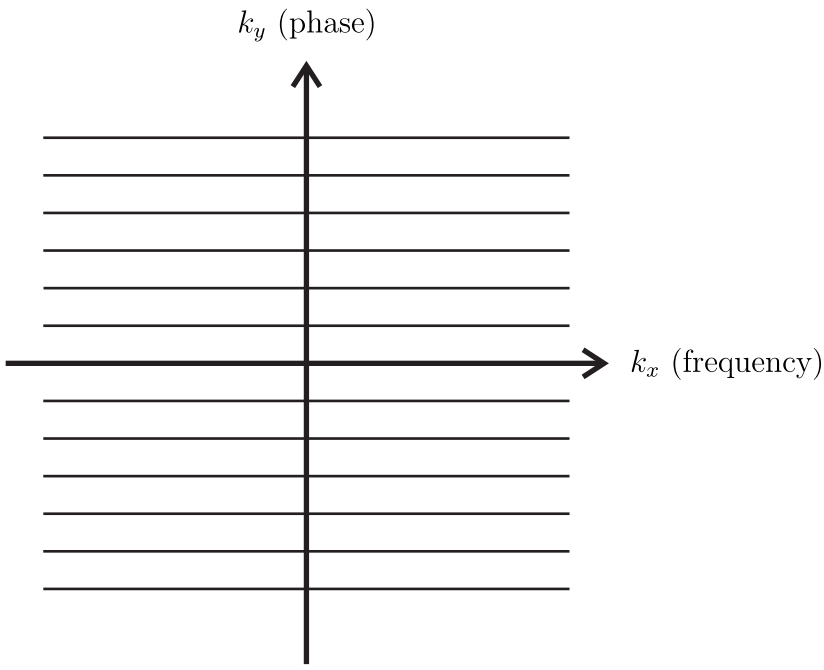

Figure A.3: K-space with frequency and phase-encoding gradients. Horizontal lines represent measurements

The obtained series of signals is stored in a mathematical area called K-space. K-space represents on the horizontal axis (k_x) the frequency information and on the vertical axis (k_y) the phase information. It is a graphic representation of the digitized MR data before Fourier transformation. For each phase-encoding step a measurement is done and displayed as a line in the K-space. After the scan is over and the K-space is

filled with raw data a two-dimensional Fourier transform is applied and an MR image is created where the lines in the K-space do not correspond with the lines in the final MR image. The K-space contains information on the contrast (center of K-space) and the spatial information (outer lines) of the image.

A.5 Basic pulse sequence

Here, a basic pulse sequence is described by the example of a spin echo sequence (see Figure A.4). The spin echo sequence consists of a 90° pulse for excitation, a 180° pulse which generates the spin echo and gradients for slice-selection, phase-encoding and frequency-encoding. In the last step when the spin echo builds up, the signal is read out. This pulse sequence is repeated until the k-space is filled with measurements.

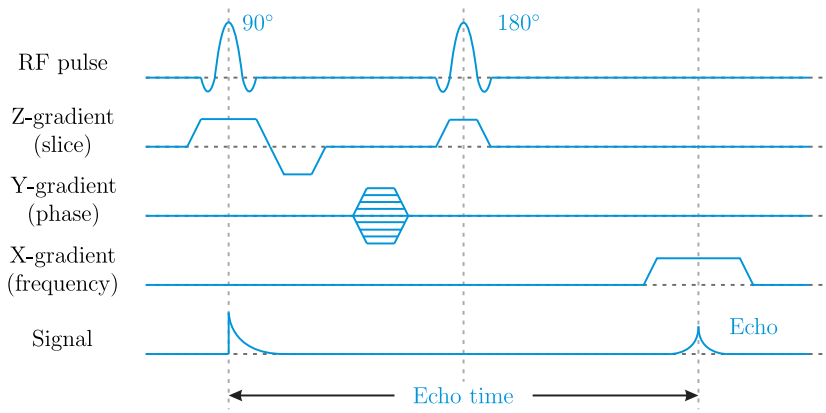

Figure A.4: Spin echo sequence

The duration of one measurement is termed repetition time. The number of phase-encoding steps is equal to the number of repetitions of the sequence. Characteristics of the spin echo sequence are the excellent image quality and a fairly long scan time, which leads to motion artefacts.
In the first step the slice-selection gradient (Z-gradient) is switched on and the 90° pulse is applied. As a result the spins precess in the xy-plane and the magnetization is tipped by 90°. The slice-selection gradient dephases the spin phases along the slice thickness and a so-called rephasing gradient of opposite polarity and half duration is turned on to compensate this effect. Subsequently the phase-encoding gradient (Y-gradient) is switched on and the phase of the spins in changed along the y-axis. The Z-gradient is switched on a second time during the 180° pulse such that only the spins previously stimulated are affected. Finally the frequency-encoding gradient (X-gradient) is turned on and the signal is read out after the echo time.

B Cardiovascular MRI

The indented application of the investigated reflectometer probe in particular is triggering of MR sequences in imaging of the beating heart. Such cardiovascular MRI or cardiac MRI offers the ability to study cardiac functions like cardiac contraction, myocardial perfusion and valvular function in a non-invasive way. Essentially the basic principles of cardiac MRI are the same as for MRI techniques in other body parts. Because of the motion of the heart, motion caused by respiration and effects of flowing blood the imaging encounters some technical difficulties in particular motion artefacts. For this reason the MRI sequences have been adjusted or are acquired in a different way in cardiac MRI [47]. Triggering and cardiac gating are methods used in MRI to reduce motion artefacts based on an accurate representation of the cardiac cycle which, at low-field MR systems mostly is derived from ECG signals.

B.1 Synchronization with ECG

Cardiac motion (contraction and relaxation of the heart muscle) is a crucial factor in the imaging process of cardiac MRI. Application of conventional MRI methods for image acquisition are not synchronized with the cardiac cycle and thus would result in motion artefacts and consequently in an unreadable image. The electrical activity of the heart, measured by means of the electrocardiogram, corresponds to the mechanical events of the heart. Thus the acquired MRI data can be synchronized to the ECG signal. Commonly the R-wave of an ECG signal is used as a trigger for the start of an MRI sequence because the voltage peak in usually higher than the other points of the ECG waveform. This allows to acquire an image of the desired phases in the cardiac cycle relative to the trigger signal. Interesting phases of the heart are the systole and diastole (contraction and relaxation of the heart muscle). Ventricular contraction is indicated by the QRS waveform. Because the mechanical systole occurs approximately 200 ms after electrical systole an image acquisition triggered by the R-wave would depict the end of diastole. Thus a time delay of 200 ms after the R-wave is needed in order to depict mechanical systole [48].
As mentioned in the introduction the surface electrodes of the ECG also measure electrical voltages induced by ions flowing within blood vessels that are exposed to the magnetic field. This source of artefacts is known as magnetohydrodynamic effect and is described in more detail in section B.2. During the systole the heart contracts and blood is ejected which causes a voltage artefact that is superimposed on the ST segment of the ECG. The corrupted ST segment can thus cause a false QRS detection

in certain R-wave detection algorithms and degrade the image quality. RF pulses and the switching of gradient fields is another source of artefacts in the ECG.
A more accurate method is the vector triggering method which acquires the ECG signal via multiple ECG channels simultaneously. It overcomes many of the shortcomings of traditional ECG gating. Besides the different ECG techniques a pulse oximeter can be used for cardiac gating, where the trigger signal is obtained by monitoring blood flow on a finger or ear. In contrast to ECG gating this peripheral method is less precise and the obtained signal is a delayed representation of systole [48].

B.1.1 Prospective triggering and retrospective gating

Image acquisition can be guided in two different ways by the ECG. One technique is the prospective triggering where the preceding R-wave acts as a trigger for the information acquisition during the full cardiac cycle (R-R interval). A major issue with this technique is that the MR acquisition length must be shorter than the average R-R interval. Otherwise the next R-wave would be ignored and the end of the diastole and the early contraction is missed. The other technique, called retrospective gating, acquires MR data continuously and matches images to the ECG tracing recorded by a computer. It is preferred because it acquires images along the full R-R interval.

B.2 Magnetohydrodynamic effect

Blood can be considered as a conductive fluid flowing through a tube (blood vessel). When this fluid is exposed to a high static magnetic field, the charged particles get deflected by the Lorenz force and a voltage is induced orthogonal to both the magnetic field and the direction of flow. This phenomenon is known as magnetohydrodynamic (MHD) effect. The magnitude of the induced voltages is proportional to the flow velocity of the blood v, the vessel diameter d and the strength of the magnetic field B. Thus for the induced voltage U the following equation can be given [49]:

$$U = |B| \cdot |v| \cdot d \cdot \sin\theta, \tag{B.2.1}$$

with θ the angle between the direction of flow and the magnetic field and d orthogonal to B and v.
As mentioned earlier, in cardiac MRI the ECG is used to synchronize the data acquisition to the cardiac cycle. During the blood ejection phase into the aorta the largest voltage is induced. This leads to distortions in the ECG signal and an increase of the T-wave can be observed. Thus the T-wave can become greater than the R-wave and a correct R-wave detection is hindered, in particular as this effect will amplify with higher B_0 field intensities which are used to achieve better image quality [50].

B.3 Interferences induced by gradient switching and RF pulses

Another type of interference arises from the dynamic magnetic fields, which consist of radio frequency pulses with frequencies of up to 289 MHz at 7 T and low-frequency gradient pulses with frequency components below 100 Hz [51]. During the process of imaging in the MR scanner, large magnetic gradients are rapidly switched, whereby a large amount of electrical interference is induced in a conductive loop present in the patient. The loop is formed by the ECG wires, electrodes and tissue of the patient. Dynamic field components perpendicular to the tissue loop induce voltages and corrupt the ECG. Gradients are in many cases the predominant source of interference [51] since the gradient impulses can be similar to the R-wave of the ECG [52]. The RF interferences can be eliminated by a low-pass filter in front of the ECG amplifier due to the fact that the RF pulses are in a much higher frequency range.

Bibliography

[1] Richard E. Wendt III, Roxann Rokey, G. Wesley Vick III, and Donald L. Johnston. Electrocardiographic gating and monitoring in {NMR} imaging. *Magnetic Resonance Imaging*, 6(1):89 – 95, 1988. ISSN 0730-725X. doi: http://dx.doi.org/10.1016/0730-725X(88)90528-0. URL `http://www.sciencedirect.com/science/article/pii/0730725X88905280`.

[2] H.D. Park, S.-P. Cho, and K.-J. Lee. A method for generating mri cardiac and respiratory gating pulse simultaneously based on adaptive real-time digital filters. In *Computers in Cardiology, 2006*, pages 813–816, 2006.

[3] J.W. Krug, G.D. Clifford, G. H. Rose, and J. Oster. The limited applicability of wiener filtering to ecg signals disturbed by the mhd effect. In *Signal Processing Conference (EUSIPCO), 2012 Proceedings of the 20th European*, pages 959–963, 2012.

[4] T. Frauenrath, S. Kozerke, P. Boesiger, and T. Niendorf. Cardiac gating free of interference with electro-magnetic fields at 1.5t, 3.0t and 7.0t. 2008.

[5] O. Kosch, F. Thiel, F. Seifert, J. Sachs, and M. A. Hein. Motion detection in-vivo by multi-channel ultrawideband radar. In *Ultra-Wideband (ICUWB), 2012 IEEE International Conference on*, pages 392–396, 2012. doi: 10.1109/ICUWB.2012.6340451.

[6] O. Aardal, S.-E. Hamran, T. Berger, Y. Paichard, and T.-S. Lande. Chest movement estimation from radar modulation caused by heartbeats. In *Biomedical Circuits and Systems Conference (BioCAS), 2011 IEEE*, pages 452–455, Nov 2011. doi: 10.1109/BioCAS.2011.6107825.

[7] O. Aardal, S. Brovoll, Y. Paichard, T. Berger, T.S. Lande, and S.-E. Hamran. Detecting changes in the human heartbeat with on-body radar. In *Radar Conference (RADAR), 2013 IEEE*, pages 1–6, April 2013. doi: 10.1109/RADAR.2013.6586027.

[8] James C. Lin, J. Kiernicki, M. Kiernicki, and P.B. Wollschlaeger. Microwave apexcardiography. *Microwave Theory and Techniques, IEEE Transactions on*, 27 (6):618–620, 1979. ISSN 0018-9480. doi: 10.1109/TMTT.1979.1129682.

[9] A.D. Droitcour, O. Boric-Lubecke, V.M. Lubecke, Jenshan Lin, and G. T A Kovacs. Range correlation and i/q performance benefits in single-chip silicon doppler

radars for noncontact cardiopulmonary monitoring. *Microwave Theory and Techniques, IEEE Transactions on*, 52(3):838–848, March 2004. ISSN 0018-9480. doi: 10.1109/TMTT.2004.823552.

[10] Amy Diane Droitcour. *Non-contact measurement of heart and respiration rates with a single-chip microwave doppler radar*. PhD thesis, Stanford University, June 2006.

[11] J. A J Thijs, J. Muehlsteff, I.O. Such, R. Pinter, R. Elfring, and C. H. Igney. A comparison of continuous wave doppler radar to impedance cardiography for analysis of mechanical heart activity. In *Engineering in Medicine and Biology Society, 2005. IEEE-EMBS 2005. 27th Annual International Conference of the*, pages 3482–3485, Jan 2005. doi: 10.1109/IEMBS.2005.1617229.

[12] D. Girbau, A.M. Roldan, A. Ramos, and R. Villarino. Remote sensing of vital signs using a doppler radar and diversity to overcome null detection. *Sensors Journal, IEEE*, 12(3):512–518, March 2012. ISSN 1530-437X. doi: 10.1109/JSEN.2011.2107736.

[13] I. Mostafanezhad and O. Boric-Lubecke. An rf based analog linear demodulator. *Microwave and Wireless Components Letters, IEEE*, 21(7):392–394, July 2011. ISSN 1531-1309. doi: 10.1109/LMWC.2011.2154318.

[14] Byung-Kwon Park, O. Boric-Lubecke, and V.M. Lubecke. Arctangent demodulation with dc offset compensation in quadrature doppler radar receiver systems. *Microwave Theory and Techniques, IEEE Transactions on*, 55(5):1073–1079, May 2007. ISSN 0018-9480. doi: 10.1109/TMTT.2007.895653.

[15] Changzhi Li and Jenshan Lin. Complex signal demodulation and random body movement cancellation techniques for non-contact vital sign detection. In *Microwave Symposium Digest, 2008 IEEE MTT-S International*, pages 567–570, June 2008. doi: 10.1109/MWSYM.2008.4633229.

[16] R. Michaelsen, T. Johansen, and K. Tamborg. Investigation of lo-leakage cancellation and dc-offset influence on flicker-noise in x-band mixers. In *Microwave Integrated Circuits Conference (EuMIC), 2012 7th European*, pages 99–102, Oct 2012.

[17] Alexander M. Vergara, O. Boric-Lubecke, and V.M. Lubecke. Dc information preservation for cardiopulmonary monitor utilizing cw doppler radar. In *Engineering in Medicine and Biology Society, 2008. EMBS 2008. 30th Annual International Conference of the IEEE*, pages 1246–1249, Aug 2008. doi: 10.1109/IEMBS.2008.4649389.

[18] Ting-Yueh Chin, Kun-Ying Lin, Sheng-Fuh Chang, and Chia-Chan Chang. A fast clutter cancellation method in quadrature doppler radar for noncontact vital signal detection. In *Microwave Symposium Digest (MTT), 2010 IEEE MTT-S International*, pages 764–767, May 2010. doi: 10.1109/MWSYM.2010.5516811.

[19] M.S. Rahman, M.M. Haque, Byung-Jun Jang, and Ki-Doo Kim. Extended kalman filter for doppler radar cardiopulmonary monitoring system. In *Electrical Computer Engineering (ICECE), 2012 7th International Conference on*, pages 264–267, Dec 2012. doi: 10.1109/ICECE.2012.6471536.

[20] S. Pisa, P. Bernardi, M. Cavagnaro, E. Pittella, and E. Piuzzi. Monitoring of cardio-pulmonary activity with uwb radar: A circuital model. In *Electromagnetic Compatibility and 19th International Zurich Symposium on Electromagnetic Compatibility, 2008. APEMC 2008. Asia-Pacific Symposium on*, pages 224–227, May 2008. doi: 10.1109/APEMC.2008.4559852.

[21] O. Aardal, Y. Paichard, S. Brovoll, T. Berger, T.S. Lande, and S.-E. Hamran. Physical working principles of medical radar. *Biomedical Engineering, IEEE Transactions on*, 60(4):1142–1149, April 2013. ISSN 0018-9294. doi: 10.1109/TBME.2012.2228263.

[22] Constantine A. Balanis. *Antenna Theory*, volume Second Edition. 1997.

[23] J. Muehlsteff, J. A J Thijs, and R. Pinter. The use of a two channel doppler radar sensor for the characterization of heart motion phases. In *Engineering in Medicine and Biology Society, 2006. EMBS '06. 28th Annual International Conference of the IEEE*, pages 547–550, Aug 2006. doi: 10.1109/IEMBS.2006.260170.

[24] J. Muehlsteff, J. Thijs, R. Pinter, G. Morren, and G. Muesch. A handheld device for simultaneous detection of electrical and mechanical cardio-vascular activities with synchronized ecg and cw-doppler radar. In *Engineering in Medicine and Biology Society, 2007. EMBS 2007. 29th Annual International Conference of the IEEE*, pages 5758–5761, Aug 2007. doi: 10.1109/IEMBS.2007.4353655.

[25] L. Knisevskaja, K.-F. Berggren, V. Engelson, and B.-A. Galwas. Microwave scattering by a three-dimensional model human heart. In *Microwaves, Radar and Wireless Communications, 2002. MIKON-2002. 14th International Conference on*, volume 1, pages 107–110 vol.1, 2002. doi: 10.1109/MIKON.2002.1017817.

[26] S. Gabriel, R. W. Lau, and C. Gabriel. The dielectric properties of biological tissues: III. parametric models for the dielectric spectrum of tissues. *Physics in Medicine and Biology*, 41(11), 1996.

[27] A. E C Tan and M. Y W Chia. Measuring human body impulse response using {UWB} radar. *Electronics Letters*, 41(21):1193–1194, 2005. ISSN 0013-5194. doi: 10.1049/el:20052417.

[28] R.K. Moore. Effects of a surrounding conducting medium on antenna analysis. *Antennas and Propagation, IEEE Transactions on*, 11(3):216–225, May 1963. ISSN 0018-926X. doi: 10.1109/TAP.1963.1138043.

[29] AK. Skrivervik. Implantable antennas: The challenge of efficiency. In *Antennas and Propagation (EuCAP), 2013 7th European Conference on*, pages 3627–3631, April 2013.

[30] J. Pribetich, R. Ledee, P. Kennis, P. Pribetich, and M. Chive. Modelling of microstrip antenna with dielectric protective layer for lossy medium. *Electronics Letters*, 24(23):1464–1465, Nov 1988. ISSN 0013-5194.

[31] Rajeev R. Wakodkar, Samik Chakraborty, and Bhaskar Gupta. Resonant frequency variation of rectangular patch antenna due to accumulation of water over its surface. *ARPN Journal of Engineering and Applied Sciences*, 6(4):49–60, April 2011.

[32] G. Chakaravarthi and K. Arunachalam. A compact microwave patch applicator for hyperthermia treatment of cancer. In *Engineering in Medicine and Biology Society (EMBC), 2014 36th Annual International Conference of the IEEE*, pages 5320–5322, Aug 2014. doi: 10.1109/EMBC.2014.6944827.

[33] S. Curto, T.S.P. See, P. McEvoy, M.J. Ammann, and Z.N. Chen. In-silico hyperthermia performance of a near-field patch antenna at various positions on a human body model. *Microwaves, Antennas Propagation, IET*, 5(12):1408–1415, September 2011. ISSN 1751-8725. doi: 10.1049/iet-map.2010.0611.

[34] M. A. Ebrahimi-Ganjeh and A. R. Attari. Study of water bolus effect on sar penetration depth and effective field size for local hyperthermia. *Progress In Electromagnetics Research B*, 4:273–283, 2008.

[35] M. Sanad. Effect of the human body on microstrip antennas. In *Antennas and Propagation Society International Symposium, 1994. AP-S. Digest*, volume 1, pages 298–301 vol.1, June 1994. doi: 10.1109/APS.1994.407753.

[36] R. K. Amineh, A. Trehan, and N. K. Nikolova. Tem horn antenna for ultra-wide band microwave breast imaging. *Progress In Electromagnetics Research*, 13:59–74, 2009.

[37] Aidin Razavi and Jian Yang. Optimal size of uniform aperture for near-field penetration through lossy medium. *Microwave and Optical Technology Letters*, 56(10):2301–2304, 2014. ISSN 1098-2760. doi: 10.1002/mop.28578. URL `http://dx.doi.org/10.1002/mop.28578`.

[38] Doug Jorgesen and Christopher Marki. *Directivity and VSWR Measurements Understanding Return Loss Measurements*. Marki Microwave, Inc, 2012.

[39] *Reflectometer Measurements - Revisited*. Anritsu, April 2000.

[40] Xinyuan Wang, Jingzhao She, and Zhenghe Feng. Real time measurement of vswr with directional couplers. In *Microwave and Millimeter Wave Technology, 2004. ICMMT 4th International Conference on, Proceedings*, pages 719–722, Aug 2004. doi: 10.1109/ICMMT.2004.1411630.

[41] Doug Rytting. *An Analysis of Vector Measurement Accuracy Enhancement Techniques*. Heweltt Packard.

[42] Fan Xiangning, Sun Yutao, and Feng Yangyang. An efficient cmos dc offset cancellation circuit for pga of low if wireless receivers. In *Wireless Communications and Signal Processing (WCSP), 2010 International Conference on*, pages 1–5, 2010. doi: 10.1109/WCSP.2010.5633563.

[43] Seung-Min Oh, Kyoung-Seok Park, Hyun-Hwan Yoo, Yoo-Sam Na, and Taek-Soo Kim. A design of dc offset canceller using parallel compensation. In *Circuits and Systems, 2007. ISCAS 2007. IEEE International Symposium on*, pages 1685–1688, 2007. doi: 10.1109/ISCAS.2007.377917.

[44] P.D.L. Beasley, A. Stove, B.J. Reits, and B. As. Solving the problems of a single antenna frequency modulated cw radar. In *Radar Conference, 1990., Record of the IEEE 1990 International*, pages 391–395, May 1990. doi: 10.1109/RADAR.1990.201197.

[45] Ron Mancini, editor. *Op Amps For Everyone*. Texas Instruments, 2002.

[46] Dominik Weishaupt, Victor D. Koechli, Borut Marincek, J.M. Froehlich, D. Nanz, and K.P. Pruessmann. *How Does Mri Work? - An Introduction to the Physics and Function of Magnetic Resonance Imaging*. Springer, Berlin, Heidelberg, 3rd edition, 2003. ISBN 978-3-540-44094-9.

[47] Jan Bogaert, Steven Dymarkowski, Andrew M. Taylor, and Vivek Muthurangu. *Clinical Cardiac MRI -*. Springer, Berlin, Heidelberg, 2nd ed. 2012 edition, 2012. ISBN 978-3-642-23034-9.

[48] MD Daniel J. Parker and PhD Dennis L. Parker. Cardiac gating in mri applications. *Applied Radiology*, 31(6):65–71, June 2002.

[49] G.M. Nijm, S. Swiryn, A. C. Larson, and A.V. Sahakian. Characterization of the magnetohydrodynamic effect as a signal from the surface electrocardiogram during cardiac magnetic resonance imaging. In *Computers in Cardiology, 2006*, pages 269–272, 2006.

[50] D. Abi-Abdallah, V. Robin, A. Drochon, and O. Fokapu. Alterations in human ecg due to the magnetohydrodynamic effect: A method for accurate r peak detection in the presence of high mhd artifacts. In *Engineering in Medicine and Biology Society, 2007. EMBS 2007. 29th Annual International Conference of the IEEE*, pages 1842–1845, 2007. doi: 10.1109/IEMBS.2007.4352673.

[51] M.K. Laudon, J.G. Webster, R. Frayne, and T.M. Grist. Minimizing interference from magnetic resonance imagers during electrocardiography. *Biomedical Engineering, IEEE Transactions on*, 45(2):160–164, 1998. ISSN 0018-9294. doi: 10.1109/10.661264.

[52] R.L. Hughes. Dual slew-rate limiting for reducing gradient field interference in cardiac gated magnetic resonance imaging. *Electronics Letters*, 45(6):298–300, 2009. ISSN 0013-5194. doi: 10.1049/el.2009.3082.